https://doi.org/10.15388/vu.thesis.999
https://orcid.org/0009-0004-0193-1883

VILNIUS UNIVERSITY

CENTER FOR PHYSICAL SCIENCES AND TECHNOLOGY

Arnoldas Solovjovas

Excitation-Relaxation Processes in Cerium Activated Garnet Scintillators

DOCTORAL DISSERTATION

Natural Sciences,
Physics (N 002)

VILNIUS 2026

This dissertation was prepared between 2022 and 2026 at the Institute of Photonics and Nanotechnology, Vilnius University.

Academic Supervisor – Dr. Saulius Nargelas (Vilnius University, Natural Sciences, Physics, N 002).

This Doctoral Dissertation will be Defended in a Public Meeting of the Dissertation Defence Panel:
Chairman – Prof. Dr. Vincas Tamošiūnas (Vilnius University, Natural Sciences, Physics, N 002).

Members:
Prof. Dr. Tomas Čeponis (Vilnius University, Technological Sciences, Materials Engineering, T 008),
Prof. Habil. Dr. Vidmantas Gulbinas (Center for Physical Sciences and Technology, Natural Sciences, Physics, N 002),
Dr. Saulius Miasojedovas (Vilnius University, Natural Sciences, Physics, N 002),
Dr. Sandra Witkiewicz-Łukaszek (Kazimierz Wielki University, Poland, Natural Sciences, Physics, N 002).

The dissertation will be defended at a public meeting of the Dissertation Defence Panel at 2 p.m. on October 29, 2026, in Room A101 of the National Center for Physical Sciences and Technology.
Address: Saulėtekio Ave. 3, Vilnius, Lithuania; tel. +370 5 264 8884; e-mail: office@ftmc.lt.

https://doi.org/10.15388/vu.thesis.999
https://orcid.org/0009-0004-0193-1883

VILNIAUS UNIVERSITETAS

FIZINIŲ IR TECHNOLOGIJOS MOKSLŲ CENTRAS

Arnoldas Solovjovas

Sužadinimo-relaksacijos procesai ceriu aktyvuotuose granatiniuose scintiliatoriuose

DAKTARO DISERTACIJA

Gamtos mokslai,
Fizika (N 002)

VILNIUS 2026

Disertacija rengta 2022–2026 metais Vilniaus universiteto Fotonikos ir nanotechnologijų institute.

Mokslinis vadovas – dr. Saulius Nargelas (Vilniaus universitetas, gamtos mokslai, fizika, N 002).

Gynimo taryba:
Pirmininkas – prof. dr. Vincas Tamošiūnas (Vilniaus universitetas, gamtos mokslai, fizika, N 002).

Nariai:
prof. dr. Tomas Čeponis (Vilniaus universitetas, technologijos mokslai, medžiagų inžinerija, T 008),
prof. habil. dr. Vidmantas Gulbinas (Fizinių ir technologijos mokslų centras, gamtos mokslai, fizika, N 002),
dr. Saulius Miasojedovas (Vilniaus universitetas, gamtos mokslai, fizika, N 002),
dr. Sandra Witkiewicz-Łukaszek (Kazimierz Wielki universitetas, Lenkija, gamtos mokslai, fizika, N 002).

Disertacija ginama viešame Gynimo tarybos posėdyje 2026 m. spalio 29 d. 14 val. Nacionalinio fizinių ir technologijos mokslų centro A101 auditorijoje. Adresas: Saulėtekio al. 3, Vilnius, Lietuva; tel. +370 5 264 8884; el. paštas: office@ftmc.lt.

„Pirmiausia pamiršk įkvėpimą. Įprotis yra patikimesnis. Įprotis – tai kasdieniu darbu virtęs atkaklumas.“

Octavia E. Butler

PADĖKA

Kai pagaliau atėjo metas rašyti disertacijos padėką, supratau, kiek daug žmonių prisidėjo prie to, kad šiandien būčiau šiame savo gyvenimo etape. Daugiau nei dešimt metų Vilniaus universitete nebūtų buvę tokie prasmingi be žmonių, kuriuos noriu paminėti.

Pirmiausia dėkoju savo šeimai: tėčiui Valerijui, broliui Artūrui ir, žinoma, mamai Jadvygai. Mama įdėjo daug pastangų ir paaukojo ne vieną bemiegę naktį, kad šiandien būčiau čia. Ji nuo mažens ugdė mano discipliną, kantrybę ir ryžtą siekti užsibrėžto rezultato. Jei prie kai kurių žmonių sėkmės nemažai prisideda talentas, mane pirmyn visada vedė šeimos išugdytas užsispyrimas.

Nuoširdi padėka mano gimtajai Vilniaus Žvėryno gimnazijai. Ačiū mokytojams už jų atsidavimą, kantrybę ir meilę savo darbui. Ačiū klasiokams už bendruomenę, kurioje buvo natūralu siekti žinių, augti ir skatinti vieniems kitus siekti geriausių rezultatų Lietuvoje ir už jos ribų.

Dėkoju Vilniaus universiteto ir Fizikos fakulteto bendruomenei. Dažnai sulaukiu klausimo, kaip galima tiek metų praleisti vienoje vietoje vien tik studijuojant. Atsakymas man visada buvo paprastas: noriu mokytis visą likusį gyvenimą. Esu dėkingas, kad tai galėjau daryti apsuptas žmonių, iš kurių kasdien galėjau mokytis. Atskira padėka Vilniaus universiteto Studentų atstovybei, kuri padėjo tvirtus pamatus mano asmeniniam augimui ir suteikė neįkainojamos patirties.

Studijų metu teko išbandyti ne vieną mokslinę kryptį, o kiekviena jų padėjo geriau suprasti, kurioje srityje norėčiau tęsti savo mokslinį kelią. Todėl nuoširdžiai dėkoju prof. Gintautui Tamulaičiui už priėmimą į mokslinę grupę ir suteiktą galimybę toliau augti Vilniaus universitete.

Savo doktorantūros vadovui dr. Sauliui Nargelui galėčiau skirti atskirą disertaciją vien padėkai. Ačiū, kad sutikote būti mano vadovu ir leidotės kartu į šią „amerikietiškų kalnelių“ kelionę. Ačiū, kad visuose dideliuose ir mažuose procesuose buvote mokytojas, mentorius ir patarėjas. Dar labiau dėkoju už kantrybę – po kiekvienos nesėkmės ar klaidos padėjote man judėti pirmyn. Sakoma, kad kiekvienas žmogus turi savo kantrybės taurę, tačiau atrodo, kad Jūsų atveju tai buvo visas bidonas.

Nuoširdi padėka Fotonikos ir nanotechnologijų instituto kolegoms už tai, kad priėmėte mane į savo bendruomenę ir leidote joje augti. Dėkoju Žydrūnui ir Kazimierui, su kuriais teko dalytis kabinetu. Gyvenimiški pokalbiai, draugiškas patraukimas per dantį tapo neatsiejama darbo dalimi.
Galiausiai dėkoju draugams ir kolegoms, su kuriais gyvenimas netikėtai suvedė. Visi jūs vienaip ar kitaip prisidėjote prie mano kelionės: vieni padėjote rasti kryptį, kiti neleido sustoti tuomet, kai buvo sunkiausia. Ačiū už visas kartu išgyventas džiaugsmo, nusivylimo, juoko ir ašarų akimirkas. O kurie iš jūsų slypi už šių eilučių – patys puikiai žinote.

Arnoldas Solovjovas

Contents

1 ACRONYMS **10**

2 INTRODUCTION **12**

3 LITERATURE REVIEW **17**
3.1 Physical processes in scintillators 17
3.2 Applications of scintillators 26
3.3 Scintillator manufacturing 31

4 EXPERIMENTAL METHODS **37**

5 Excitation-relaxation processes in $Y_3(Al_{1-x}Ga_x)_5O_{12}$:Ce **43**
5.1 Samples 46
5.2 Results 47
5.3 Summary and highlights 62

6 Excitation-relaxation processes in $(Lu_xGd_{1-x})_3(Ga_yAl_{1-y})_5O_{12}$:Ce,Mg **63**
6.1 Samples 66
6.2 Results 67
6.3 Summary and highlights 82

7 Excitation-relaxation processes in $(Lu_xY_{1-x})_3Al_5O_{12}$:Ce silica-based composites **83**
7.1 Samples 86
7.2 Results 87
7.3 Summary and highlights 98

REFERENCES **99**

SANTRAUKA **122**

CURRICULUM VITAE **164**

LIST OF PUBLICATIONS **165**

LIST OF OTHER PUBLICATIONS **166**

LIST OF CONFERENCES **167**

1. ACRONYMS

Abbreviation	Definition
BS	Bridgman Method
CB	Conduction Band
CCC	Crystal Clear Collaboration
CCD	Charge-Coupled Device
CERN	European Organization for Nuclear Research
CL	Cathodoluminescence
CMOS	Complementary Metal–Oxide–Semiconductor
CMS	Compact Muon Solenoid
CT	Computed Tomography
CTR	Coincidence Timing Resolution
CVD	Chemical Vapor Deposition
CZ	Czochralski Method
e-beam	Electron Beam
FWHM	Full Width at Half Maximum
GAGG	Gadolinium Aluminum Gallium Garnet
GDMS	Glow Discharge Mass Spectrometry
HEP	High-Energy Physics
HL-LHC	High-Luminosity Large Hadron Collider
ICDD	International Centre for Diffraction Data
LED	Light-Emitting Diode
LHCb	Large Hadron Collider Beauty Experiment
LPE	Liquid-Phase Epitaxy
LuAG	Lutetium Aluminum Garnet
LuGAGG	Lutetium Gadolinium Gallium Aluminum Garnet
LuYAG	Lutetium Yttrium Aluminum Garnet
LY	Light Yield
LYSO	Lutetium Yttrium Oxyorthosilicate
PET	Positron Emission Tomography
PL	Photoluminescence
PVD	Physical Vapor Deposition
QY	Quantum Yield
SC	Single Crystal
SCF	Single-Crystal Films

Abbreviation	Definition
SCINT	International Conference on Scintillating Materials and their Applications
SCS	Solution Combustion Synthesis
SEM	Scanning Electron Microscopy
SNR	Signal-to-Noise Ratio
SPE	Solid-Phase Epitaxy
TINR	Temperature-Independent Nonradiative Recombination
TOF-PET	Time-of-Flight Positron Emission Tomography
TRPL	Time-Resolved Photoluminescence
wLEDs	White Light-Emitting Diodes
XANES	X-Ray Absorption Near-Edge Structure
XRD	X-Ray Diffraction
YAG	Yttrium Aluminum Garnet
YAGG	Yttrium Aluminum Gallium Garnet
YGG	Yttrium Gallium Garnet

2. INTRODUCTION

Scintillating materials are essential components of many modern technologies. Even a brief review of the literature demonstrates their broad range of applications, extending from medical imaging to high-energy physics (HEP) experiments [1], [2], [3], [4]. A scintillator is a material that absorbs high-energy radiation, such as X-rays, gamma rays, or high-energy particles, and converts it into light, typically in the ultraviolet or visible spectral range [5], [6]. This conversion enables the detection and quantification of radiation that would otherwise remain invisible. Owing to this property, scintillators are widely used in applications ranging from household white light-emitting diodes (wLEDs) to advanced medical imaging systems and large-scale HEP experiments [7], [8], [9].

In the early development of scintillators, the primary requirement was the ability to detect radiation and generate a measurable visible-light signal [10]. Over time, however, the range of desired material properties has expanded significantly, driven by the specific requirements of different application fields. High light yield (LY), fast scintillation response (i.e., short rise and decay times), good energy resolution, and radiation hardness are now considered among the key performance parameters [11]. For example, in HEP experiments at CERN, there is an ongoing effort to achieve time resolutions on the order of 10 ps [4]. Detectors in such environments are exposed to extremely high radiation doses and intense particle fluxes, necessitating scintillating materials capable of maintaining stable performance under these harsh operating conditions.

Among the various material classes, garnet-based scintillators have recently emerged as a highly promising group due to their high density, which is essential for efficient detection of high-energy particles, and their compositional flexibility, particularly for HEP applications [12]. Their main advantage lies in the structural and compositional versatility of the garnet lattice, which allows partial substitution of cations without complete disruption of the crystal structure. This flexibility enables systematic tuning of the scintillation properties through controlled doping and compositional engineering.

Cerium ions are considered highly efficient luminescence activators due to their fast 5d→4f optical transition [13]. Such performance can only be achieved under ideal conditions, where no carrier traps or antisite defects are

present in the lattice structure [14]. One of the major limitations preventing Ce-doped garnet scintillators from broader application in fields such as HEP is the presence of trapping-related processes [15]. In such cases, radiative recombination becomes slower, or non-radiative recombination processes may become dominant. Another significant challenge is achieving an optimal balance between high light output and fast scintillation response. Materials used for wLED manufacturing are generally unsuitable for applications such as CERN experiments, and vice versa. Identifying a suitable candidate that provides an appropriate balance between a fast scintillation response and photoluminescence (PL) intensity remains highly challenging. The development of improved scintillating materials may appear straightforward: starting from an already well-performing host, one could introduce selected dopants to enhance specific properties. However, in practice, this approach is highly non-trivial. The incorporation of additional ions into the crystal lattice can lead to structural distortions and defects [16]. Not all dopants are compatible with a given host matrix or with the required synthesis and crystal growth conditions. One possible approach is band-gap engineering, which can suppress existing shallow electron traps by burying them in the conduction band (CB) [15]. However, this may simultaneously reduce the material's resistance to thermal ionization processes. The current challenge remains the identification of a single host material that would allow band-gap engineering to be applied in a manner that enables the tuning of essential properties required for distinct application areas.

Several studies have reported that aliovalent codoping with Ca^{2+} or Mg^{2+} ions can lead to a faster scintillation response [17]. This is typically performed at low concentrations, as heavier aliovalent codoping often leads to diminished PL intensity and more pronounced non-radiative recombination, commonly associated with the stabilization of Ce^{4+} ions [18]. Although the literature generally interprets these effects through the stabilization of Ce^{4+}, not all observations can be consistently explained within this framework, particularly in cases where resonant excitation and excitation with high-energy electron flux produce comparable results.

CERN periodically implements technological upgrades, with the High-Luminosity Large Hadron Collider (HL-LHC) currently representing one of the major ongoing developments. In addition to the search for materials with higher PL intensity, a faster scintillation response, and enhanced radiation tolerance, production cost remains a critical consideration [11], [19]. Conse-

quently, alternative fabrication approaches are being explored to identify more cost- and time-efficient substitutes for conventional single-crystal (SC) growth techniques. One particularly promising approach is the two-step sol–gel method, although it still requires thorough characterization. This technique offers considerable flexibility in terms of compositional design, while also providing significantly faster and more cost-effective synthesis compared to conventional crystal growth methods.

Aim, task and novelty

This work presents a series of Ce-doped garnet scintillators. Although all investigated materials belong to the same garnet family, they differ significantly in their host composition (e.g., YAG, LuAG), which strongly influences their luminescence and scintillation performance. In addition, the studied materials involve different fabrication methods and material engineering strategies aimed either at improving scintillator performance or developing more cost-effective production approaches. **The aim of this work** is to identify the processes that limit the emission efficiency and scintillation response of Ce-doped garnet-based scintillators by investigating host materials optimized through different engineering strategies, including band-gap engineering, heavy aliovalent codoping, and composite fabrication using a two-step sol–gel method.

To achieve this aim, a **general task was formulated**: to characterize Ce-doped garnet-based scintillators using a consistent set of experimental techniques, including PL, time-resolved photoluminescence (TRPL), quantum yield (QY), and cathodoluminescence (CL) measurements, while varying key experimental conditions such as excitation regimes, temperature range, and excitation energy density.

The first chapter presents a systematic investigation of gallium incorporation in $Y_3(Al_{1-x}Ga_x)_5O_{12}$:Ce scintillators over a broad compositional range (x = 0–1). The novelty of this chapter lies in identifying the gallium concentration range in which QY and scintillation response can be optimized.

The second chapter demonstrates that heavy aliovalent codoping with Mg in Ce-doped garnet scintillator LuGAGG leads to a significant shortening of the luminescence decay time, together with reduced PL intensity. The novelty of this chapter is the identification of an alternative mechanism responsible for this behaviour, showing that the effect is caused by the formation of an additional emission centre.

The third chapter presents the development and characterization of silica and Ce-doped garnet scintillator composites synthesized using a two-step sol–gel fabrication method. The novelty of this chapter lies in demonstrating the potential of this approach as an economically and technologically efficient alternative to conventional scintillator fabrication methods.

Defense statements

Statement 1 Incorporation of gallium in scintillator $Y_3(Al_{1-x}Ga_x)_5O_{12}$:Ce up to $x \sim 0.7$ decreases the barrier for thermal depopulation of Ce^{3+} emitting level and results in reduced ratio between luminescence decay time and light yield, ensuring improvement of timing performance of the scintillator. Further increase in gallium content leads to drastic performance deterioration.

Statement 2 Heavy magnesium codoping in LuGAGG:Ce creates modified emission centres Ce^{3+}+Mg^{2+} that accelerate luminescence decay by introducing an additional temperature-independent nonradiative recombination channel and by enhancing thermal quenching over a barrier of 0.2 eV, substantially lower than that of regular Ce^{3+} centres.

Statement 3 Efficiency losses in Mg codoped LuGAGG:Ce originate mainly from nonradiative recombination at Ce related emitting centres rather than from excitation transfer losses.

Statement 4 Low-cost composites consisting of YAG:Ce, LuYAG:Ce, or LuAG:Ce grains in silica matrix have potential for scalable production as scintillators exhibiting bulk-like Ce^{3+} emission spectra, luminescence decay, and quantum efficiency.

Thesis layout

The thesis is composed of an introductory section in which the main research problem, the novelty of the study, and the principal defense statements are presented. This section also provides technical information related to the thesis, including the list of published papers and conference presentations. The literature review is organised into three main parts: (1) physical processes in scintillators, (2) applications of scintillators, and (3) scintillator manufactur-

ing. The experimental methods chapter outlines the photoluminescence, time-resolved photoluminescence, quantum yield, and cathodoluminescence measurement techniques employed in this work. The results are presented across three chapters. Each chapter begins with a short introduction focusing on a specific garnet-based scintillator, followed by the presentation and discussion of the experimental results. Each chapter concludes with a summary and key findings. The first defense statement is presented in the first chapter, the second and third statements are presented in the second chapter, and the fourth statement is presented in the third chapter. Chapter numbering is directly associated with the three publications listed further.

Author contribution

Most of the experimental results and data analysis related to QY, temperature-dependent PL, and decay kinetics were carried out by the author of this thesis. The experimental work and data analysis associated with CL measurements were performed by laboratory colleagues. The author of the thesis also contributed to the preparation of scientific manuscripts that were published based on these results prior to this thesis.

3. LITERATURE REVIEW

3.1. Physical processes in scintillators

A brief scintillators literature review is presented and structured into three main sections: a general overview of scintillators, their areas of application, and the corresponding manufacturing processes. These three major sections are interconnected and are presented with a sequential progression.

A scintillator is generally defined as a material capable of absorbing ionizing radiation and converting the deposited energy into ultraviolet–visible light [5], [6]. The historical development of scintillators is closely associated with the discovery of X-rays at the end of the 19th century. It soon became evident that X-rays would serve as a valuable tool in numerous fields of everyday life, including medicine, security, and scientific research. However, the expanding use of ionizing radiation also required the parallel development of reliable detectors to monitor radiation levels and prevent harmful consequences resulting from overexposure [10]. The first experiments investigating the scintillation process were conducted in the early 20th century by the British chemist and physicist William Crookes, who used zinc sulfide to detect individual α particles [20]. Subsequently, in the mid-20th century, the first scintillator-based detector incorporating a photomultiplier device was developed by Samuel Curran and William Baker. The operating principle of this device is based on the conversion of incident photons into a measurable electrical signal, enabling substantially higher precision compared to visual ("naked-eye") detection [21]. Further progress in the development of scintillator-based detectors for various applications was largely constrained by the limited number of available scintillating materials.

Scintillators can be categorised according to their nature into solid, liquid and gaseous scintillators. The two principal groups of solid scintillators are organic and inorganic. Organic scintillators emit light through molecular excited states after excitation by ionising radiation and typically consist of compounds containing benzene rings [22]. Organic scintillators can be further divided into subgroups of organic crystal scintillators, plastic scintillators and organic liquid scintillators. In the latter, the excitation occurs via the solvent part in the solution [23]. Organic liquid scintillators allow for a wide range of solvent compositions and can be produced in large volumes. However, they

are unsuitable for gamma spectroscopy due to their low atomic number, and quenching processes degrade their scintillation optical performance [24]. In contrast, inorganic scintillators are typically crystals or glasses containing a small amount of activator impurities [25]. Inorganic scintillators are widely used due to their high LY, chemical stability, and mechanical robustness. Existing materials engineering methods, including compositional modification and controlled doping, allow their optical and scintillation properties to be further improved. However, SC growth techniques are expensive, and producing large numbers of homogeneous crystals remains challenging [11], [26], [27]. Gaseous scintillators are less widespread compared to the earlier-mentioned groups, but in the 1980s they were used in nuclear particle detectors that utilise noble gases such as helium, argon, krypton, and xenon or their mixtures [28]. Gaseous scintillators maintain a linear relationship between deposited energy and light output even at high ionisation levels, but mainly emit scintillation light in the UV range and require additional technical systems, such as pressure control and vacuum systems, for detection [29].

In the review by C. Dujardin et al. [11], a comprehensive chart covering the period from the 1940s to 2017 presents the number of newly reported scintillators exhibiting LY over 2×10^4 photons/MeV. A notable observation is that the majority of publications report entirely new compounds, whereas a smaller proportion focuses on previously known host materials modified by introducing new activators or co-doping with additional ions. The review authors attribute a clear increase in the development of new scintillators to two major events: the establishment of the "Crystal Clear Collaboration" (CCC) at CERN in 1990 and the initiation of the international conference "SCINT" in 1992. The rise in the number of newly developed scintillators can also be associated with the broadening range of application requirements. In earlier decades, scintillators were primarily employed in positron emission tomography (PET) and high-energy calorimetry, where key parameters included density, LY, and decay time [11]. In contrast, modern medical imaging techniques, such as time-of-flight PET (TOF-PET), as well as emerging homeland security applications, impose additional, more demanding requirements on scintillator performance characteristics.

As explained earlier, a scintillator is capable of absorbing high-energy radiation (waves or particles) and converting this energy into UV–visible light. This entire energy conversion process can be divided into three main steps: conversion, transport, and luminescence. These three stages are also

illustrated in Figure 1. In the conversion stage, high-energy particles interact with the scintillator material, resulting in the generation of energetic electronic excitations. The interaction mechanism depends on the type and energy of the incident particle. In the case of high-energy photons, three main interaction mechanisms contribute to the initial energy deposition: photoelectric absorption, Compton scattering, and electron–positron pair production [30], [31], [32]. At low photon energies, photoelectric absorption generally dominates, while Compton scattering becomes dominant at intermediate energies, with the relative contributions depending strongly on the composition of the scintillator. Electron–positron pair production becomes energetically possible above 1.02 MeV [30], [33]. In contrast, high-energy charged particles lose energy primarily through Coulomb interactions with atomic electrons, resulting in excitation and ionization of the material [30]. The resulting energetic charged particles initiate a cascade of secondary electronic excitations, resulting in the formation of numerous electron–hole pairs [34]. This process continues until the energy of the electrons falls below the ionization threshold [27], [34]. During the transport stage, the generated charge carriers migrate through the crystal lattice, where their energy can eventually be transferred to activator luminescence centres [35]. During this process, electrons and holes can be captured by luminescence centres, thereby transferring the excitation energy from the host lattice to the activator. The detailed sequence of electron and hole capture depends on the activator and host material. In Ce^{3+} activated scintillators, one possible sequence involves the initial capture of a hole by Ce^{3+}, resulting in the temporary formation of Ce^{4+}. The Ce^{4+} centre can subsequently capture an electron from the CB, forming an excited Ce^{3+} centre, which can undergo radiative recombination [17]. During transport, energy losses may occur through non-radiative processes, while charge carriers can also be temporarily trapped at localized defect states, resulting in delayed radiative processes. In garnet scintillators, such trapping centres can be associated with intrinsic lattice defects, including antisite defects and oxygen-related defects [36]. The efficiency of the transport stage can be strongly affected by material preparation and crystal growth processes [32]. Since carrier transport, capture, and energy transfer contribute to the population dynamics of luminescence centres, these processes can also influence the rise time of the scintillation signal [37], [38]. In the final stage (luminescence), the excitation energy is transferred to a luminescence centre, where it is converted into scintillation photons through radiative relaxation [13]. These luminescence

emission centres arise from a small concentration of activator ions, such as Ce^{3+} or Pr^{3+} centres, incorporated into the crystalline host material [39]. Luminescence originating from such introduced activator ions is classified as extrinsic luminescence. In contrast, intrinsic luminescence does not require an activator and includes mechanisms such as free-exciton, self-trapped-exciton, Auger-free, and self-activated luminescence. In contrast to the rise time, the scintillation decay time is often dominated by the final luminescence stage and depends on the radiative and non-radiative relaxation processes of the excited luminescence centres [30].

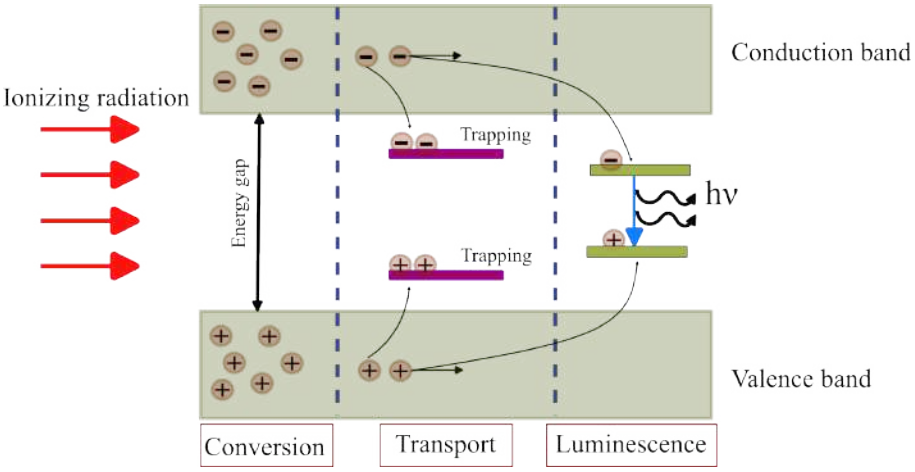

Figure 1. Schematic illustration of the scintillation mechanism in inorganic scintillators. Adopted from [13], [40].

Apart from the classical three-stage description of the scintillation process, the microscopic relaxation of electronic excitations in inorganic scintillators can be divided into five stages: cascade, thermalization, capture, transport, and recombination, as shown in Figure 2 [41], [42], [43]. During the cascade stage, absorption of ionizing radiation generates highly energetic electrons and holes with energies considerably above the corresponding band edges. These energetic carriers undergo inelastic scattering, generating secondary electron–hole pairs and progressively losing their excess energy. A single high-energy primary carrier can generate multiple secondary electron–hole pairs during the cascade process. The number of generated charge carriers per interaction depends primarily on the energy deposited in the scintillator and the energy required for the generation of electronic excitations, whereas the incident radi-

ation intensity mainly determines the number of such interaction events occurring per unit time [44], [45]. Although different types of ionizing radiation ultimately generate energetic secondary electrons in the scintillator, the spatial distribution and local density of the generated electronic excitations can differ substantially between charged-particle and high-energy photon excitation [27]. During the thermalization stage, the remaining energy of the charge carriers is dissipated through phonon emission until electrons and holes approach the CB and valence band edges. Thermalized charge carriers can then be captured by defects or luminescence centres, undergo self-trapping, or form excitons. The duration of the capture stage can also depend on the excitation density. The electron trapping rate can depend on the concentration of holes, and therefore, the total duration of the capture stage can vary with excitation density [43]. During the transport stage, the resulting electronic excitations migrate through the material or transfer their energy toward luminescence centres. Finally, radiative recombination at the luminescence centre results in the emission of scintillation photons. In Figure 2, each stage is associated with a characteristic timescale. The cascade stage occurs approximately within 10^{-16}–10^{-14} s, followed by thermalization within 10^{-14}–10^{-12} s and capture within 10^{-12}–10^{-10} s, while energy transport and recombination generally occur at times longer than 10^{-10} s. The timescale of the final radiative recombination is strongly dependent on the luminescence centre and material. The characteristic timescales therefore generally increase from the ultrafast cascade and thermalization processes toward slower transport and recombination processes. The later stages of the scintillation process generally have the strongest influence on the overall scintillation kinetics [30]. However, these timescales are only approximate, since the individual durations of the early scintillation stages are difficult to determine experimentally due to their extremely short timescales and the limitations of currently available time-resolved techniques. Direct experimental measurements are most readily available for the recombination stage through the scintillation lifetime and for slower transport and energy-transfer processes through the scintillation rise time [41], [42], [43], while ultrafast spectroscopic techniques can also provide information on capture and self-trapping processes in suitable materials.

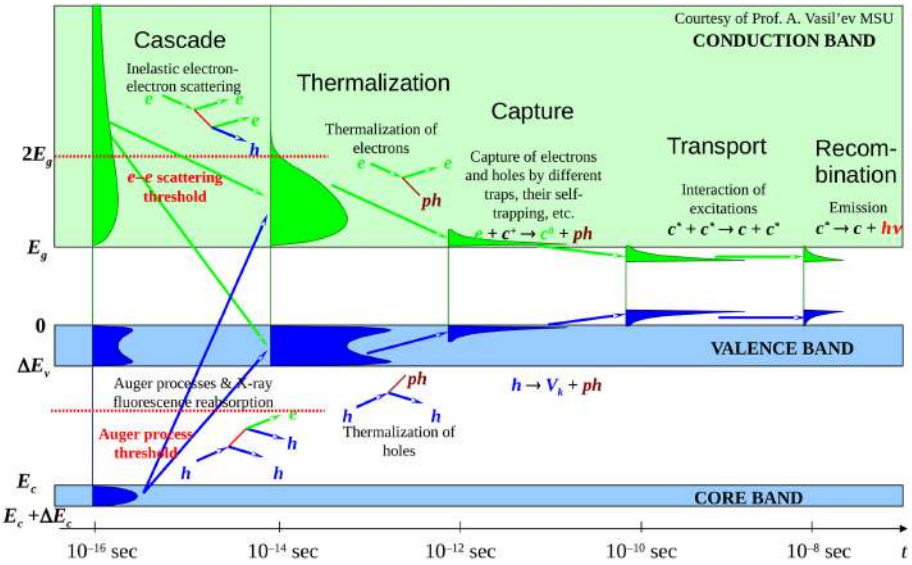

Figure 2. Schematic illustration of the scintillation mechanism in inorganic scintillators. Reproduced from [42].

In this work, the primary focus is placed on inorganic scintillators. These inorganic scintillators can be further divided into several subgroups according to their crystallographic structure. Examples include perovskite-type scintillators (general formula ABO_3), oxyorthosilicate scintillators (Re_2SiO_5, where Re denotes rare-earth elements), pyrosilicates ($Re_2Si_2O_7$), and garnets ($A_3B_2C_3O_{12}$), which are commonly doped with cerium or praseodymium [46]. Initially, the term garnet was used to define a group of silicate minerals found in nature and commonly used as gemstones. Several compositions occur naturally, such as $Mg_3Al_2Si_3O_{12}$ (pyrope), $Ca_3Al_2Si_3O_{12}$ (grossular), and others [47]. Although the term garnet is also widely used to describe these naturally occurring gemstones, they should not be confused with synthetic garnet-structured materials employed as scintillators. Garnet scintillators possess a cubic crystal structure, and their general formula, $A_3B_2C_3O_{12}$, describes a structure in which C-site cations form oxygen tetrahedra, B-site cations form oxygen octahedra, and A-site cations occupy dodecahedral sites within a framework of interconnected tetrahedra and octahedra [12]. The dodecahedral site [A] can be occupied by ions such as Y^{3+}, Gd^{3+}, and Lu^{3+}, while the octahedral site [B] can be occupied by Al^{3+}, Ga^{3+}, Mg^{2+}, and others. The tetrahedral site [C] is typically occupied by Al^{3+} or Ga^{3+} ions. As indicated, the cation distribution may vary depending on the specific composition. The activator ion Ce^{3+}

typically occupies the dodecahedral site, with the site occupancy primarily determined by ionic radius and valence state [47]. Compared with other groups of inorganic scintillating materials, garnets are considered strong candidates for HEP experiments, such as those conducted at CERN. Garnet materials exhibit high density, which is crucial for the efficient detection of high-energy particles. Their host composition can be readily modified, and they allow flexible doping [12]. Previously mentioned trapping effects within the lattice structure, such as those caused by oxygen vacancies, can be mitigated by introducing divalent dopants such as Ca^{2+} or Mg^{2+}. This approach helps to improve the LY and reduce radiative recombination delays [36].

It may seem that only the activator ions (Ce^{3+} or Pr^{3+}) are responsible for the optical properties of garnet-based scintillators. However, the environment surrounding the activator ion significantly influences the luminescence performance, as it determines parameters such as the QY and the scintillation response [39]. The Ce^{3+} ion has a single electron in the 4f shell, giving the ground electronic configuration $4f^1$. Due to spin–orbit interaction, the 4f ground state is split into the $^2F_{5/2}$ and $^2F_{7/2}$ levels. Upon optical excitation, the 4f electron is promoted to the 5d states, which are considerably more sensitive to the surrounding crystal field. In garnet hosts, the 5d states are split by the crystal field into five distinct energy levels, conventionally denoted as $5d_1$–$5d_5$ [47]. The energy diagram of the Ce^{3+} activator ion in different environments is shown in Figure 3. In the free-ion state, a large energy gap of ≈6 eV separates the 4f ground state and the 5d excited states of Ce^{3+}. In a spherical field approximation, a centroid shift is observed, which refers to the downward shift of the 5d energy levels caused by ligand polarisation and covalent interactions with the surrounding anions [36]. When a Ce^{3+} ion is incorporated into a garnet structure, the energy gap between the ground and excited states decreases due to interactions with the surrounding lattice. In highly symmetric but anisotropic coordination environments, crystal field splitting occurs due to the direction-dependent electrostatic potential created by the surrounding ligands. As a result, the Ce^{3+} 5d orbitals split into t_{2g} and e_g components. This effect is particularly pronounced in the dodecahedral crystal field, where the 5d states split into five distinct energy levels. The magnitude of the crystal field splitting is commonly defined as the energy difference between the highest and lowest 5d states [39], [47]. As a combined effect of the centroid shift and crystal field splitting, a red shift of the $5d_1 \rightarrow 4f$ transition occurs.

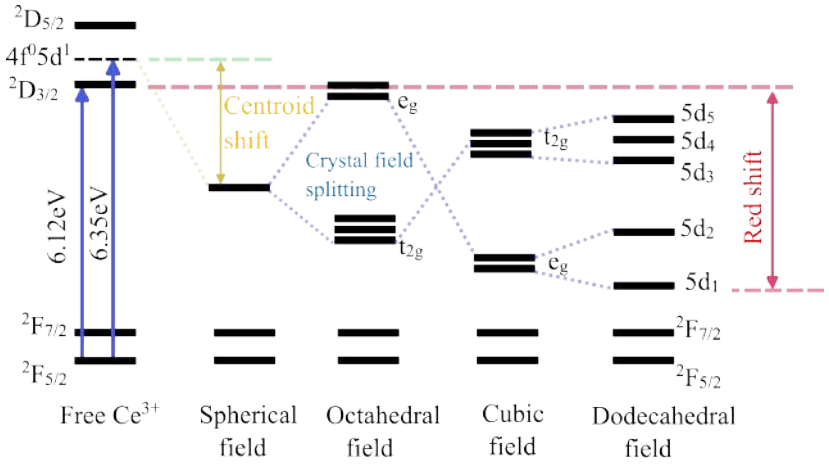

Figure 3. Energy level diagram of Ce^{3+} in the free ion and in various crystal field environments: spherical, octahedral, cubic and dodecahedral. Adopted from [47].

Another important aspect of scintillators is the quenching process. Most of the PL measurements presented in this work are temperature-dependent. The variation of intensity or lifetime with temperature may arise from different mechanisms. It is essential to outline the general aspects of the quenching process in garnet-based scintillators. Several key mechanisms contribute to thermal quenching. One of the most important is the thermal ionisation process (see Figure 4). In this process, an electron located in an excited state of Ce^{3+} (or another activator ion) can acquire sufficient thermal energy from the lattice to overcome the energy barrier separating the excited state from the CB of the host material. The electron is then thermally ionized from the activator centre into the CB. After thermal ionisation, the electron may become trapped at defect centres, from which it can either be thermally released back into the CB or participate in non-radiative recombination [39]. The parameter E_a represents the activation energy required for thermal ionisation to occur.

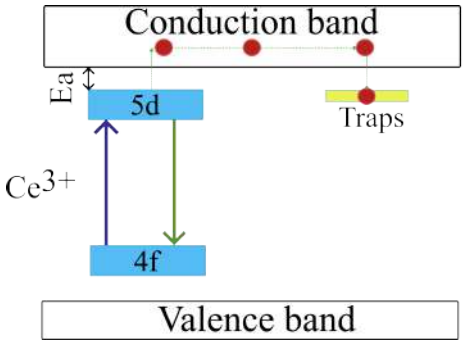

Figure 4. Schematic representation of thermal ionization and charge carrier trapping in the garnet host lattice. Adopted from [39].

An additional process contributing to the general quenching mechanism is known as thermally activated crossover, which is illustrated in Figure 5. This model describes a mechanism in which an electron in the lowest excited state (for Ce^{3+}, the $5d_1$ level) can decay non-radiatively to the 4f ground state. This process occurs through phonon-assisted vibrational excitation, allowing the electron to cross at the intersection point of the corresponding potential energy curves of the excited and ground states [48].

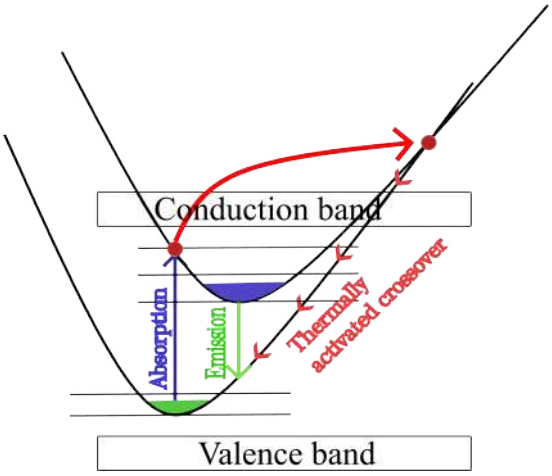

Figure 5. Schematic illustration of the nonradiative relaxation process via a thermally activated crossover. Adopted from [48].

3.2. Applications of scintillators

In the early stages of scintillator detector development, the primary requirement for a scintillating material was mainly high luminescence intensity. However, as the range of applications has expanded, the performance requirements for scintillators have also become more demanding.

Today, three major application areas can be identified where scintillators are widely used: medical imaging, HEP experiments, and security/safety systems. In addition to these primary groups, there are several niche application fields that do not fall strictly within these categories; these will also be briefly discussed.

The application of scintillators in medical imaging began in the 1950s with the development of the Anger gamma camera for two-dimensional imaging [49]. Later, PET enabled three-dimensional imaging and was further advanced by the development of TOF-PET [50], [51]. In conventional PET, the coincident detection of two annihilation γ-rays defines a line of response, whereas TOF-PET uses the difference in their arrival times to estimate the annihilation position along this line [51], [52]. Scintillator development has played a crucial role in improving the performance of both technologies, with sensitivity and spatial resolution being important for PET, while TOF-PET places strong emphasis on timing performance [1]. These performance demands impose several requirements on the scintillator material.

For PET and TOF-PET, the key scintillator requirements are high stopping power, high LY, good energy resolution, and a fast scintillation response. Efficient detection of 511 keV γ-rays requires materials with high density and effective atomic number. Typical TOF-PET scintillator candidates exhibit densities of approximately 5–$7.4\ \mathrm{g/cm^3}$ and effective atomic numbers of approximately $Z_{\mathrm{eff}} = 45$–66 [1], [53]. A high LY, typically around 3×10^4 photons/MeV or higher, provides good photon statistics and contributes to both energy and timing resolution [54], [55]. An energy resolution (which defines the detector's ability to distinguish between different deposited energy values) of approximately 10–12% at 511 keV is representative of commonly used PET scintillators and enables efficient rejection of scattered γ-ray events [56]. The emission of commonly used Lu-based PET scintillators is typically located around 400–450 nm, providing good spectral matching with modern photodetectors [50], [57]. A fast scintillation response becomes particularly important in TOF-PET. Commonly used Lu-based scintillators exhibit sub-nanosecond

rise times and decay times of approximately 30–40 ns. These parameters, together with the LY, determine the coincidence timing resolution (CTR), which in modern TOF-PET systems is typically on the order of a few hundred picoseconds. A shorter CTR improves the precision with which the annihilation position can be estimated along the line of response [51], [55].

Another medical imaging system relying on scintillators is computed tomography (CT), developed in the early 1970s. Unlike PET and TOF-PET, CT uses X-rays transmitted through the human body. During imaging, a rotating X-ray source and detector arrays record attenuation projections at multiple angles, which are reconstructed into cross-sectional and three-dimensional images [2], [3].

Efficient X-ray detection in CT requires scintillators with high stopping power, with densities of approximately $6\ \mathrm{g/cm^3}$ being preferred [58], [59], [60]. A LY exceeding approximately 2×10^4 photons/MeV is desirable to provide a high SNR [61]. Modern CT systems also require decay times below approximately $10\ \mu$s to accommodate high projection sampling rates, while afterglow should remain below approximately 0.1% at 3 ms to prevent residual emission from affecting subsequent projections [61], [62], [63]. In addition, the temperature dependence of the light output should be below approximately $0.1\%/^{\circ}\mathrm{C}$ to maintain a stable detector response during operation [61].

Hadron therapy uses charged particles, such as protons and heavier ions, for cancer treatment [64]. Compared with conventional photon radiotherapy, it enables more precise dose deposition and is particularly advantageous for tumours located near critical organs. Scintillators are mainly used for dosimetry and beam monitoring, requiring high spatial and temporal resolution as well as radiation hardness. High spatial resolution (the ability to distinguish two closely located objects or signals) is important for resolving the steep dose gradients around the Bragg peak (the region where charged particles deposit the maximum amount of energy near the end of their penetration range) [65], with detector dimensions of approximately 0.5 mm or smaller being suitable for proton-beam dosimetry [66]. Fast temporal resolution (the ability to distinguish signals occurring closely in time) enables time-resolved beam monitoring, with nanosecond-scale resolution demonstrated using fast scintillation detectors [67]. High radiation hardness is also desirable to maintain stable performance under prolonged irradiation [68].

HEP investigates matter and its fundamental interactions using particles with energies typically in the GeV range or higher [69]. One of the world's largest

centres for HEP research is CERN [70], where the Large Hadron Collider (LHC) is currently being upgraded to the HL-LHC. The increased collision rate and radiation levels expected at the HL-LHC impose significantly more demanding conditions on particle detectors [4]. Scintillators play an important role in these detectors, and their properties must therefore meet several demanding performance requirements. Scintillators for HL-LHC detectors require high radiation hardness and a fast scintillation response due to the intense radiation environment and high interaction rates. Depending on the detector location, materials may be exposed to radiation doses reaching the MGy range and therefore must retain their optical and scintillation properties under prolonged irradiation [4], [19], [71]. High temporal resolution is particularly important for separating closely spaced events, with the CMS MIP Timing Detector targeting a resolution of approximately 30–60 ps [72], [73]. Short scintillation decay times in the nanosecond range are also desirable to minimise signal overlap and pile-up at high interaction rates [19], [71], [72], [74].

Scintillators are also widely used in security applications, including the detection of special nuclear materials, monitoring of contaminated areas and nuclear facilities, and cargo inspection [11], [75], [76]. These applications require the detection of γ-rays, X-rays, and neutrons, with considerable effort devoted to developing scintillators capable of both single- and dual-mode radiation detection [75], [77]. Scintillators for nuclear security applications require good energy resolution, efficient neutron/γ-ray discrimination, and a sufficiently fast scintillation response. Good energy resolution is particularly important for identifying radioactive isotopes from their characteristic γ-ray energies, with values of approximately 1–2$\%$ at 662 keV reported as desirable for reliable identification of potential fissile sources under moderate count-rate conditions [78]. The ability to discriminate between neutron and γ-ray interactions is also important for detecting and identifying nuclear materials in mixed radiation fields [79], [80]. Fast scintillation decay, typically ranging from a few to several hundred nanoseconds depending on the detector type, enables operation at high count rates and reduces signal overlap [76], [81], [82].

Another security-related application of scintillators is the non-intrusive screening of cargo, luggage, and individuals using X-rays, γ-rays, and, in some systems, neutrons [11], [83]. Scintillators used in these systems require high stopping efficiency, high light output, and low afterglow. Scintillators employed in X-ray security imaging can provide LY of approximately 5×10^4–6×10^4 photons/MeV, enabling high SNR and image contrast [84]. Afterglow and slow

decay components can degrade image quality by causing signal overlap between consecutive X-ray pulses, while decay times of approximately 70–100 ns have been reported for fast garnet scintillators developed for security imaging applications [11], [75]. Dual- or multi-energy detector configurations can additionally be employed to distinguish materials with different effective atomic numbers [85].

In addition to the three major application groups, scintillators are also used in several niche fields, including the manufacture of wLEDs, which relies on phosphor materials. Phosphors used in wLEDs require efficient absorption of the LED excitation, high QY, appropriate emission characteristics, and high thermal stability. Commercial wLEDs commonly employ blue excitation at approximately 450–470 nm, requiring strong phosphor absorption in this spectral region [86], [87]. Highly efficient YAG:Ce-based phosphors exhibit QY values of approximately 90% or higher, with values exceeding 95% demonstrated for high-performance materials [88], [89]. Broad visible emission is required to obtain the desired colour temperature and colour rendering properties [86], [87]. High thermal stability and low thermal quenching are also important to maintain emission efficiency at elevated LED operating temperatures [86].

Several additional application fields of scintillators can be identified. In nuclear logging, ionising radiation, particularly γ-rays, is used for subsurface formation analysis and oil and gas exploration. Scintillators used in these applications require high thermal stability, with operating temperatures exceeding 150 °C, as well as a linear response to γ-radiation [90], [91]. Scintillators are also used in space instrumentation, including satellite-based γ-ray spectroscopy for determining the elemental composition of planetary surfaces. Such applications require stable operation over a broad temperature range (−30 °C to +50 °C) [92], good energy resolution for distinguishing characteristic γ-ray lines, with values of approximately 7% FWHM at 662 keV reported for planetary spectroscopy applications [93], and nanosecond-scale decay times to minimise signal pile-up at high count rates [94], [95], [96].

Table 1 summarises the key scintillator characteristics for the principal application fields discussed above.

Table 1. Comparison of key scintillator characteristics for different application areas.

Applications	**LY/QY**	**Scintillation response**	**Others**
PET/TOF-PET	$\geq 3 \times 10^4$ photons/MeV	Decay: ≈30–40 ns; rise: sub-ns; CTR: few hundred ps	Density: ≈5–7.4 g/cm^3; energy resolution: ~ 10–12% at 511 keV;
CT	$\geq 2 \times 10^4$ photons/MeV	Decay: < 10 μs	Density: ≈6 g/cm^3; low afterglow
Hadron therapy	–	Temporal resolution: ns scale	Spatial resolution: $\lesssim$ 0.5 mm; high radiation hardness
HEP	–	Decay: ns scale; temporal resolution: ≈30–60 ps	Radiation hardness: MGy range
Nuclear security	–	Decay: few ns–several hundred ns	Energy resolution: ≈1–2% at 662 keV; γ/neutron discrimination
Security imaging	≈5–6×10^4 photons/MeV	–	Low afterglow; high stopping efficiency; multi-energy detection
wLED	QY: ≥ 90%	–	Excitation: ≈450–470 nm; broad visible emission; high thermal stability

3.3. Scintillator manufacturing

The suitability of scintillators for different applications is largely determined by their intrinsic properties, including scintillation response, LY, and radiation resistance, which are strongly influenced by the chosen manufacturing process. The garnet-based scintillators investigated in this work were produced using three techniques: the Czochralski method (CZ) (melt growth), liquid-phase epitaxy (LPE), and the sol–gel method (chemical synthesis). These techniques are discussed below in terms of their principles, advantages, limitations, and associated costs, together with a brief overview of alternative synthesis methods.
G. Muller suggests that crystal growth techniques can be broadly classified into three major groups: solution growth, vapour growth, and melt growth. The latter category can be further subdivided into several techniques, including the CZ, Bridgman-Stockbarger (BS), crystal pulling, directional solidification, floating zone, and the Verneuil technique, among others [97].
These techniques enable the growth of bulk single or polycrystalline materials. SCs possess a single crystallographic orientation, whereas polycrystalline materials consist of multiple differently oriented grains. CZ and BS are widely used because they enable the growth of large, high-purity SCs [98], [99]. CZ belongs to the crystal-pulling group [97], [100]. In this method, the material is melted in a cylindrical crucible, and an oriented seed crystal is dipped into the melt and slowly withdrawn while rotating. The crystal shape and diameter are controlled by the heating power, rotation rate, and pulling speed. After growth, the crystal is gradually cooled and annealed to reduce thermal stress. The process is typically performed under vacuum or in a controlled atmosphere [100].
The main advantages and limitations of CZ-grown scintillators are presented below:

+ The CZ method enables the growth of large bulk SCs with a high degree of chemical purity and excellent reproducibility [98], [99], [100], [101].

+ CZ-grown scintillator crystals typically exhibit high optical transparency, enabling efficient transport of scintillation light to the photodetector [98], [99].

– Garnet scintillators have high melting points (≈1700–1970 °C), requiring expensive refractory-metal crucibles and precise temperature control. In addition, large thermal gradients during growth and cooling can induce

thermoelastic stress and crystal cracking [102], [103], [104].

- Differences in ionic radii between host and dopant ions can introduce lattice strain and promote crack formation, while interactions between the melt and crucible may cause contamination that degrades the crystal quality [101], [104], [105].

An alternative melt-growth technique is the BS method. Similar to the CZ method, it employs a crucible containing molten material placed in a high-temperature furnace. In contrast to the CZ method, the BS technique does not involve mechanical pulling or rotation of the crystal from the crucible [106], [107]. As a result, thermoelastic stresses associated with mechanical motion are reduced, which lowers the risk of crack formation during crystal growth. The BS method is also generally more cost-effective due to its simpler growth setup and less demanding temperature-control requirements [108]. However, continuous contact between the melt and the crucible walls increases the risk of impurity incorporation, which can degrade crystal quality. The absence of pulling and rotation limits the control over growth conditions and crystal properties [107], [109].

Another melt-growth technique is the floating zone method. In contrast to CZ, no crucible is used, eliminating contamination from container materials. A polycrystalline feed rod is locally heated to create a narrow molten zone, which is stabilised by surface tension and translated along the rod. As the molten zone moves, the material solidifies on a seed crystal, forming an SC with the orientation defined by the seed [97], [110], [111]. However, the main limitation is the difficulty of producing large-volume crystals, which restricts their use in detector-scale applications.

Moving from bulk crystal production techniques to epitaxial growth, epitaxy in general refers to the formation of a crystalline layer (thin film) on top of a crystalline substrate [112], [113]. This technology is widely used in semiconductor manufacturing, including CMOS (Complementary Metal-Oxide-Semiconductor) technology and light-emitting diodes (LEDs) [113]. In addition, four epitaxial growth approaches can be identified, as shown in Figure 6. In solid phase epitaxy (SPE), a crystalline layer is formed by thermal annealing of an amorphous compound in direct contact with a crystalline substrate [114]. However, SPE is limited to a narrow range of amorphous materials, mainly elemental semiconductors such as silicon and germanium. In the LPE method, which will be discussed in more detail later, crystal growth occurs

from a molten phase that is in direct contact with the substrate [112]. Physical vapor deposition (PVD) is a thin-film fabrication technique capable of producing high-quality films from a wide range of materials. In a typical PVD process, a solid source material and a substrate are placed in a vacuum chamber, where the source material is vaporised. The main limitations are difficulties in achieving uniform deposition and restriction to thin films [115]. Chemical vapour deposition (CVD) is similar to PVD in that it is carried out in a vacuum or low-pressure chamber; however, it differs fundamentally in the use of reactive precursor gases. In CVD, the precursor molecules are transported in the gas phase and undergo chemical reactions or dissociation at the heated substrate surface, where the desired material is deposited [116], [117]. CVD enables high-purity films with good compositional control but is time-consuming and requires costly specialised precursors [118].

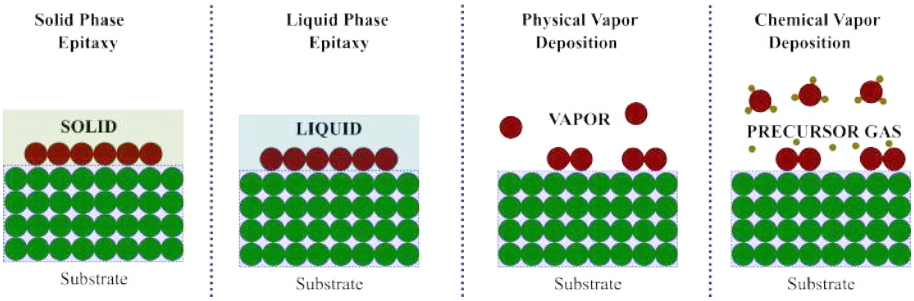

Figure 6. Schematic illustration of four epitaxial growth methods: SPE, LPE, PVD, CVD. Adopted from [112].

As one of the investigated sample series was grown by LPE, this method is described in more detail. LPE can be divided into several subgroups, including sliding, tipping, dipping, and centrifugal force-assisted methods [119]. In all cases, a crystalline substrate is brought into contact with a supersaturated solution, forming a thin crystalline film on its surface. The methods differ mainly in how the substrate interacts with the solution. In the sliding, or boat, technique, a horizontal sample holder moves across the substrate, allowing thin films to be grown on multiple substrate regions [113], [119], [120]. In the tipping technique, the crucible is rotated or tilted, allowing the supersaturated solution to flow over the substrate surface; this approach can also be adapted for multilayer growth [119]. In centrifugal LPE, crucible rotation transports the solution toward substrates positioned along the crucible walls, where epitaxial growth occurs [121], [122]. In the present work, the LPE dipping method was em-

ployed and is therefore of particular relevance. In this technique, the substrate is lowered into a supersaturated solution in a vertical furnace and subsequently withdrawn, forming a thin crystalline film on its surface [123]. The main advantages and limitations of the general LPE technique are summarised below:

+ The LPE method offers high flexibility in film composition and dopant incorporation while providing reduced operational costs due to lower growth temperatures and simpler crucible requirements [121], [123].
+ LPE-grown films exhibit excellent surface morphology and a uniform distribution of activator ions, enabled by lower growth temperatures [119], [123].
– Possible contamination originating from the flux material or from interactions between PbO-based fluxes and platinum crucibles, leading to impurity incorporation [119], [123].
– The structural and optical quality of LPE-grown films strongly depends on the surface quality and defect density of the substrate [121], [123].

The remaining garnet-scintillator production group relies on chemical synthesis, with the sol–gel method being one of the commonly used approaches. As this method was used to prepare one of the investigated sample series, it is discussed in more detail in the following chapters. The sol–gel technique involves the transformation of a sol (solid particles suspended in a liquid) into a gel (a three-dimensional macromolecular network in a solvent) [124], [125]. The process typically begins with precursor preparation, followed by hydrolysis and condensation reactions leading to gel formation. Subsequent thermal treatment removes solvents and promotes crystallisation. Depending on the desired material form, additional steps such as ageing, milling, calcination, sintering, or thermal consolidation may be required [124], [126]. Sol–gel synthesis has been successfully applied to various scintillator materials [127], [128], [129], [130]. The main advantages and limitations of the sol–gel technique are presented below:

+ The sol–gel method offers flexible composition and doping while enabling the fabrication of powders, ceramics, glasses, and composite scintillators [126], [131].

+ Sol–gel processing allows low-temperature preparation of precursor gels, although subsequent heat treatment at higher temperatures is required to obtain crystalline garnet phases [132], [133].

– The processing time can be long due to multiple processing steps, while high-purity metal–organic precursors increase material costs [133], [134].

– Crack formation and structural defects are highly possible in the drying stage, when removing unwanted solvent [135], [136].

Given the limitations of the sol–gel technique, alternative synthesis routes can be considered. One such approach is co-precipitation, in which the solid phase forms directly from a solution without a gel network. The absence of a gel-drying stage can reduce processing time and drying-related issues such as cracking [137]. However, compared with sol–gel synthesis, co-precipitation may provide lower chemical homogeneity, potentially resulting in secondary phases [138].
Similar to earlier presented table of main features for each of the field, in Table 2 a comparison of the main advantages and issues for different scintillators growth techniques.

Table 2. Comparison of scintillator production methods highlighting their key advantages and limitations.

Methods	CZ	LPE	Sol–gel
Key advantages			
Chemical stability	✓		
Optical transparency	✓	✓	
Large crystal size	✓		
Composite flexibility		✓	✓
Cost efficiency			✓
Low process temperature		✓	✓
Thickness control		✓	
Key limitations			
Thermal cracking	✗		✗
Contamination	✗	✗	✗
Dopant segregation	✗		

Scintillators were presented from their fundamental physical principles to their major application domains, including medical imaging and HEP. The performance of a scintillator in a specific application is largely governed by intrinsic material properties, which are, in most cases, directly linked to the chosen fabrication route. While conventional melt-growth techniques enable the production of highly transparent, structurally uniform SCs, they are often associated with significant manufacturing costs. This has motivated the exploration of alternative fabrication strategies, such as epitaxial growth methods and chemically synthesised materials, which offer a possibility to balance performance requirements with technological and economic considerations.

4. EXPERIMENTAL METHODS

In this chapter, the experimental techniques and procedures used to analyse the PL and lifetime characteristics of scintillators are described. Scintillator feature analysis comprises several measurement techniques, including time-integrated PL, TRPL, QY measurements, as shown in Figure 7. CL is presented separately below. In the figure, the QY measurement setup is indicated in brown dashed lines, while PL together with TRPL is shown using green dashed lines. Optical properties were measured at room temperature or using a cryogenic system that enables measurements in the 78–750 K temperature range.

The experimental setup consists of a Yb:KGW laser delivering 170 fs pulses at a wavelength of 1030 nm, coupled with a tunable optical parametric amplifier (OPA). This configuration enables resonant excitation to one of the Ce^{3+} ion energy levels. Photographs of the laser system coupled to the OPA, the optical path leading to the sample position, and the spectrograph together with a streak camera are presented in Figure 8.

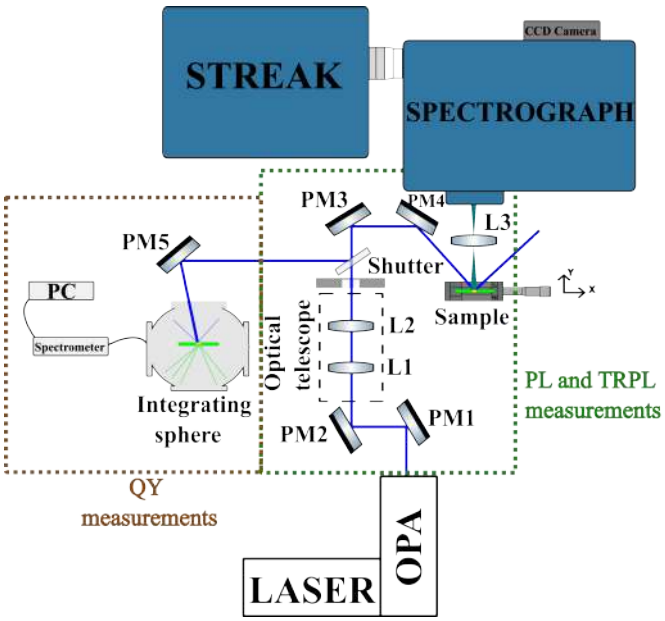

Figure 7. Schematic representation of the experimental setup used for PL, TRPL, and QY measurements.

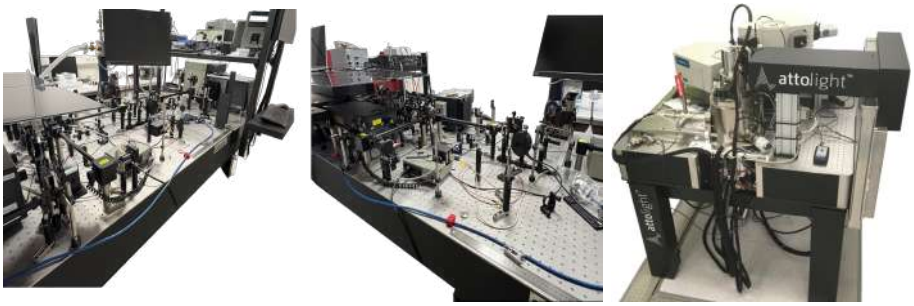

(a) **(b)**

Figure 8. Photographs of the experimental setups used for (a) PL, TRPL, QY and (b) for CL measurements.

Time-integrated PL is a method used to analyse the total emitted light from an excited sample. The PL measurement setup consists of a 328-mm focal-length spectrograph, Kymera 328i, integrated with a Hamamatsu UV-VIS CCD (charge-coupled device) camera. In Figure 7, a schematic of the PL measurement setup is presented. An optical telescope composed of two lenses (L1 and L2) is used to modify the beam diameter. A L3 lens operates in a 2f–2f imaging configuration, forming a real image of the sample at the spectrometer's entrance. The sample's position and height can be adjusted with the sample holder.

TRPL is an experimental technique used to analyse the PL lifetime after excitation. As shown in Figure 7, TRPL measurements are sequentially integrated with the PL measurement setup. The TRPL experiment is performed using a high-resolution Hamamatsu UV-VIS Streak Camera, certified to provide a time resolution of 30 ps. Figure 9 presents the operating scheme of a streak camera. Initially, the incident light is focused through a slit onto a photocathode, where photons are converted into a number of electrons proportional to the initial light intensity. The electrons are then accelerated and directed by electrodes towards a phosphor screen. The collision of the electrons with the phosphor scintillator screen produces an optical image, known as the streak image.

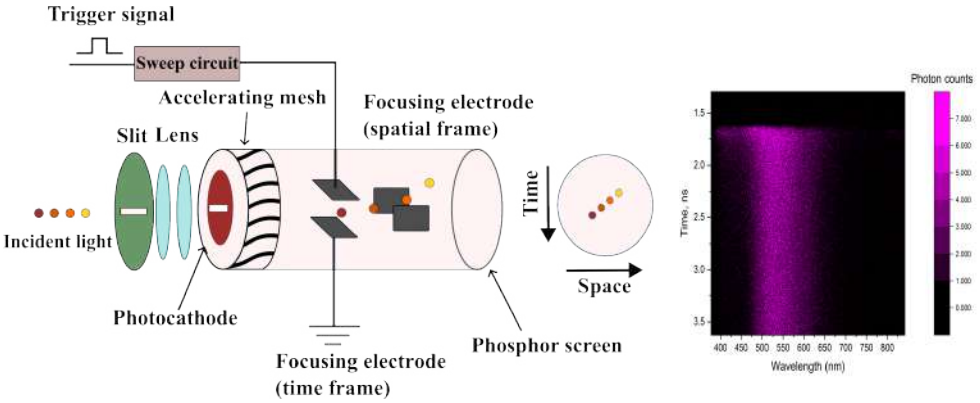

Figure 9. Schematic diagram of the operating principle of a streak camera used for TRPL measurements. Adopted from [139].

The QY is an important scintillator property that defines the ratio of emitted photons to the absorbed ones. In our case, QY experiments were conducted using a 6-inch $BaSO_4$ coated integrating sphere. This measurement provides a straightforward method to determine how efficiently scintillators emit light after excitation. The QY experimental setup is presented in Figure 7. Most of the components remain the same to those used in PL and TRPL measurements, with the addition of a 6-inch integrating sphere.

In Figure 10, a schematic representation of the QY measurement process is presented. It consists of three measurement steps: “Empty sphere”, “Sample out”, and “Sample in” [140]. During the “Empty sphere” measurement, no sample is placed inside the sphere, and only the incident radiation is detected by the spectrometer. In the “Sample out” phase, the sample is not directly aligned with the incident radiation; instead, it is excited by the reflected beam. In the final “Sample in” phase, the measured sample is positioned in the direct path of the incident radiation.

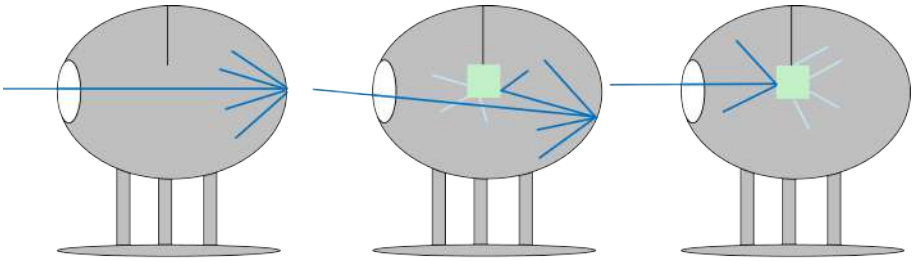

Figure 10. Schematic illustration of the three-step method for QY measurements using an integrating sphere: (a) “Empty sphere”, (b) “Sample out”, and (c) “Sample in”. Adopted from [140], [141].

The (4.1) and (4.2) equations presented below are used to calculate the absolute value of QY using the three-step method. The variables in these equations are obtained by calculating the integrated areas, as illustrated in Figure 11.

$$QY = \frac{P_c - (1 - A_{dir})P_b}{L_a A_{dir}} \tag{4.1}$$

$$A_{dir} = 1 - \frac{L_c}{L_b} \tag{4.2}$$

L_a number of photons in the laser line region when no sample is present;
L_b number of laser line photons when the sample is out of the direct pathway of the incident radiation;
L_c number of laser line photons when the sample is in the direct pathway;
P_a number of photons in the emission region when no sample is present;
P_b number of photons in the emission region when the sample is out of the direct pathway of the incident radiation;
P_c number of photons in the emission region when the sample is in the direct pathway.

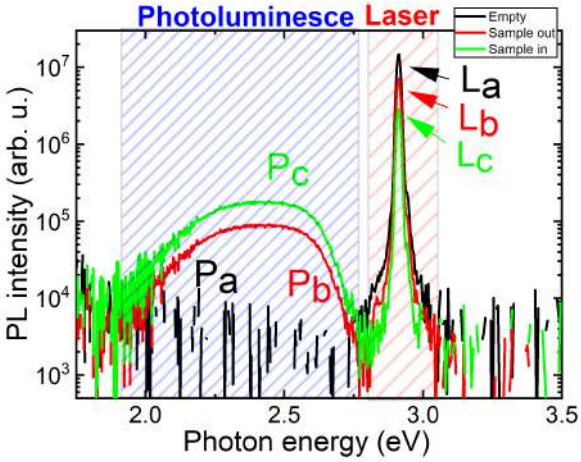

Figure 11. Graphical representation of the integrating-sphere three-step method for QY determination based on PL spectra of the ”Empty sphere”, ”Sample out”, and ”Sample in” configurations.

Currently used CL measurement techniques combine scanning electron microscopy (SEM) with a CL detector to analyse the sample's emission spectrum under electron-beam (e-beam) excitation. Figure 12 shows a schematic of the SEM combined with a Chronos high-resolution time-resolved CL detection system developed by the Attolight company. The current system enables measurements with spatial, spectral, and temporal resolution. An aeroPULSE PL, NKT Photonics laser is used to trigger the electron gun. The luminescence signal is collected using a Cassegrain-type objective connected to a spectrometer (iHR 320, Horiba). For spatial map detection, an Andor Newton 920 CCD camera is used, while a Hamamatsu C10910 streak camera is used to measure the CL time evolution. The Chronos system also allows the study of surface morphology in SEM mode.

Briefly describing the basic working principles of the CL experiment: first, electrons emitted by the electron gun are accelerated at a voltage of 10 kV and directed onto the surface of the sample under investigation. When interacting with the material, the incident electrons lose energy through inelastic scattering and initiate cascades of secondary electronic excitations, resulting in the generation of multiple electron–hole pairs per incident electron. Since the energy of the incident electrons is considerably higher than the band-gap energy of the investigated materials, the excitation is not selective to a single optical transition; instead, the electron energy is progressively transferred through

multiple inelastic interactions [142], [143]. The excitation of the activator ions and the following radiative relaxation leads to photon emission. The emitted CL light is collected by the optical system and directed to the CCD and Streak cameras. The current CL setup also includes an integrated laser system, which enables measurements to be performed in two different regimes: continuous and pulsed. In the continuous regime, constant excitation allows the analysis of the intensity and spectral distribution across the entire microstructure. While the pulsed regime provides information about the emission decay kinetics and enables lifetime mapping.

In most cases, PL and CL experimental results are compared, as they complement each other. In PL measurements, Ce^{3+} centres are excited resonantly by promoting an electron directly from the Ce^{3+} 4f ground state to one of its 5d excited states [144]. In contrast, CL primarily excites the host lattice, generating nonequilibrium charge carriers whose transport and subsequent energy can populate the Ce^{3+} emission centres. Therefore, comparison of PL and CL measurements provides information on processes associated with carrier transport, trapping, and energy transfer to the Ce^{3+} centres, as well as on differences in the resulting luminescence kinetics.

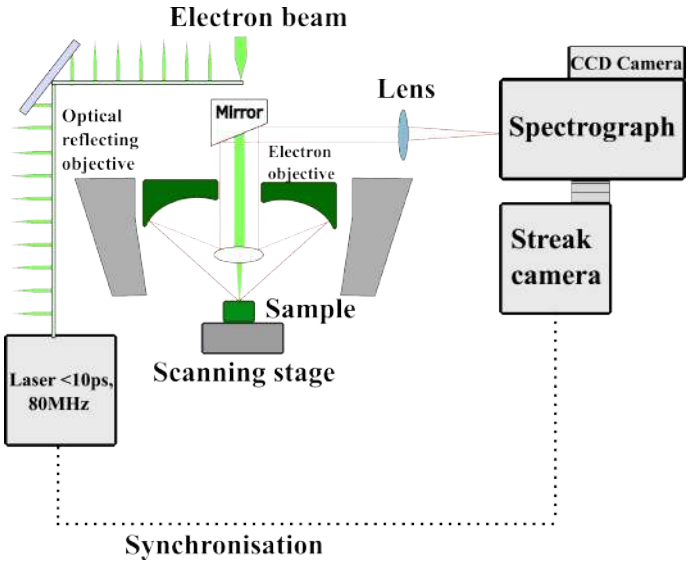

Figure 12. Schematic diagram illustrating the operating principle of the CL experimental setup. Adopted from [145].

Excitation-relaxation processes in

$Y_3(Al_{1-x}Ga_x)_5O_{12}$:Ce

Yttrium aluminium garnet doped with cerium is considered to be one of the first Ce^{3+}-activated garnet scintillators, developed in 1967 for flying-spot cathode-ray tube applications [146]. $Y_3Al_5O_{12}$ as a host crystal possesses a cubic structure, and the ionic positions can be expressed by the formula $A_3B_2(CO_4)_3$. Y^{3+} occupies the dodecahedral site coordinated by eight oxygen atoms, while 2/5 of the Al^{3+} ions occupy octahedral sites coordinated by six oxygen atoms, and the remaining 3/5 of the Al^{3+} ions occupy tetrahedral sites coordinated by four oxygen atoms [147]. When Ce^{3+} is incorporated into the host lattice, it substitutes Y^{3+} in the garnet structure. YAG:Ce is one of the most widely used scintillators in everyday applications, ranging from being an essential component in white LED structures that replace incandescent lamps and fluorescent tubes on the market [47], to applications in medicine for detecting beta or X-ray intensity. In the white LED industry, a simple combination of a blue InGaN chip with cerium-doped phosphors is typically employed [148]. This scintillator has a broad range of applications due to several advantageous properties, including high LY, high density, and excellent chemical and mechanical stability. In HEP, YAG:Ce could also be considered for applications in future colliders. Currently used scintillators containing heavy elements, such as lead tungstate $PbWO_4$, suffer from radiation damage caused by high-energy hadrons. Therefore, next-generation scintillators are expected to consist of materials containing ions with intermediate atomic numbers, which provide improved resistance to radiation damage [149].

Several technical parameters characterize YAG:Ce scintillators. The emission maximum is located around 550 nm, while the emission spectrum covers the range of 500–700 nm. The typical decay time is ≈ 70 ns [150], and the photon yield reaches 3×10^4 photons/MeV at 300 K [151]. The internal quantum efficiency is reported to be as high as 99.5 % [152].

As the CZ method has already been briefly introduced in the literature review, only a short reminder of its main steps is provided here. In this technique, the feed material is melted in a crucible, and a seed crystal is brought into contact with the melt surface to initiate crystallisation at the seed–melt interface. The crystal is then slowly pulled upward, typically while rotating, and its diameter and morphology are controlled by adjusting the thermal conditions, pulling rate, and rotation speed [97].

Still, alongside the mentioned advantages, YAG:Ce scintillators also face several challenges that limit their wider implementation in HEP field. The currently observed decay time of YAG:Ce samples is ≈ 70 ns, which needs

to be reduced for applications in HEP experiments [19]. The relatively slow scintillation response of YAG:Ce scintillators are influenced by electron trapping mechanisms. These traps capture and temporarily hold charge carriers, leading to deterioration in both the efficiency and the scintillation response of the scintillator. The origin of these traps is still under discussion, but several possible sources have been proposed, including oxygen vacancies [153], antisite defects [154], and self-trapped excitons [155].

There are two main approaches to addressing the trap-related issues in YAG:Ce scintillators. The first approach involves the stabilization of Ce^{3+} to Ce^{4+} through codoping with divalent ions such as Mg^{2+} or Ca^{2+} [155]. Since the first crystal growth experiments, considerable time has been required to achieve a fundamental understanding of the processes associated with the stabilization of Ce^{4+} [18], [156]. Ce^{4+} centres can capture electrons to form excited Ce^{3+*} ions, which then emit photons. This pathway can reduce trapping-related delays, while Ce^{3+}+Mg^{2+} pairs can introduce faster luminescence decay components. As discussed in the literature review, the rise time and decay time of a scintillation pulse are governed by different physical processes. The rise time is mainly influenced by carrier transport, capture, and energy transfer to the luminescence centres, whereas the decay time is often dominated by the radiative and non-radiative relaxation of the excited luminescence centres. Another approach to improving the scintillation response of YAG:Ce scintillators is to implement a bandgap engineering strategy.

To address existing electron-trapping issues, band-gap engineering offers an alternative approach. This strategy involves the incorporation of substituent ions into the crystal lattice, thereby modifying the position of the Ce^{3+} emission levels through control of the band-gap size and crystal-field strength [15]. In this way, existing electron traps can be effectively “buried” in the CB illustrated in Figure 13. Incorporation of gallium into another scintillator, gadolinium aluminum gallium garnet (GAGG), proved to be successful [157]. In the case of YAG:Ce scintillators, the incorporation of gallium in small amounts, up to a certain threshold value, leads to a noticeable improvement in the existing limitations [149]. Gallium ions substitute Al^{3+} ions at the tetrahedral sites, increasing the LY by approximately 30%, as reported by Sidletskiy et al. [16]. However, further introduction of Ga ions results in somewhat different scintillation behaviour.

The incorporation of gallium allows modification of the emission wavelength,

which is particularly important for the LED market due to changes in the crystal field [148], [149]. Other studies report that further incorporation of gallium leads to a pronounced persistent luminescence effect, extending the afterglow duration from several minutes to nearly hours [158].

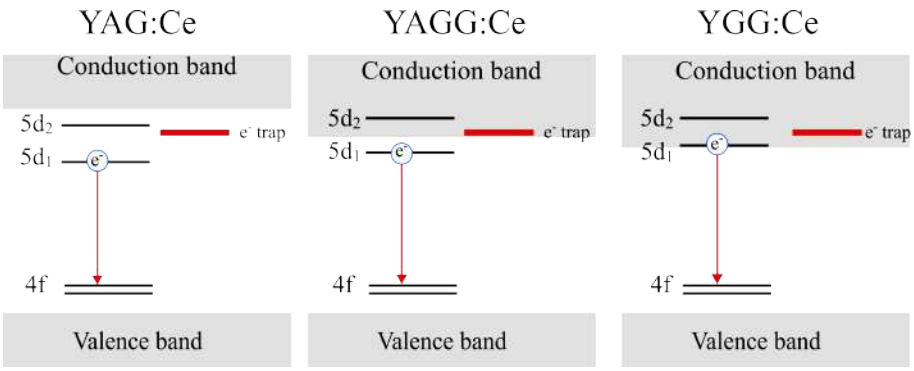

Figure 13. Schematic illustration of the influence of band-gap engineering on the positions of Ce^{3+} excited states in $Y_3(Al_{1-x}Ga_x)_5O_{12}$:Ce as a function of Ga content x. Adopted from [149].

Although YAG:Ce, as a garnet scintillator, has been widely used in industry and extensively studied in research for a considerable period of time, several unresolved questions remain relevant. For example, it is still unclear whether thermally activated crossover quenching is the dominant mechanism responsible for the luminescence quenching. Another open question is whether the centroid shift has a significant influence on the red-shift of the $5d_1$ state [47]. In this chapter, the optical properties of a set of samples with progressively increasing gallium incorporation into the YAG:Ce lattice were investigated, covering the entire range from 0% to 100%.

5.1. Samples

Eight samples of $Y_3(Al_{1-x}Ga_x)_5O_{12}$:Ce (YAGG:Ce), with varying Ga content x ranging from 0 to 1, specifically x = 0.00, 0.16, 0.36, 0.66, 0.75, 0.80, 0.85, and 1.00, were investigated. These samples were provided by colleagues from a group led by *Oleg Sidletskiy* from the Institute for Scintillation Materials NAS in Ukraine. The samples were grown using the CZ method in an iridium crucible. For crystal growth, Y_2O_3, Al_2O_3, Ga_2O_3, and CeO_2

oxides were used as raw materials. With 1 mol.% CeO_2 added to the melt, the resulting Ce^{3+} concentration in the samples was approximately 0.1 at.% relative to Y^{3+} and was kept constant throughout the investigated series. The growth was carried out in an Ar atmosphere with 1% oxygen to prevent melt evaporation. Subsequently, the crystals were annealed at 1500 °C in an oxygen atmosphere to compensate for oxygen vacancies that may have formed during the growth process.

YAGG:Ce samples were characterised using the previously defined measurement methods: PL, TRPL, CL, and QY. PL and TRPL measurements were performed in the temperature range of 90–750 K using a liquid-nitrogen cryogenic system.

5.2. Results

Initially, absorption spectra were measured for all eight samples and are presented in Figure 14. Two main distinctive bands can be observed, corresponding to the optical transitions between the ground state 4f and the two excited states, $5d_1$ and $5d_2$, of the Ce^{3+} ion. The incorporation of gallium alters the crystal-field strength and the energy-level separations (see Figure 15) [39]. Increasing incorporation of Ga into the lattice structure leads to a decrease in the energy difference between the two excited states, $5d_1$ and $5d_2$, from $\Delta E = 0.93$ eV to $\Delta E = 0.54$ eV. As reported in the literature, ΔE reflects changes in the crystal field strength at the dodecahedral sites of the lattice structure [47]. The excitation band corresponding to the $5d_1$ state exhibits a blue shift, whereas the $5d_2$ band shows a red shift. This behaviour observed in YAGG samples is explained as the result of a balance between several competing processes, primarily the centroid shift and crystal field splitting, as discussed by J. Ueda et al. [47].

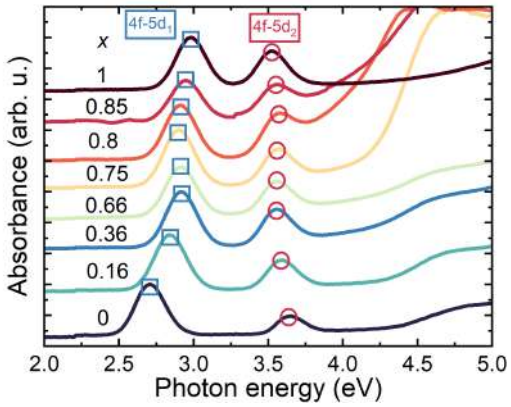

Figure 14. Absorption spectra of $Y_3(Al_{1-x}Ga_x)_5O_{12}$:Ce samples with different Ga content x.

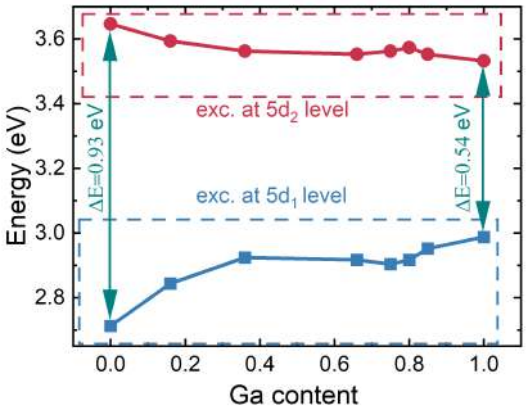

Figure 15. Ce^{3+} $5d_1$ and $5d_2$ level energy positions as a function of Ga content in $Y_3(Al_{1-x}Ga_x)_5O_{12}$:Ce samples.

PL spectra were investigated in the temperature range from 90 to 750 K. The samples were excited resonantly according to the absorption peak positions in the absorption spectra corresponding to the two excited states, $5d_1$ and $5d_2$. In Figure 16, the emission spectra of all measured samples are presented for each 100 K temperature interval under excitation to the $5d_1$ excited state. PL spectrum consists of two overlapping bands, which is explained by the optical transitions from the $5d_1$ state to the two ground states $F_{7/2}$ and $F_{5/2}$. The incorporation of gallium in the range of x = 0.16–0.66 results in a higher PL signal intensity, which is clearly observed in the 90–500 K temperature range. This enhancement may be associated with reduced

defect-related nonradiative losses at Ce^{3+} centres, as discussed below. With further increases in temperature up to 750 K, thermal quenching becomes more pronounced, particularly in gallium-containing samples, as the barrier to thermal depopulation is progressively reduced.

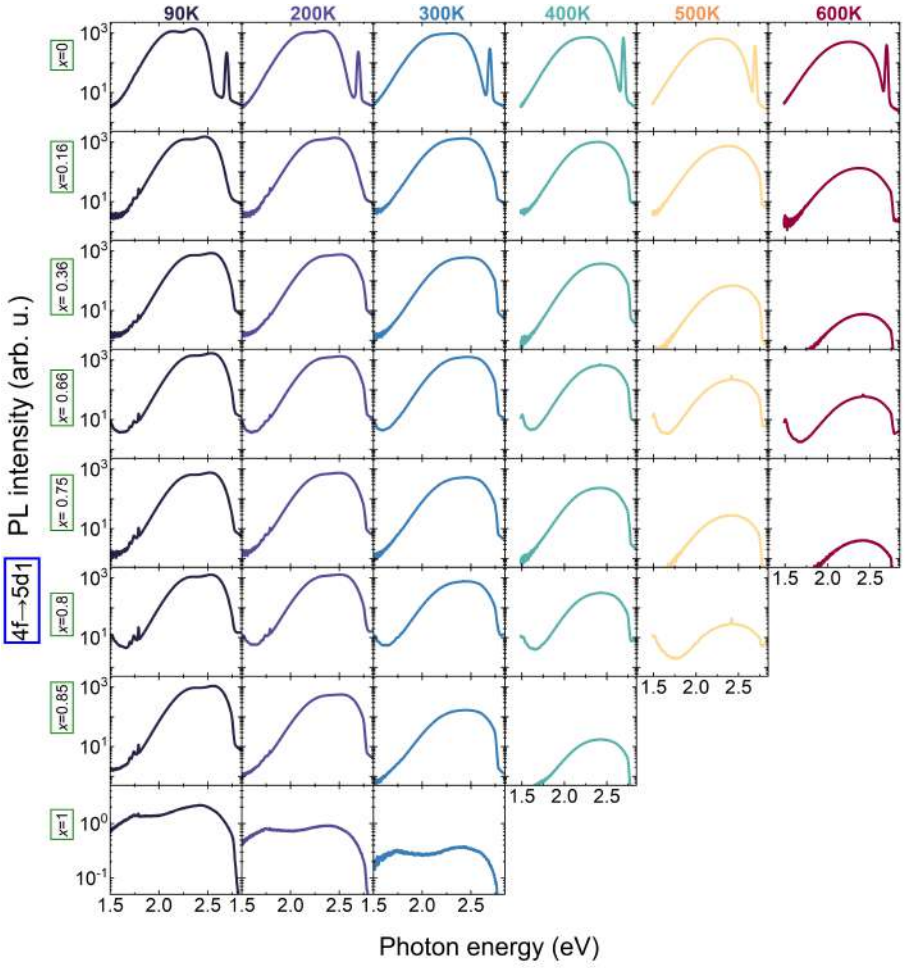

Figure 16. Temperature-dependent PL spectra of $Y_3(Al_{1-x}Ga_x)_5O_{12}$:Ce samples excited at the Ce^{3+} $5d_1$ level.

Not only do electron traps influence the emission properties. Defects in the lattice structure may act as electron traps or non-radiative recombination centres, both of which reduce luminescence efficiency. When such defects are located in the vicinity of a Ce^{3+} ion, non-radiative recombination centres, often

referred to as “dark Ce ions”, can be formed. These centres do not participate in the radiative recombination process. Instead, they capture nonequilibrium electrons or absorb photons during resonant excitation. As the number of such captured electrons or absorbed photons increases, the luminescence efficiency correspondingly decreases. The incorporation of gallium can potentially reduce the number of these “dark Ce ions”. However, when the gallium concentration exceeds approximately $x > 0.66$, Ga ions perturbed by Ce^{3+} ions or by electron traps may introduce energy levels below the CB. These levels can act as non-radiative channels for electrons from the excited states, thereby contributing to additional luminescence quenching.

Figure 17 shows the temperature-dependent PL spectra of three samples (x = 0, 0.85, and 1) under resonant excitation into the Ce^{3+} $5d_1$ and $5d_2$ states. At the lowest temperature (90 K), the spectrum is clearly dominated by two overlapping emission bands, as explained earlier, due to optical transitions from the $5d_1$ state to the two ground states. With increasing temperature, the spectral shape gradually changes due to the broadening of these two bands. However, no noticeable shift in the emission peak position is observed with increasing temperature. The general spectral features remain similar for both excited states, although their intensity dependence on temperature exhibits different behaviour.

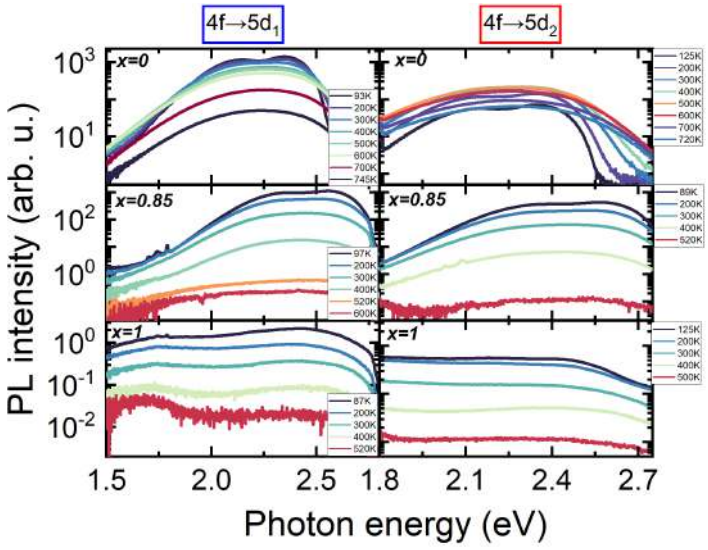

Figure 17. Temperature-dependent PL spectra of $Y_3(Al_{1-x}Ga_x)_5O_{12}$:Ce with different Ga content x at excitation to Ce^{3+} $5d_1$ and $5d_2$ levels.

Figure 18 shows the temperature dependence of the spectrally integrated PL intensity, obtained by integrating the Ce^{3+} emission band at each temperature. An important feature is the steepness of the intensity decrease, which, when analysed using an Arrhenius fit, provides the activation energy, a key parameter that defines the barrier height for thermal depopulation of emitting level. The activation energy was estimated using the Arrhenius equation, assuming that the temperature dependence of the PL intensity is governed by thermal depopulation of the emitting level over a single energy barrier E_a (see (5.1)). The PL intensity temperature dependence shown in Figure 18 was fitted using the (5.1) equation for samples with gallium content up to $x = 0.66$ for both Ce^{3+} excited states. For higher gallium concentrations, the thermal quenching mechanism becomes more complex, probably including more than one barrier. The activation energy values estimated from the PL intensity are presented in the first column of Table 3. A general overview of the obtained activation energies will be discussed after analysing the PL kinetics.

$$V = \frac{V_0}{1 + A \cdot \exp\left(-\frac{E_a}{k_B T}\right)} \tag{5.1}$$

V_0 is the intensity at the low temperature ($k_b T \ll E_a$);
A is the fitting constant;
k_b Boltzmann constant.

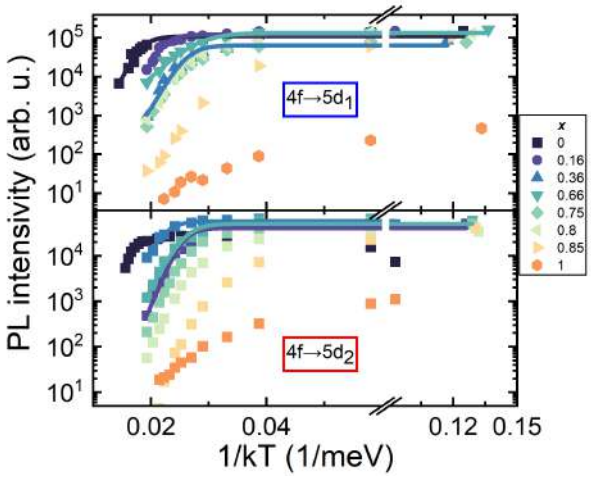

Figure 18. Temperature dependences of PL intensity of $Y_3(Al_{1-x}Ga_x)_5O_{12}$:Ce samples at excitation to Ce^{3+} $5d_1$ and $5d_2$ levels.

The decay kinetics were evaluated at the emission band peak position over the entire temperature range of 90–750 K. The results are illustrated in Figure 19. For both excitation conditions, $5d_1$ and $5d_2$, three samples with different gallium contents are presented. For gallium-free sample, excitation to the first $5d_1$ state results in a lifetime (time value defining the exponential decay of the emitted light intensity following excitation) of 55 ns at room temperature. As the temperature increases to 745 K, the lifetime decreases to 18 ns. In gallium-free sample, the temperature dependence of the lifetime is primarily governed by thermal quenching processes. In contrast, samples with higher gallium content (x = 0.85) exhibit a lifetime of 13 ns at room temperature, which decreases to sub-nanosecond values, reaching 0.9 ns at 600 K. A similar behaviour is observed in the same Figure 19 (right panel) for excitation to the second Ce^{3+} excited level, $5d_2$. For gallium-free sample, the lifetime at room temperature is also 55 ns, decreasing to 12 ns at 745 K. In the sample containing gallium (x = 0.85), the lifetime is 10 ns at room temperature and decreases to 0.7 ns at 520 K, which represents the highest temperature at which reliable measurements could be obtained under excitation to the $5d_2$ state due to the dominance of thermal quenching. In contrast, under excitation to the $5d_1$ state, reliable measurements for the same sample were possible up to 600 K. Samples with the low gallium content are well described by a single-exponential fit over the entire temperature range. However, with

increasing gallium content, deviations from single-exponential behaviour are observed. Fitting results are presented in Figure 20, which shows the temperature dependence of the PL decay time, analogous to the previously discussed PL intensity dependence. Fitting using equation (5.1) was applied to the four samples with the lowest gallium content. The activation energies derived from the decay-time analysis are presented in the second column of Table 3.

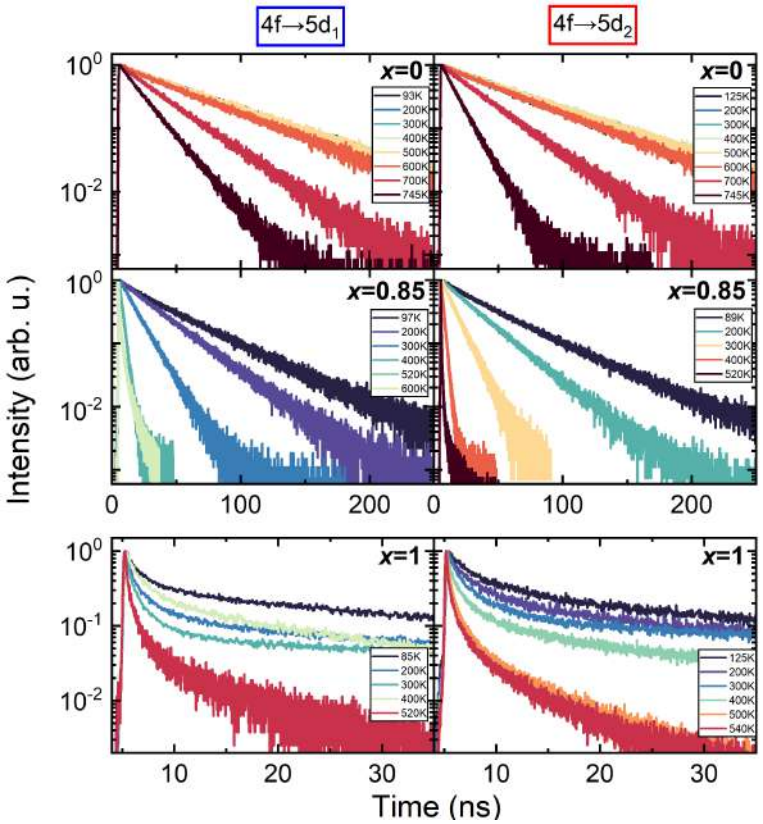

Figure 19. Temperature-dependent decay of normalized PL of $Y_3(Al_{1-x}Ga_x)_5O_{12}$:Ce samples at excitation to Ce^{3+} $5d_1$ and $5d_2$ levels.

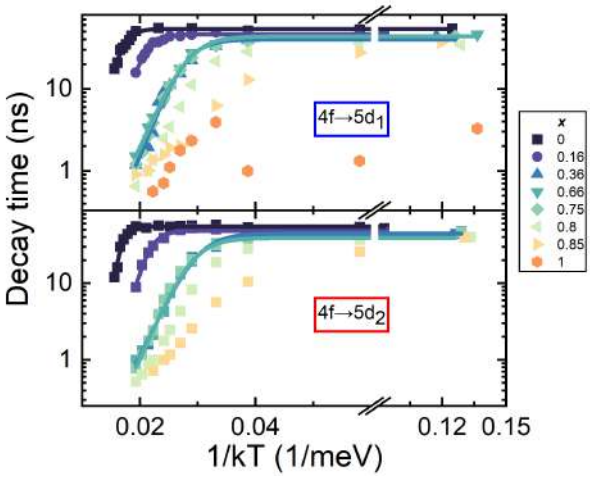

Figure 20. Temperature dependences of PL decay of $Y_3(Al_{1-x}Ga_x)_5O_{12}$:Ce samples at excitation to Ce^{3+} $5d_1$ and $5d_2$ levels.

Based on Table 3, the activation energy values obtained from PL and TRPL measurements are in good agreement. The uncertainties in the activation energies E_a represent the standard errors obtained from the nonlinear least-squares fitting of the experimental data using the Arrhenius model. As discussed earlier, incorporation of gallium into the lattice structure serves as band-gap engineering, shifting the positions of the excited-state energy levels of activator Ce^{3+} ions. In this case, the Ce^{3+} excited states $5d_1$ and $5d_2$ shift closer to the CB edge. As a consequence, the activation energy decreases, leading to more pronounced thermal quenching. This effect becomes particularly evident at higher temperatures.

Table 3. Activation energies E_a (meV) from PL intensity and 1/e analyses of $Y_3(Al_{1-x}Ga_x)_5O_{12}$:Ce samples with different gallium content at excitation to Ce^{3+} $5d_1$ level.

x	E_a (meV); intensity	E_a (meV); decay time
0	684 ± 94	681 ± 63
0.16	628 ± 85	642 ± 60
0.36	534 ± 49	421 ± 29
0.66	333 ± 31	386 ± 14

The temperature dependence of PL intensity and decay time reveals that, in samples with low gallium content, thermal quenching is governed by a single energy barrier. In contrast, samples with gallium content above $x = 0.66$ exhibit more complex PL intensity temperature dependence, probably including more than one quenching channel. The PL intensity can therefore be influenced by two possible quenching mechanisms: the already mentioned thermal quenching, caused by the reduced barrier for thermal depopulation, and potentially the intracenter non-radiative decay process. The activation energy associated with the intracenter non-radiative decay can be evaluated using (5.2) presented below [159]:

$$E_{a,int} = \frac{\left(E_{2\,F_{5/2}\rightarrow 5d_1} - S\hbar\Omega\right)^2}{4S\hbar\Omega} \tag{5.2}$$

$E_{2,F_{5/2}\rightarrow 5d_1}$ is the energy of the transition $^2F_{5/2} \rightarrow 5d_1$ without phonon interaction. The phonon-free transition energies were estimated by subtracting $S\hbar\Omega = 0.24$ eV from the absorption peak energies. The obtained $E_{2,F_{5/2}\rightarrow 5d_1}$ values range from 2.47 eV to 2.75 eV for gallium content varying from 0 to 1; S is the Huang–Rhys factor, with $S = 6$ [160];
$\hbar\Omega$ is the optical phonon energy. The value $\hbar\Omega = 40$ meV was obtained from the fits of the cerium absorption spectra. The obtained minimal value of $E_{a,int}$ is 5.18 eV. The parabolic branches of the Ce^{3+} $5d_1$ and $^2F_{5/2}$ levels intersect deep within the CB, as shown in the literature review in Figure 5. It shows that intracenter non-radiative decay is not feasible under resonant excitation conditions. The activation energies presented in Table 3, estimated using two different methods, confirm that the thermal quenching process of the excited electrons dominates over intracenter non-radiative decay, as it requires a significantly lower activation energy.
As mentioned earlier, QY experiments allow the estimation of the number of photons emitted by the activated Ce^{3+} ions relative to the number of absorbed photons. The results of the QY measurements with excitation to both $5d_1$ and $5d_2$ levels are presented in Figure 21. Considering the results for excitation to the $5d_1$ level, the QY value slightly increases with gallium content up to $x = 0.66$ and then rapidly decreases with further gallium incorporation. Several authors explain this behaviour by the preferential occupation of lattice sites by gallium ions. At low concentrations, gallium tends to substitute Al^{3+} ions in the tetrahedral sites. Once the tetrahedral sites become largely occupied, gal-

lium begins to substitute Al^{3+} ions in the octahedral sites of the lattice structure [161]. The most pronounced increase in the QY value is observed in the range between the samples with $x = 0$ and $x = 0.16$.

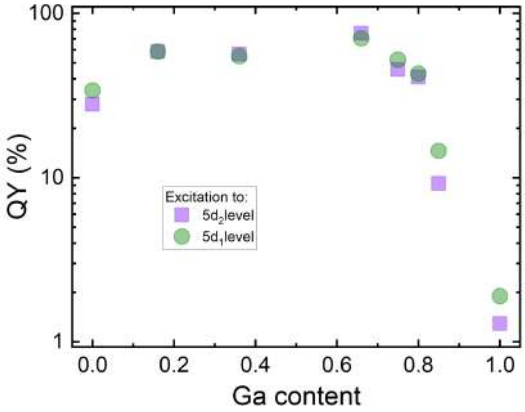

Figure 21. The QY of $Y_3(Al_{1-x}Ga_x)_5O_{12}$:Ce samples as a function of a Ga content at excitation to Ce^{3+} $5d_1$ and $5d_2$ levels.

The CL experiments were performed with a temporal resolution of 100 ps. The electrons used to excite the samples were accelerated at a voltage of 10 kV. The electron gun was triggered by sub-10-ps pulses from a laser system to generate short electron pulses. The CL spectra are presented in Figure 22. In the energy interval of 2.0–2.5 eV, the emission spectrum of Ce^{3+} is observed. A blue shift of the main CL band is detected with increasing gallium content. In most samples, the Ce^{3+} emission dominates; however, in the sample where gallium fully replaces aluminium (YGG), this emission becomes hardly detectable. In the same YGG sample, a new emission band appears with a peak at approximately 2 eV.

An additional CL peak is observed at 3.8 eV, which is most intense in the gallium-free sample. In the range $0.16 \leq x \leq 0.85$, this peak is significantly suppressed, but it appears again for the $x = 1$ composition.

Earlier studies using synchrotron radiation [162], [163] have reported an additional emission band around 3.8 eV that cannot be attributed to the typical $5d_1 \rightarrow 4f$ emission of Ce^{3+} observed in the 2.0–2.5 eV range. The spectra observed in the CL measurements are therefore interpreted as radiative recombination of excitons associated with antisite defects Y_{Al} (where a Y^{3+} ion occupies a lattice site normally associated with Al^{3+}) or as luminescence originating from F^+ centres.

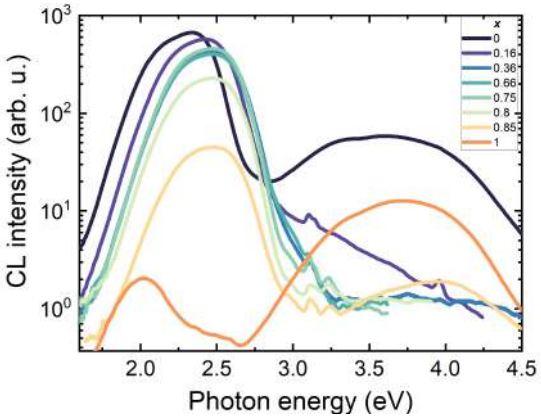

Figure 22. CL spectra of $Y_3(Al_{1-x}Ga_x)_5O_{12}$:Ce samples with varying Ga content x.

In Figure 23, the normalized CL decay kinetics are presented. With increasing gallium content, the CL decay becomes significantly faster. The decay time was estimated using the time interval over which the intensity decreases by a factor of $1/e$. In gallium-free samples, the decay time reaches 92 ns, whereas in samples with gallium content $x = 0.85$, the decay time decreases to approximately 2 ns.

In comparison with earlier measurements performed using X-ray excitation [16] and synchrotron radiation [161], no increase in intensity within the x = 0.4–0.5 range was observed (see Figure 22). This behaviour can be explained by the nonlinearity of the CL response resulting from the higher excitation density.

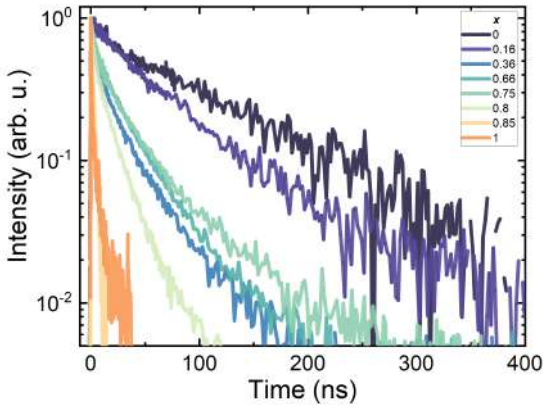

Figure 23. Normalized CL decay kinetics of $Y_3(Al_{1-x}Ga_x)_5O_{12}$:Ce samples with varying Ga content x.

In Figure 24, the dependence of the CL intensity on the gallium content is analysed for different e-beam currents. At the initial stage of gallium incorporation, up to $x = 0.16$, an increase in CL intensity is observed. This effect is more pronounced at lower e-beam currents. In contrast, for samples with higher gallium content ($x = 0.8$), a significant decrease in CL intensity is registered, which becomes more evident at higher e-beam currents.

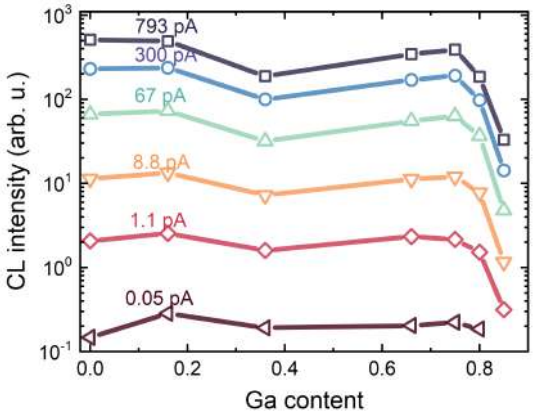

Figure 24. CL intensity of $Y_3(Al_{1-x}Ga_x)_5O_{12}$:Ce samples with varying Ga content x under different e-beam current.

To test the previously described assumption regarding the presence of nonlinearity, a study of the excitation intensity dependence of the CL intensity was conducted. The results are presented in Figure 25. The probe current shown

on the X-axis was adjusted by defocusing the e-beam onto an aperture, while the excitation spot size remained constant. The dependence of the CL intensity $I(j)$ on the probe current j is non-linear and can be approximated by the relation $I(j) \propto j^{\alpha}$. Here, the power factor α decreases from 0.84 to 0.71 as the gallium content increases from $x = 0$ to $x = 0.85$. Thus, higher gallium content leads to a stronger deviation from linear dependence on the excitation intensity.
A weak nonlinearity was also observed in the dependence of PL intensity on excitation intensity at the highest excitation levels. The PL measurements were conducted in the excitation intensity range of 4 μJ/cm^2 to 20 mJ/cm^2, and a sublinear dependence was identified only above 10 mJ/cm^2.
A typical explanation for nonlinear processes in scintillators is the saturation of trapping centres or certain non-radiative recombination centres. However, in the case of YAGG samples, such a mechanism would lead to a different behaviour, namely a superlinear dependence of emission intensity on excitation intensity. Therefore, the observed sublinear dependence can instead be interpreted as a result of saturation of the Ce^{3+} ion centres. As shown in Figure 25, the CL intensity dependence on the probe current can be described by the same power law $I(j) \propto j^{\alpha}$ over a wide current range (50 fA to 800 pA).
Although CL excitation involves the main processes relevant to scintillation following high-energy particle excitation, including charge-carrier generation, relaxation, transport, and subsequent energy transfer to the Ce^{3+} luminescence centres, the applied 10 kV CL excitation conditions do not directly reproduce those encountered in specific scintillator applications. In particular, the deposited energy, its spatial distribution, and excitation density may differ from those produced by higher-energy particles under actual operating conditions. Differences in excitation energy and the resulting ionization density can modify the scintillation kinetics and the scintillation response [164].

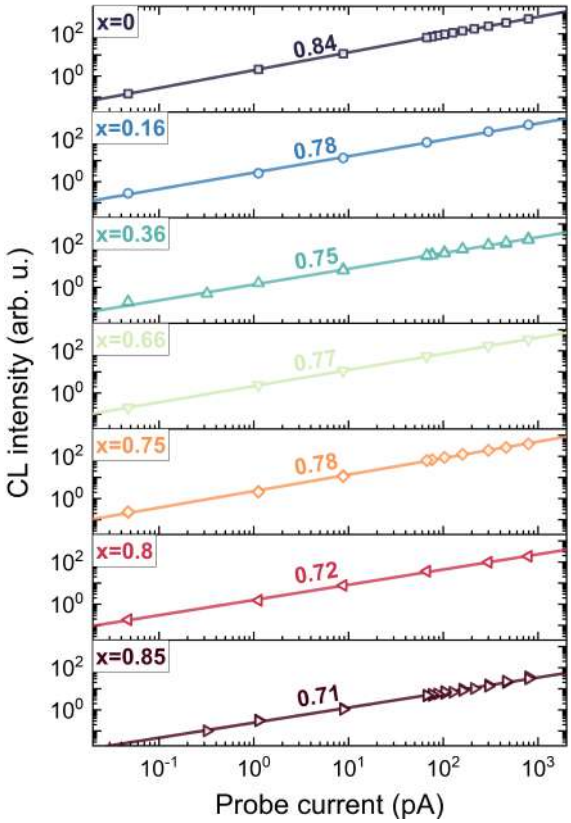

Figure 25. Dependences of CL intensity on e-beam current in $Y_3(Al_{1-x}Ga_x)_5O_{12}$:Ce samples with varying Ga content x. Lines represent the best fits of the dependence with power law $I(j) \propto j^{\alpha}$.

In Figure 26, the QY and decay time are presented for each analysed sample. The highest QY among the investigated samples is observed at $x = 0.66$, while the decay time decreases with increasing gallium content. Both the luminescence efficiency and decay characteristics are relevant when considering the timing performance of scintillation detectors. The CTR is commonly used to quantify the precision with which the time difference between two coincident detections is measured.

Since a shorter decay time and a higher light output are both favorable for timing performance, combining these parameters provides a useful figure of merit for assessing the expected timing performance. Using experimental data, CTR can be expressed as CTR $\propto \sqrt{\tau/N_{ph}}$, where τ is the luminescence decay time and N_{ph} is the number of detected photons [1], [165]. The spectrally and tem-

porally integrated CL intensity was used as a relative measure of the number of detected photons N_{ph}, while τ corresponds to the CL decay time. Therefore, the ratio $\sqrt{\tau/N_{ph}}$ was evaluated and is presented in the Figure 26. The lowest $\sqrt{\tau/N_{\mathrm{ph}}}$ value was obtained at a Ga content of $x = 0.80$, indicating the potentially best timing performance within the investigated series. However, this improvement is accompanied by a substantial decrease in QY compared with $x = 0.66$, where the highest QY was observed. Above $x = 0.66$, the luminescence efficiency decreases. Therefore, $x \sim 0.7$ can be considered a favorable compromise between timing performance and luminescence efficiency.

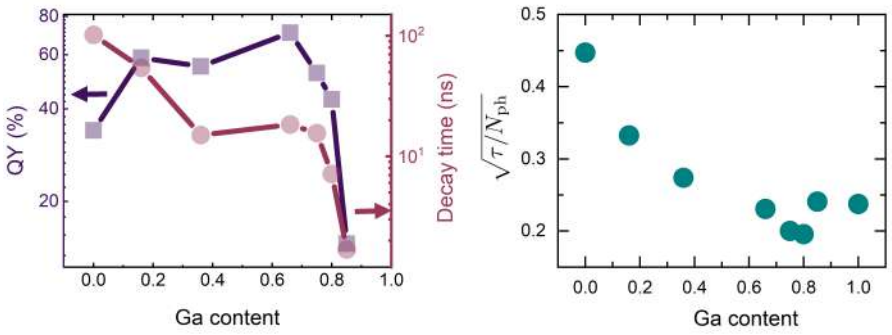

Figure 26. QY (squares, left axis) and decay time (circles, right axis) in $Y_3(Al_{1-x}Ga_x)_5O_{12}$:Ce with varying Ga content *x*. The right panel presents the $\sqrt{\tau/N_{ph}}$ values as a function of varying Ga content.

5.3. Summary and highlights

Highlights:

- Gallium incorporation modifies the band structure by lowering the CB edge, thereby suppressing the influence of shallow electron traps and simultaneously reducing the activation energy for thermal quenching.
- The influence of shallow traps is reduced with gallium incorporation, up to $x = 0.16$.
- Gallium incorporation in the range $0 < x < 0.7$ reduces the concentration of the "dark Ce ions", thereby improving luminescence efficiency.

Key findings:

- Incorporation of gallium in scintillator $Y_3(Al_{1-x}Ga_x)_5O_{12}$:Ce up to $x \sim 0.7$ decreases the barrier for thermal depopulation of Ce^{3+} emitting level and results in reduced ratio between luminescence decay time and light yield, ensuring improvement of timing performance of the scintillator. Further increase in gallium content leads to drastic performance deterioration.

Excitation-relaxation processes in

$(Lu_xGd_{1-x})_3(Ga_yAl_{1-y})_5O_{12}$:Ce,Mg

For a scintillating material to be implemented in the field of medical imaging or HEP experiments, a fast scintillation response is expected. For a scintillating material to be used in SEM detection, pixel dwell times of approximately 100 ns or shorter may be required depending on the acceptable image contrast [166]. For an e-beam inspection system, the requirements should not exceed 10 ns and ideally should be even shorter [167]. The essential parameters are the lifetime (1/e decay time) and the afterglow effect. Longer decay times result in more blurred images, while the presence of afterglow further degrades image contrast [168]. Plastic scintillators are widely considered a cost-effective and fast solution for producing scintillators with a fast scintillation response. However, these advantages are accompanied by a major drawback: plastic scintillators degrade rapidly under e-beam irradiation [169].

Several candidates are considered for applications in the previously defined fields. One of the primary candidates is Ce-doped oxyorthosilicates [17], such as ($Lu_{2(1-x)}Y_{2x}SiO_5$) (LYSO), which exhibit a decay time of approximately 36 ns, a high density of 7.1 g/cm^3, and a high light output of 3.3×10^4 photons/MeV [170]. Cerium-doped LYSO scintillators are currently used in modern PET systems. Another candidate is the garnet-based scintillator family. It is expected that a garnet-based scintillator ($Gd_3(Ga, Al)_5O_{12}$:Ce) will be implemented in future experiments of the Large Hadron Collider beauty (LHCb) at CERN. As another well-known example of a garnet-based scintillator, lutetium aluminium garnet ($Lu_3Al_5O_{12}$:Ce), commonly referred to as LuAG, can be considered. In its standard form, LuAG scintillators exhibit a decay time exceeding ≈70 ns, a density of 6.73 g/cm^3, and a light output of 2.5×10^4 photons/MeV [171]. Garnet-based scintillators offer flexibility in incorporating additional codopants. This allows electronic band-gap engineering and improves the scintillation response. For example, in Ce-doped LuAG:Ce scintillators, the simultaneous introduction of gadolinium and gallium cations into the lattice has been shown to mitigate the influence of shallow electron traps [172].

Aliovalent codoping refers to the incorporation of an ion with a different valence state from that of the host ion it substitutes. The resulting charge imbalance requires compensation, which can alter the defect structure and the valence state of activator ions [173]. These modifications can be exploited to tailor luminescence and charge-carrier transport in scintillators. At relatively low codopant concentrations, this approach has been shown to improve the scintillation response by facilitating excitation transfer and suppressing the influence of carrier trapping [174]. Aliovalent codoping with Ca^{2+} or Mg^{2+} ions is also

employed to improve luminescence properties [13], [17]. In oxyorthosilicate scintillators such as LYSO and GAGG garnets, a faster scintillation response has been associated with the stabilization of a fraction of Ce ions in the Ce^{4+} oxidation state. The presence of Ce^{4+} in such aliovalently codoped materials has been confirmed using X-ray absorption near-edge structure (XANES) spectroscopy [18], [175]. In XANES measurements, the incident X-ray energy is scanned across an element-specific absorption edge, where core electrons are excited into unoccupied electronic states. The spectral features near the absorption edge are sensitive to the oxidation state of the investigated element and can therefore be used to distinguish between Ce^{3+} and Ce^{4+}. In Mg-codoped GAGG:Ce, additional spectral features characteristic of Ce^{4+} were observed at the Ce L_{III} edge compared with Mg-free samples, providing evidence for the stabilization of Ce^{4+} [175]. For the garnet-based LuAG scintillator, in addition to the suppression of shallow electron traps, the stabilization of Ce^{4+} has also been proposed as a mechanism contributing to a faster scintillation response [36]. The radiative recombination process involving Ce^{4+} ions is presented below in (6.1) and (6.2). Initially, Ce^{4+} captures an electron and becomes an excited Ce^{3+*} state. In the second step, Ce^{3+*} emits a photon and returns to the Ce^{3+} ground state:

$$Ce^{4+} + e^{-} \rightarrow Ce^{3+*} \tag{6.1}$$

$$Ce^{3+*} \rightarrow Ce^{3+} + h\nu \tag{6.2}$$

The antisite defects observed in CZ-grown crystals arise from the high temperatures required during the growth process. To overcome the resulting delays in the scintillation response, researchers employ not only suitable codoping strategies but also alternative growth techniques, such as the previously defined LPE method. This method is performed at significantly lower temperatures and does not require post-growth mechanical processing such as polishing or cutting; therefore, it avoids the introduction of additional defects that could degrade the crystal's scintillation properties [168]. In this case, thin-layer films were grown on a CZ-grown substrate using the isothermal dipping LPE methodology [176]. The general principles of the LPE method were briefly introduced earlier; therefore, only the specific procedural steps relevant to the

present study are described in this section. Garnet films can be grown using $PbO–B_2O_3$, $BaO–B_2O_3–BaF_2$, and $MoO_3–Li_2MoO_4$ fluxes. The thin films were grown from a flux in a platinum crucible. The CZ-grown substrate was attached to a rotating holder and immersed in a supercooled melt. After growth, the substrate was withdrawn from the melt, and the residual flux was removed by rapid rotation [123]. In this study, $Lu_{0.8}Gd_{2.2}Ga_{2.5}Al_{2.5}O_{12}$:Ce,Mg (LuGAGG) samples were grown using the LPE method with heavy codoping of magnesium ions. Codoping is typically effective when small amounts of divalent ions up to a few hundred ppm are introduced. At high aliovalent codopant concentrations, the average distance between codopant and activator ions decreases, increasing the probability of codopant ions being located in close proximity to the activator centres [177]. Such close association can modify the local electronic environment of the emission centres, and introduce additional recombination pathways resulting in changes in their luminescence properties and decay kinetics.

The aim of this study is not only to analyse the influence of heavy aliovalent codoping on the optical properties but also to determine whether the stabilization of Ce^{4+} is responsible for the accelerated luminescence decay in LuGAGG samples.

6.1. Samples

In this study, six LuGAGG samples with different magnesium contents were analysed, as presented below in Table 4. The samples were obtained through a collaboration with the research group of *Miroslav Kučera* from the Faculty of Mathematics and Physics at Charles University in Prague.

LuGAGG samples were grown using the isothermal dipping LPE method on a CZ-grown $Gd_3Ga_{2.7}Al_{2.3}O_{12}$ substrate with a $BaO–B_2O_3–BaF_2$ flux. Using this method, it is possible to incorporate cerium up to 1 atomic % due to the higher segregation coefficient. A larger amount of dopants can be introduced compared to the classical CZ method without damaging the crystalline lattice [178], [179]. The epitaxial layers of the LuGAGG samples contain a constant cerium concentration of 1 %. The layer thickness is approximately 16 μm. The concentrations of cerium and magnesium ions are expressed relative to the number of ions occupying the dodecahedral site to enable comparison. The magnesium content was determined using glow discharge mass spectrom-

etry (GDMS) for one of the samples and calculated for the remaining samples based on the melt composition using the segregation coefficient $k_{Mg} \approx 0.06$. Unintentional impurities, structural defects, and the concentration of Ce ions are assumed to be nearly identical, as the samples were grown from the same melt under identical growth conditions. This enables a direct comparison of their properties.

Table 4. Mg content (ppm) in LuGAGG:Ce, Mg samples.

LuGAGG:Ce,Mg
Mg content (ppm)
0
35
300
700
2200
6000

6.2. Results

In Figure 27, the optical absorption spectra of the LuGAGG samples are presented. As mentioned earlier, the nominal total Ce content in each sample is the same, while the differences arise from the introduction of magnesium. The main absorption peaks are observed at 2.84 eV (corresponding to the $4f$–$5d_1$ transition) and 3.65 eV (corresponding to the $4f$–$5d_2$ transition). The absorption bands become weaker with increasing magnesium content. Such results may be attributed to the transformation of the emission centre from Ce^{3+} to Ce^{4+}, as reported for other magnesium-codoped scintillators such as LYSO:Ce, Mg [18] and LuAG:Ce, Mg [180]. Samples 0 ppm and 6000 ppm represent two extreme cases. The Mg-free sample (0 ppm) exhibits well-defined cerium-related absorption peaks. In contrast, the 6000 ppm sample, with the highest magnesium content, shows very weak cerium-related absorption bands, possibly due to the earlier defined stabilization of Ce^{3+} into Ce^{4+}. Sharp lines observed in the ≈3.95–4.1 eV range are attributed to gadolinium ions.

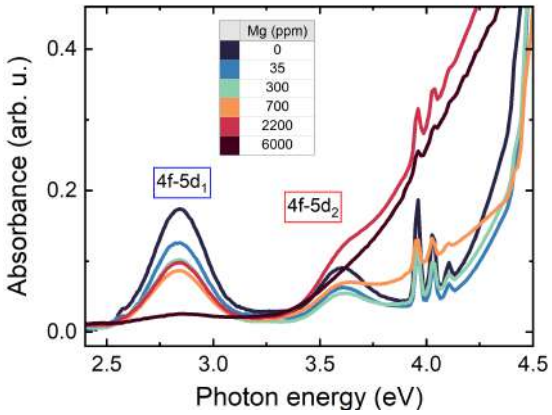

Figure 27. Absorption spectra of LuGAGG:Ce, Mg samples with different Mg content.

For LuGAGG samples, the QY was measured to determine how heavy codoping with Mg affects the number of emitted photons relative to the absorbed ones. The experimental results for different LuGAGG samples under excitation to both the $5d_1$ and $5d_2$ levels are presented in Figure 28. Magnesium incorporation leads to a decrease in PL intensity, and for samples with magnesium content above 2200 ppm the QY value becomes hardly measurable. In Table 5, the absolute QY values are presented for both excitations. A more pronounced decrease in QY is observed when the magnesium concentration exceeds approximately 300 ppm.

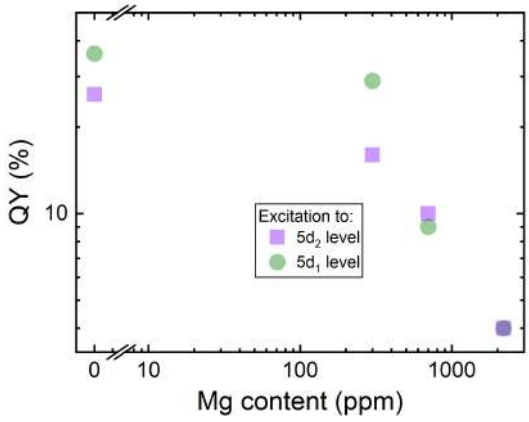

Figure 28. The QY of LuGAGG:Ce, Mg samples as a function of Mg content at excitation to Ce^{3+} $5d_1$ and $5d_2$ levels.

Table 5. The QY of LuGAGG:Ce, Mg samples at excitation to Ce^{3+} $5d_1$ and $5d_2$ levels.

Sample, Mg content [ppm]	QY with the excitation to the $5d_1$ level, %	QY with the excitation to the $5d_2$ level, %
0	36	26
300	29	16
700	9	10
2200	4	4

In Figure 29, the PL spectra of all samples measured at room temperature are presented for excitation to both the $5d_1$ and $5d_2$ states. Further analysis will focus only on the samples containing 0, 300, 700, and 2200 ppm of Mg, as no PL signal could be registered from the sample containing 6000 ppm of Mg.

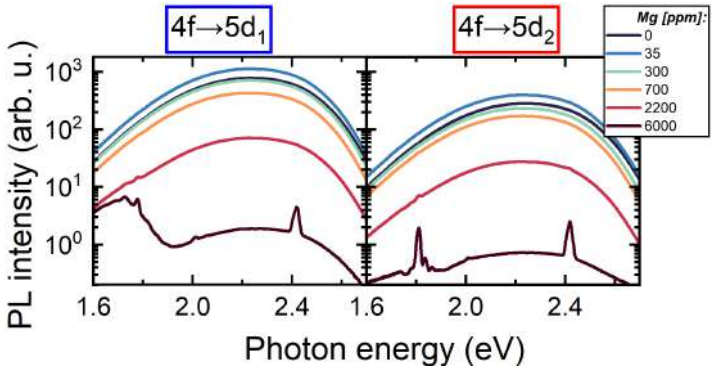

Figure 29. PL spectra of LuGAGG:Ce, Mg samples at room temperature with the excitation at Ce^{3+} $5d_1$ and $5d_2$ levels.

The temperature dependence of PL spectra was investigated in the 80–600 K temperature range, as shown in Figure 30. At lower magnesium concentrations, the PL intensity remains relatively unchanged, whereas further incorporation of Mg above 700 ppm results in a significant reduction in PL intensity. At ≈80 K, the PL intensity reaches its maximum value due to the suppression of thermal ionization, which becomes dominant at higher temperatures.

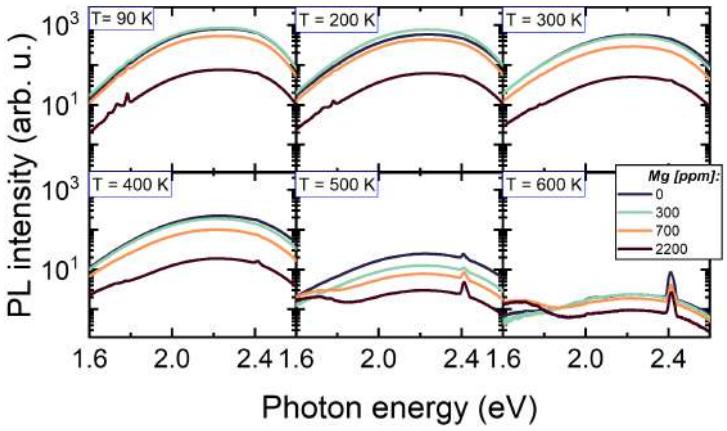

Figure 30. Temperature-dependent PL spectra of LuGAGG:Ce, Mg samples measured at 100 K intervals with the excitation at the Ce^{3+} $5d_1$ level.

In Figure 31, a more detailed PL(T) dependence is presented for each sample separately under excitation to both the $5d_1$ and $5d_2$ levels. A broad asymmetric emission band, characteristic of Ce^{3+} ions, is observed. This asymmetry originates from the optical transition from the $5d_1$ excited state to the two ground states $^2F_{7/2}$ and $^2F_{5/2}$. The minor peaks near 2.4 eV are not intrinsic to the sample but are introduced by the experimental setup. Heavy codoping with magnesium does not alter the energy levels of the excited states and has no observable effect on the emission band position of the LuGAGG samples.

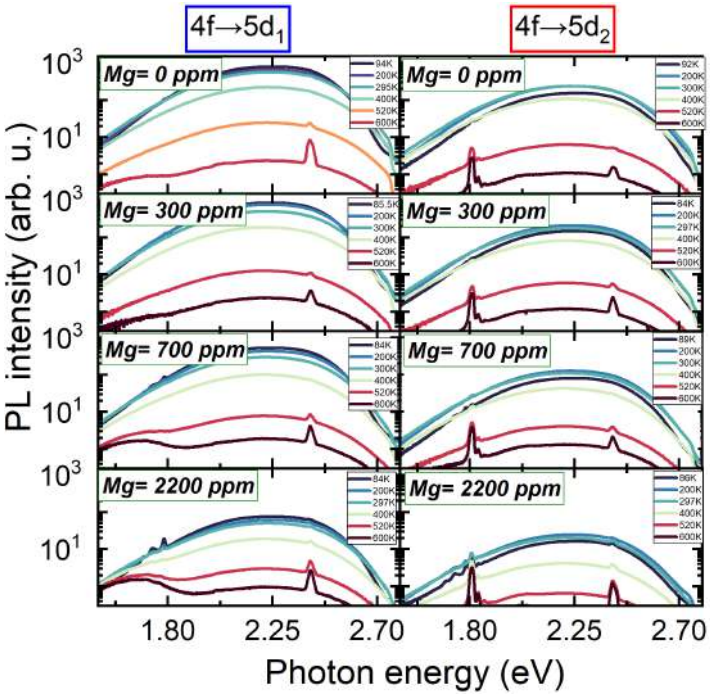

Figure 31. Temperature-dependent PL spectra of LuGAGG:Ce, Mg samples excited at the Ce^{3+} $5d_1$ and $5d_2$ levels.

The temperature dependence of the spectrally integrated PL intensity for both excitations is presented in Figure 32 as an Arrhenius plot, using the (5.1) equation, similarly to the analysis performed in the previous chapter for YAGG samples. The activation energies estimated from the Arrhenius fitting of the PL intensity temperature dependence are listed in Table 6 for both excitation pathways. The variation of PL intensity with temperature is governed by the thermal depopulation of the emitting level over a single energy barrier.

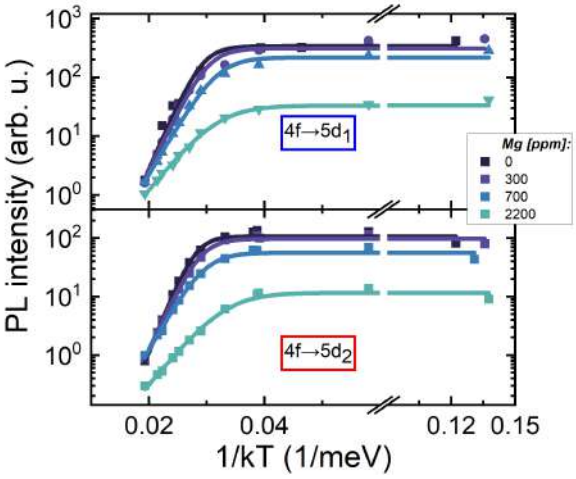

Figure 32. Temperature dependences of PL intensity of LuGAGG:Ce, Mg samples at excitation Ce^{3+} $5d_1$ and $5d_2$ levels.

Figure 33 presents the normalized PL decay curves of LuGAGG samples measured at various temperatures under both excitation conditions. For the samples without magnesium, the decay is close to a single-exponential behavior over the temperature range of 90–600 K. As the magnesium concentration increases, a faster decay component becomes more pronounced. For excitation to the $5d_1$ state in the magnesium-free sample, the lifetime at room temperature reaches approximately 42 ns, while at 600 K it decreases to below 1 ns as a result of thermal quenching processes. In contrast, for the sample with the highest magnesium concentration, the lifetime at room temperature is approximately 10 ns, and at the highest temperature (600 K) it reaches a sub-nanosecond value. As shown above, increasing the Mg concentration does not result in a noticeable shift of the Ce^{3+} emission spectrum. Despite the nearly unchanged spectral position, a substantial acceleration of the emission decay is observed with increasing Mg concentration. The temperature dependence of the lifetime for the LuGAGG samples is presented in Figure 34 as an Arrhenius plot, and the activation energies estimated from the lifetime (1/e) are summarized in Table 6.

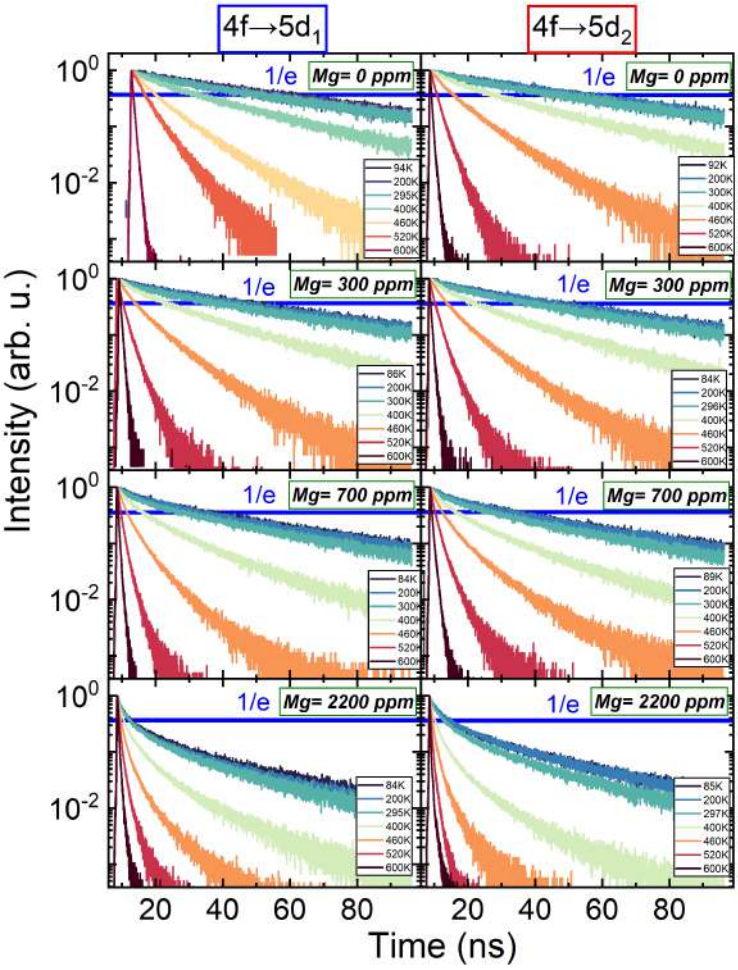

Figure 33. Temperature-dependent decay of normalized PL of LuGAGG:Ce, Mg samples at excitation to Ce^{3+} $5d_1$ and $5d_2$ levels.

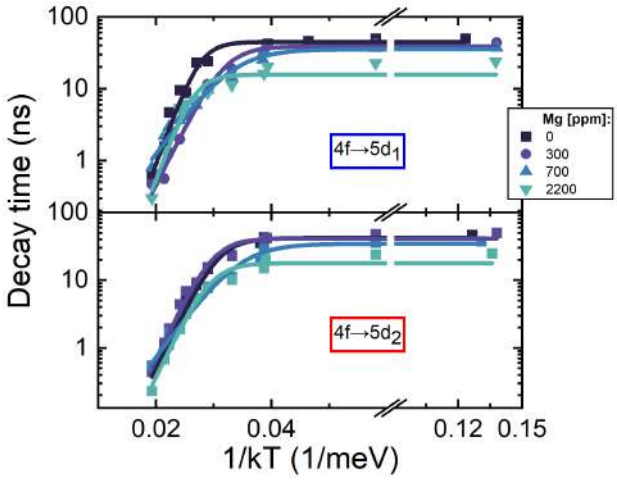

Figure 34. Temperature dependences of PL decay of LuGAGG:Ce, Mg samples at excitation to Ce^{3+} $5d_1$ and $5d_2$ levels.

In Table 6, all activation energy values are summarized for two different excitation conditions, estimated from both the PL intensity and the lifetime (1/e). Below the table, in Figure 35, the activation energy is presented as a function of magnesium content. In the graph, the green region indicates the general trend. Initially, the activation energy decreases slightly with the introduction of magnesium up to 300 ppm; however, with further magnesium incorporation, a more pronounced decline is observed. Some uncertainty in the Mg-content values should be considered, as the Mg concentration was directly measured for one sample and estimated for the others using the segregation coefficient; nevertheless, the observed activation-energy trend remains well defined.

Table 6. Activation energies E_a (meV) from PL intensity and $1/e$ analyses of LuGAGG:Ce, Mg samples with different magnesium content at excitation to Ce^{3+} $5d_1$ and $5d_2$ levels.

Sample (Mg content), ppm	**Excitation to $5d_1$ state**		**Excitation to $5d_2$ state**	
	E_a *from* **PL** (meV)	E_a *from* $1/e$ (meV)	E_a *from* **PL** (meV)	E_a *from* $1/e$ (meV)
0	516 ± 41	486 ± 42	563 ± 27	462 ± 18
300	464 ± 37	423 ± 14	498 ± 17	407 ± 15
700	388 ± 21	348 ± 15	402 ± 22	316 ± 12
2200	278 ± 15	261 ± 5	273 ± 16	223 ± 8

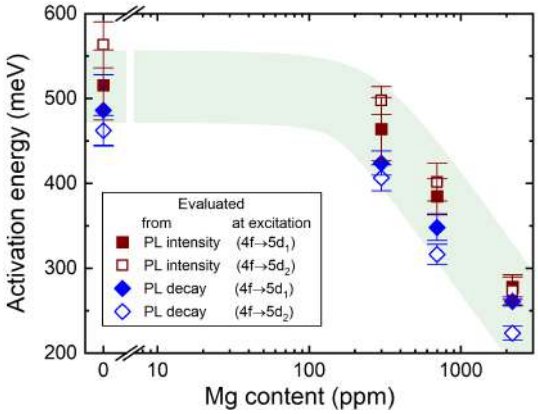

Figure 35. Activation energy dependence for PL intensity quenching and shortening of decay time at excitation to Ce^{3+} $5d_1$ and $5d_2$ states in LuGAGG:Ce, Mg samples. The green field depicts the tendency.

As discussed earlier, previous studies [18], [175] have attributed the improved timing characteristics of such scintillators to the stabilization of Ce^{4+} ions. In this work, however, we tend to interpret the results based on the presence of two emission centres: the classical Ce^{3+} centre and a modified centre consisting of Ce^{3+} ions located in close proximity to Mg^{2+} ions, forming a Ce^{3+}+Mg^{2+} centre. Mg^{2+} ions predominantly occupy octahedral sites, although a fraction of them can also be located in dodecahedral sites [181]. Since Ce^{3+} ions are also situated in the dodecahedral sites, they may be surrounded by up to ten possible magnesium positions at distances of 3.05 Å, 3.41 Å, and 3.74 Å. These

distances are sufficiently short to consider the formation of a Ce^{3+}+Mg^{2+} emission centre.

In the previous chapter, the temperature dependence of the PL decay curves was briefly analysed. In Figure 36, the temperature dependence of the PL decay time for the magnesium-free LuGAGG sample under excitation to the $5d_1$ state is presented. The decay curves measured at different temperatures are well described by a single-exponential function. This behaviour indicates that the luminescence in the magnesium-free sample is dominated by a single radiative recombination channel. The temperature dependence of the extracted decay time τ_1, shown in the right panel of Figure 36, is well defined by the Arrhenius expression (5.1). The activation energy is determined to be 0.48 eV, while the radiative decay time reaches approximately 50 ns.

A slightly different situation is observed for the LuGAGG samples doped with magnesium. In order to describe the temperature dependence of their PL kinetics, the involvement of a second emission centre, Ce^{3+}+Mg^{2+}, must be considered. Below, the equation describing the time dependence of the PL intensity *I(t)* is presented. This expression will be used to fit the PL decay kinetics of the LuGAGG samples containing magnesium:

$$I(t) \propto w_1 \cdot \exp\left(-\frac{t}{\tau_1}\right) + (1 - w_1) \cdot \exp\left(-\frac{t}{\tau_2}\right) \tag{6.3}$$

where w_1 is the weight coefficient that defines the involvement of the Ce^{3+} centre;

τ_1 represents decay times of the regular Ce^{3+} emission centre, extracted by fitting measured PL kinetics in samples with Mg content 300 and 700 ppm using (6.3);

τ_2 represents decay times of the modified Ce^{3+}+Mg^{2+} emission centre, also extracted by fitting measured PL kinetics using (6.3).

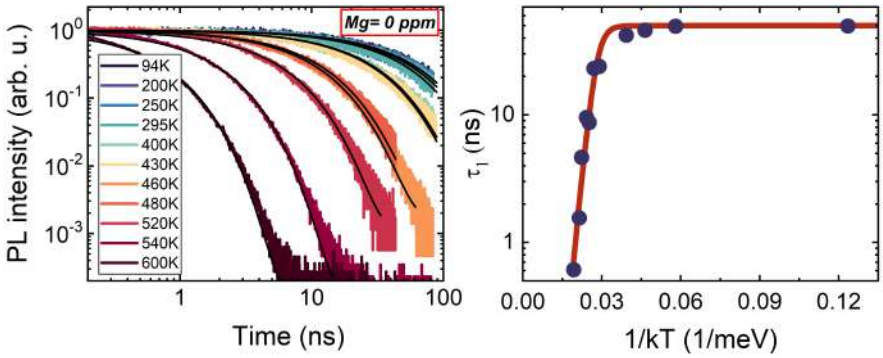

Figure 36. Temperature-dependent decay of normalized PL of Mg-free Lu-GAGG:Ce, Mg sample under excitation to Ce^{3+} $5d_1$ level. The decay curves are fitted using a single-exponential function. The right panel presents the temperature dependence of the extracted decay time τ_1, which is fitted with the Arrhenius expression (5.1).

The decay times τ_1 and τ_2 were extracted by fitting the measured PL kinetics using (6.3). Their temperature dependences were subsequently fitted using the Arrhenius-type expression (5.1) as shown in Figure 37. At low temperatures, the value of τ_2 is 10.6 ns, while τ_1 is 50 ns, which is substantially longer than τ_2. The value of τ_1 in the low-temperature range is 50 ns and represents the Ce^{3+} centre $5d_1 \rightarrow 4f$ radiative recombination. In contrast, the Ce^{3+}+Mg^{2+} emission centre corresponds to a faster recombination with a decay time of 10.6 ns, even at low temperatures where thermal ionization processes can be neglected. This indicates that a new recombination pathway appears in the Ce^{3+}+Mg^{2+} centres. Both decay rates (a combination of radiative recombination and temperature-independent nonradiative recombination (TINR)) do not depend on the magnesium concentration. They can be expressed as follows:

$$\tau_1 = \left(\frac{1}{\tau_{\mathrm{rad}}} + \frac{1}{\tau_{\mathrm{q1}}}\right)^{-1} = \frac{\tau_{\mathrm{rad}}}{1 + c_1 \cdot \exp\left(-\frac{E_{\mathrm{a1}}}{kT}\right)} \tag{6.4}$$

and

$$\tau_2 = \left(\frac{1}{\tau_{\text{rad}}} + \frac{1}{\tau_{\text{q2}}} + \frac{1}{\tau_{\text{TINR}}}\right)^{-1} = \frac{\left(\frac{1}{\tau_{\text{rad}}} + \frac{1}{\tau_{\text{TINR}}}\right)^{-1}}{1 + c_2 \cdot \exp\left(-\frac{E_{a2}}{kT}\right)} \tag{6.5}$$

τ_{q1} and τ_{q2} represent decay time constants for thermal quenching at Ce^{3+} and Ce^{3+}+Mg^{2+} centres;

τ_{TINR} represents decay time of temperature-independent nonradiative recombination.

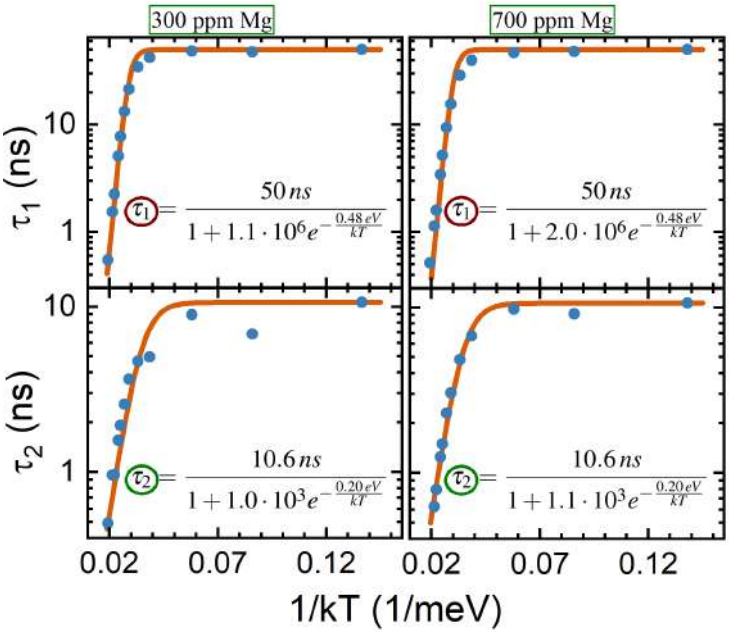

Figure 37. Temperature dependence of the emission decay times τ_1 and τ_2 for LuGAGG:Ce, Mg samples containing 300 and 700 ppm of Mg. The decay times were extracted from measured PL kinetics using (6.3). The lines correspond to Arrhenius-type fits, and the fitting parameters are indicated in the insets.

From Figure 37, the estimated activation energy for thermal quenching differs for the two emission centres. For the Ce^{3+} centre, the activation energy is 0.48 eV, whereas for the Ce^{3+}+Mg^{2+} centre it is 0.20 eV. Referring again to Table 6, the effective activation energy estimated by different methods also decreases with further magnesium incorporation, which can be explained by the increasing number of Ce^{3+}+Mg^{2+} emission centres. In addition, the weight

coefficient w_1 from (6.3) also depends on the magnesium content in the sample. Its dependence is presented in the graph shown in Figure 38, together with the parameters extracted for the Ce^{3+} and Ce^{3+}+Mg^{2+} centres.

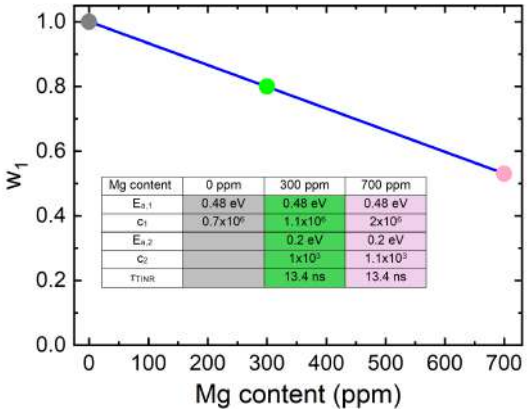

Figure 38. Dependence of the weight coefficient w_1 of the Ce^{3+} luminescence decay component on Mg content, as defined in the (6.3). The table presents parameters extracted for centres Ce^{3+} and Ce^{3+}+Mg^{2+}, including the activation energies E_{a1} and E_{a2}, frequency factors c_1 and c_2, temperature-independent nonradiative decay time τ_{TINR}, for samples with different Mg content. Different colors indicate the corresponding LuGAGG:Ce, Mg samples.

The two defined emission centres can be represented in the energy level scheme of the LuGAGG sample for interpretation (see Figure 39). In this scheme, both emission centres are illustrated together with their radiative and nonradiative recombination pathways. First, in the Ce^{3+} emission centre, a charge carrier is excited to one of the excited states, $5d_1$ or $5d_2$. From this excited state, the carrier can either decay radiatively to the ground state or be thermally ionized to the CB as the temperature increases. For the Ce^{3+}+Mg^{2+} emission centre, the situation differs because nonradiative recombination processes become more pronounced. In this case, a barrier-free channel for TINR is present, and the activation energy is reduced to only about 200 meV, making thermal quenching significantly easier compared to the Ce^{3+} centre.

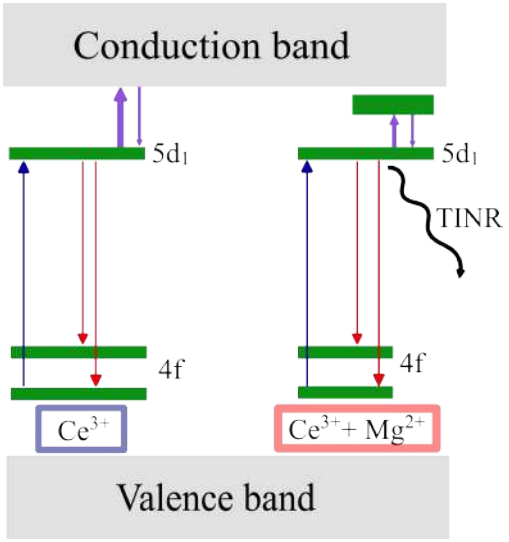

Figure 39. Energy scheme of Ce^{3+} and Ce^{3+}+Mg^{2+} centres in LuGAGG:Ce, Mg samples. Blue arrows indicate optical excitation, violet arrows represent thermal activation, red arrows correspond to radiative recombination, and the black arrow denotes the TINR.

In the PL measurements, excitation occurs via resonant photoexcitation of Ce^{3+} centres, whereas in the CL method, it is achieved using high-energy electrons. During CL measurements, nonequilibrium electron–hole pairs are generated throughout the lattice and migrate toward the Ce^{3+} emission centres, while a fraction of them recombine nonradiatively. In Figure 40, the results of the PL and CL intensities obtained using the two different experimental methods are presented. The PL intensity (corr.) values represent the emission intensity corrected for the number of absorbed photons, as determined from the measured absorbance spectra.

Conducting PL measurements to resonantly excite a charge carrier (electron) is only possible when an electron is present in the ground state of the Ce^{3+} emission centre; otherwise, excitation cannot occur. In contrast, during CL measurements, the entire host matrix is excited, making it possible to transfer a charge carrier from the host crystal lattice to the emission centre. Based on the results shown in the graph, both the PL and CL measured data points exhibit a similar trend: a significant decrease in intensity is observed in samples with magnesium content above few hundred ppm. However, no major differences in intensity between the two excitation methods are detected. The accelerated luminescence decay in LuGAGG samples with heavy magnesium codoping is

often explained by the stabilization of the Ce^{4+} emission centre. In the Ce^{4+} state, no electron is present in the ground state, which would prevent any PL emission under resonant excitation. In contrast, CL excitation could still activate the Ce^{4+} emission centre by supplying a nonequilibrium charge carrier from the lattice matrix. If this mechanism were dominant, clear differences between PL and CL results would be seen in Figure 40. However, the present results provide no evidence of emission enhancement by Ce^{4+}. The observed reduction in both PL and CL intensities is mainly attributed to nonradiative recombination processes at the emission centres. Meanwhile, typical CL-related excitation losses, caused by nonradiative recombination during the transport of charge carriers to the Ce^{3+} emission centres, appear to be negligible.
Codoping LuGAGG samples with magnesium leads to an accelerated emission decay; however, this improvement is achieved at the cost of reduced quantum efficiency.

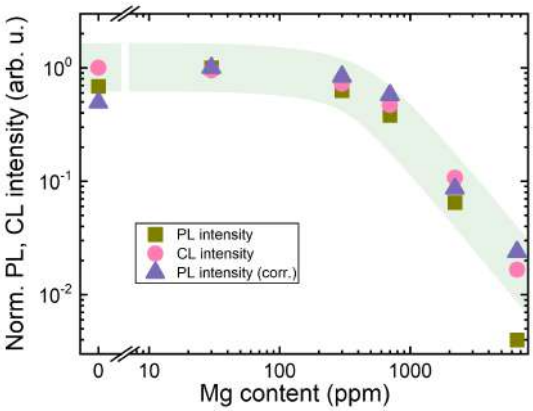

Figure 40. Normalized luminescence intensity of LuGAGG:Ce, Mg samples as a function of Mg content. CL under e-beam excitation is shown by pink circles, while PL under resonant excitation to the emitting Ce^{3+} $5d_1$ level is shown without correction (green squares) and with correction for the number of absorbed photons (violet triangles). The green shaded region indicates the observed trend.

6.3. Summary and highlights

Highlights:

- Heavy codoping with magnesium has no effect on the emission spectrum position and energy level positions of the excited states.
- Heavy magnesium codoping modifies the recombination dynamics by introducing a TINR channel and lowering the energy barrier for the thermal quenching process.
- Increasing magnesium content decreases the activation energy for thermal quenching.

Key findings:

- Heavy magnesium codoping in LuGAGG:Ce creates modified emission centres Ce^{3+}+Mg^{2+} that accelerate luminescence decay by introducing an additional temperature-independent nonradiative recombination channel and by enhancing thermal quenching over a barrier of 0.2 eV, substantially lower than that of regular Ce^{3+} centres.
- Efficiency losses in Mg codoped LuGAGG:Ce originate mainly from nonradiative recombination at Ce related emitting centres rather than from excitation transfer losses.

Excitation-relaxation processes in $(Lu_xY_{1-x})_3Al_5O_{12}$:Ce silica-based composites

YAG:Ce scintillators are essential for white LED manufacturing. However, in other fields, such as HEP experiments or medical imaging, a fast scintillation response and high stopping power for detecting high-energy particles enabled by high material density become critical. Garnet-type materials are highly flexible in terms of incorporating new ions with different ionic radii into the lattice structure. Although garnet materials exhibit considerable compositional flexibility, the realisation of the desired compositions in high-quality remains a technological challenge. Crystal growth using conventional methods such as CZ or BS requires high temperatures, which can result in the formation of shallow electron traps. In addition, expensive iridium crucibles are required during the growth process. These methods are not the most growth-efficient, especially considering that both medical imaging and particle physics experiments require thousands of crystals of consistent quality.

Currently, alternative synthesis or crystal growth techniques are being explored to replace traditional and expensive methods. As discussed in the previous chapter, LuGAGG samples were synthesised using the LPE method, which can be considered one of the alternative approaches. Another strategy is the incorporation of Ce-doped microcrystalline garnets into a glass matrix. The glass industry can provide a cost-effective alternative for cerium-doped composites due to the ability to scale the production to a large number of samples. Previous studies have already been conducted on cerium-doped Ba–Gd silica glass [182] and SiO_2:Ce^{3+} glass [183], demonstrating promising results. However, achieving efficient excitation transfer to the Ce^{3+} emitting centres remains challenging.

In this chapter, a two-step sol–gel method is employed for scintillator synthesis. The resulting composite consists of microcrystalline garnet scintillators embedded in a silica matrix. This approach has several objectives: (1) to improve the excitation transfer process to the Ce^{3+} emission centres, (2) to minimise surface defects through the formation of a silica passivation layer, and (3) to develop a flexible and low-cost sol–gel synthesis method. Tangible results obtained using the sol–gel method for composite phosphor materials have already been reported in the literature [184].

In the literature review section, the fundamental principles of the sol–gel method were outlined; therefore, a more detailed description of the two-step sol–gel process is presented in Figure 41. These compounds were fabricated and provided by Vilnius University, at the Department of Inorganic Chemistry in the laboratory of Professor *Aivaras Kareiva*. The term “two-step sol–gel

method" indicates that the process consists of two separate sol–gel cycles. In the first cycle (in Figure 41, marked with green squares), the precursors Y_2O_3 and/or Lu_2O_3 were dissolved in hot concentrated nitric acid. After the acid evaporated, the residual gel was washed several times with ≈200 mL of distilled water. Once the initially added distilled water had evaporated, an additional 50 mL of distilled water was introduced. Subsequently, three precursors ($Al(NO_3)_3 \cdot 9H_2O$, $(NH_4)_2Ce(NO_3)_6$, and H_3BO_3) were dissolved in the solution in order to obtain a nominal Ce concentration of 0.5%. The solution was stirred for 2 hours at 50 °C. Afterwards, citric acid was added and the solution was left stirring for more than 10 hours. At the same temperature of 50 °C, the solution was allowed to evaporate. The formed gel was dried for 24 hours at 140 °C. The obtained xerogel was then heated at 600 °C for 2 hours. Afterwards, it was ground in a mortar and calcined at 1000 °C for 4 hours in air. Finally, the powder was ground again in a mortar and annealed at 1200 °C for 4 hours. This procedure was performed in order to obtain a crack-free material. In the second step of the sol–gel procedure (in Figure 41, marked with brown squares), a hydrolysis reaction occurs between the silicon organic precursor (TEOS) and deionised water, with the addition of a small amount of nitric acid and a specific quantity of scintillator powder. The mixture was stirred for 1 hour at room temperature to achieve a homogeneous solution. Subsequently, the solution was placed in a drying container inside an ultrasonic bath to prevent air bubble formation, which can promote crack formation. Subsequently, the solution was dried at 70 °C for 168 hours [185]. The obtained xerogels of YAG:Ce/SiO_2, LuYAG:Ce/SiO_2, and LuAG:Ce/SiO_2 were placed in a quartz tube furnace and annealed in a helium atmosphere at 1000 °C for 2 hours. In the final stage, translucent YAG:Ce/SiO_2, LuYAG:Ce/SiO_2, and LuAG:Ce/SiO_2 composites were obtained.

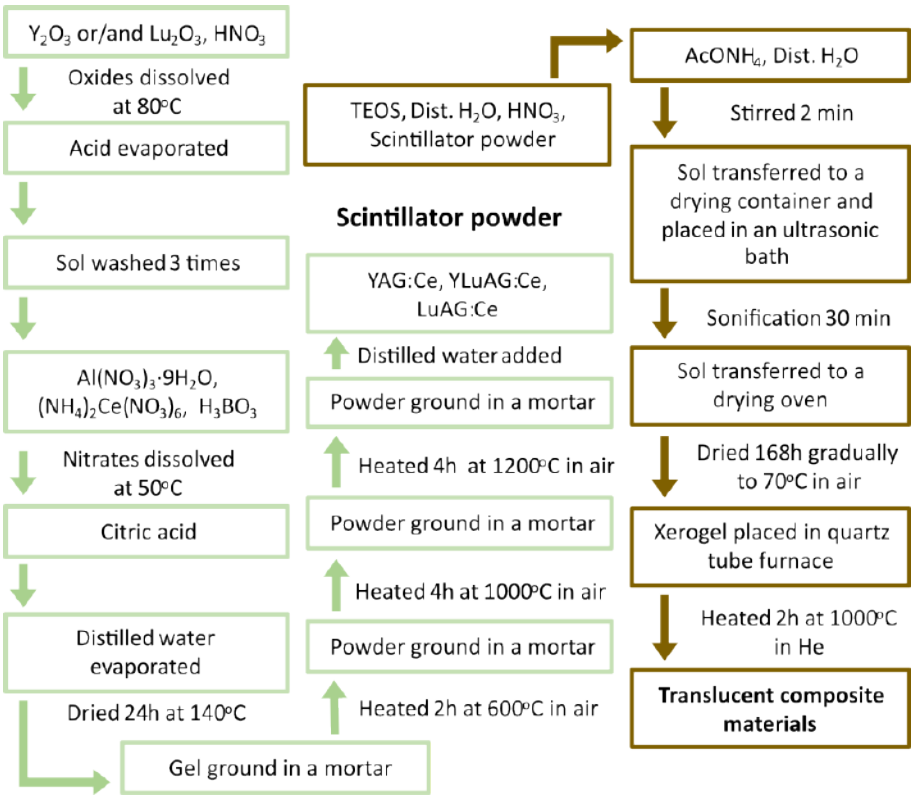

Figure 41. A scheme of a two-step sol–gel method synthesis process used to incorporate Ce-doped garnets into a silica matrix.

7.1. Samples

In this work, three related scintillator sets were investigated. The first set, yttrium aluminum garnet (YAG:Ce), was used as a reference sample. In the second set, yttrium was partially substituted with lutetium (LuYAG), while in the third set yttrium was fully replaced by lutetium, forming LuAG. Each of these sets consists of four samples with different incorporated garnet contents of 0.5 wt%, 1 wt%, 1.5 wt%, and 2 wt%.

Initially, the quality of the synthesised composites was examined using the X-ray diffraction (XRD) method. The results for all sample sets with 0.5 wt% garnet content are presented in Figure 42. A broad band can be identified in the 20–30° range, which corresponds to amorphous SiO_2. In addition, the composite XRD patterns were compared with the corresponding YAG and LuAG SC reference patterns from the ICDD Powder Diffraction File database. The com-

parison confirms that no additional crystalline phases are present apart from the single-phase garnet and amorphous silica. These results indicate that there is no observable contamination of the garnet microcrystals with silicon, which could potentially occur during the sol–gel fabrication procedure. In YAG, silicon can act as a tetravalent impurity (Si^{4+}) and promote the formation of the perovskite phase [186].

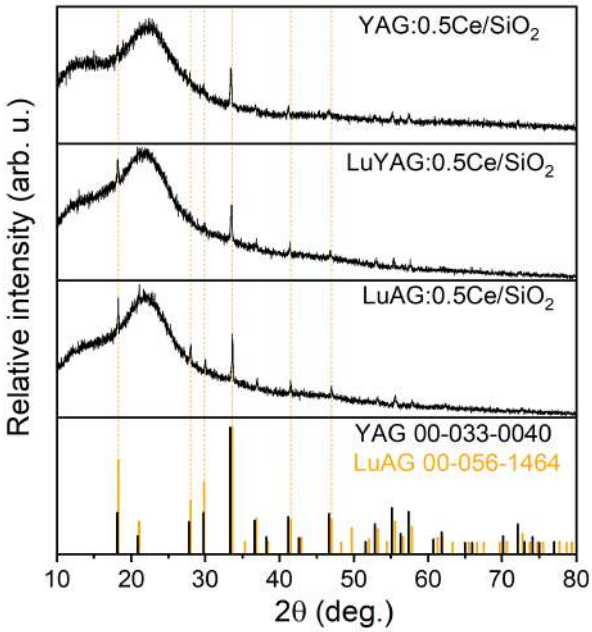

Figure 42. Comparison of XRD patterns of 0.5 wt% YAG:Ce, LuYAG:Ce and LuAG:Ce composites with a PDF data corresponding to SC phases.

7.2. Results

In Figure 43, SEM images together with CL intensity maps of several different areas are presented for the YAG:Ce/SiO_2 composite containing 2 wt% of garnets. These images demonstrate that the composite scintillators consist of submicrometer Ce-doped garnet grains embedded in a silica matrix. Some of these grains tend to agglomerate into larger clusters. The CL intensity map shows that agglomeration leads to higher CL intensity. Similar behaviour is observed in the other composite sets. SEM imaging, together with CL intensity mapping, is essential for interpreting the relationship between PL intensity and

QY as the garnet content increases, which will be discussed in the following sections.

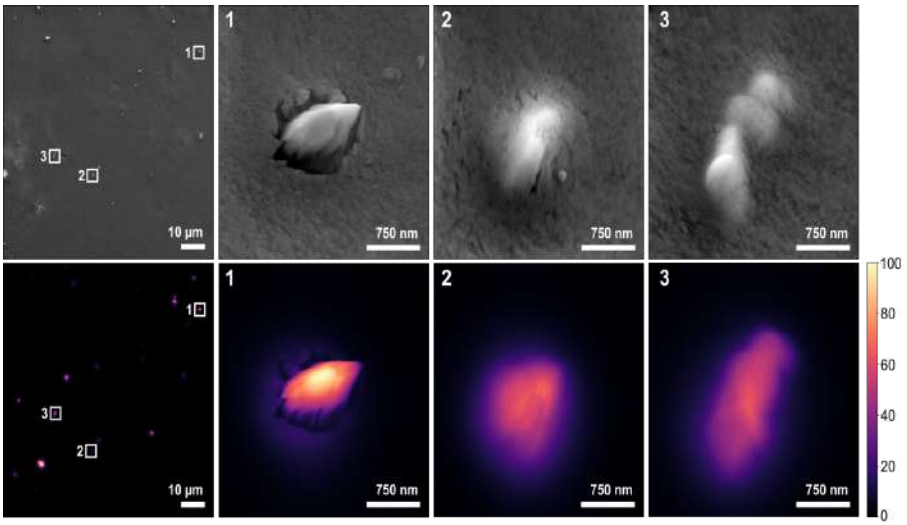

Figure 43. SEM images (upper row) and corresponding CL intensity maps (lower row) of the YAG:Ce/SiO_2 composite containing 2 wt% garnet. The numbered regions in the overview image are shown at higher magnification in panels 1–3.

In Figure 44, the normalised emission spectra of two composites, YAG/SiO_2 and LuAG/SiO_2, both containing 2 wt% of garnet, are presented under resonant excitation at 2.75 eV corresponding to the $5d_1$ state of Ce^{3+}. For comparison, the spectra of YAG:Ce SC and LuAG:Ce single-crystal films (SCF) are also included. No significant differences can be observed between the spectra of the composites and those of the SC or SCF samples. Due to the optical transition from the excited state to the two ground states, $F_{7/2}$ and $F_{5/2}$, the emission spectra consist of two overlapping bands. The LuAG/SiO_2 composite spectrum is shifted by approximately 25 nm relative to YAG/SiO_2, which is attributed to differences in the crystal field strength. However, the crystal field experienced by the Ce^{3+} ions within the microcrystals does not differ significantly from that in the bulk SC.

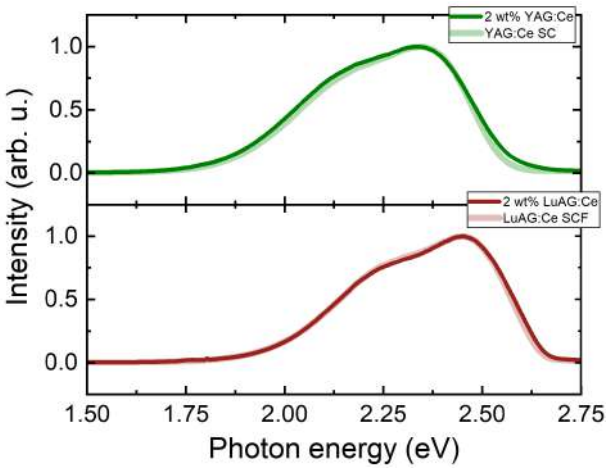

Figure 44. Normalized PL spectra of YAG:Ce/SiO_2 and LuAG:Ce/SiO_2 samples containing 2 wt% of garnet material. The spectra are compared with those of YAG:Ce SCs and LuAG:Ce SCF with excitation to the Ce^{3+} $5d_1$ state.

Initially, it might be assumed that no optical deviations from SCs are present. However, as shown in Figure 45, the contribution from SiO_2 is identified under excitation to the $5d_2$ state of Ce^{3+}. No significant differences are observed in the Ce^{3+} emission spectra when comparing excitation to the two Ce^{3+} excited states. An additional spectral band with a peak at approximately 2.99 eV was detected. The bandgap of SiO_2 is approximately 9 eV, whereas the present excitation energy is 3.58 eV, which is well below this value. Therefore, this emission band most likely originates from defect-related radiative centres in SiO_2. The two emission bands are well separated, and the silica-related emission can be suppressed, if necessary, through an optimised design of the scintillation detection setup. The SiO_2 emission band decays much faster than the Ce^{3+} emission band, as shown on the right in Figure 45. A single-exponential fit indicates that the Ce-related emission decays in approximately 60 ns, whereas the SiO_2 emission decays in about 14 ns.

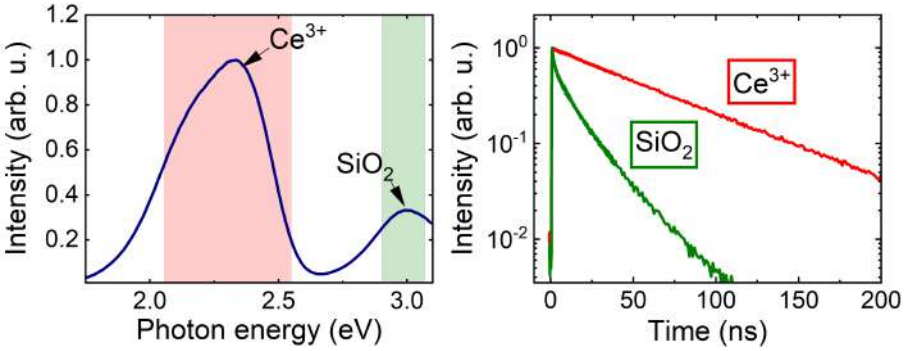

Figure 45. PL spectra of YAG:Ce/SiO_2 measured under the excitation to the Ce^{3+} $5d_2$ state. The right panel shows a comparison of the PL decay kinetics for emission bands attributed to Ce^{3+} and SiO_2.

In Figure 46, the dependence of PL intensity on the scintillator content is shown for all three sets of composite samples. Initially, at low scintillator concentrations, the PL intensity increases approximately linearly with increasing garnet content. However, with a further increase in wt%, the PL intensity begins to increase superlinearly. This behaviour is particularly evident in the LuYAG:Ce/SiO_2 composites. One possible explanation for this effect is improved light extraction caused by enhanced scattering of the luminescence light within the composite. Due to the refractive index contrast at the interface between the composite and the surrounding medium, part of the emitted light can be trapped within the material by total internal reflection. Light scattering changes the propagation direction of these photons, allowing a larger fraction of them to escape from the sample [187], [188]. In addition, increasing garnet content promotes the agglomeration of microcrystals into larger emitting structures. As discussed, the CL intensity of individual microcrystals normalized to their area increases with increasing microcrystal size, indicating that the emission is not simply proportional to the amount of scintillating material. This behaviour can be attributed to the increasing volume-to-surface ratio, which reduces the relative contribution of surface-related nonradiative recombination. Therefore, the formation of larger agglomerated structures may also contribute to the observed superlinear increase in PL intensity.

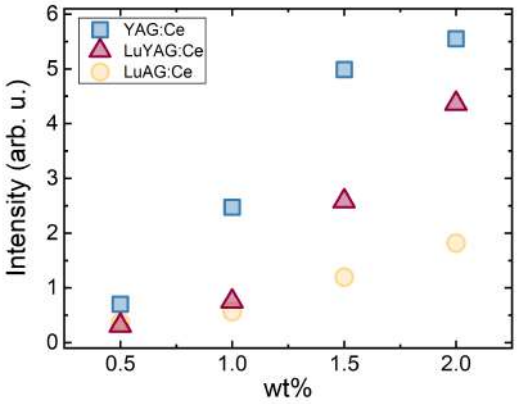

Figure 46. Comparison of PL intensity of YAG:Ce/SiO_2, LuYAG:Ce/SiO_2 and LuAG:Ce/SiO_2 composites as a function of garnet content wt% under excitation to the Ce^{3+} $5d_1$ state.

Together with the PL intensity, a clear trend was observed: increasing the wt% content leads to an increase in PL intensity. However, the behaviour of the QY differs slightly. In Figure 47, the dependence of QY on the wt% content for all three sets of scintillator composites is presented. The measurements were performed for all sample sets using excitation to the $5d_1$ excited state of the Ce^{3+} ion. Initially, with increasing wt% content, the QY value also tends to increase. This behaviour is most pronounced in the LuYAG:Ce/SiO_2 samples. The observed increase can be attributed to the previously discussed agglomeration process, assuming that the interface between grains within a cluster contains fewer nonradiative recombination centres than the interface between the grains and the surrounding silica matrix. Starting from approximately 1.5 wt% content, a saturation of the QY value is observed. The initial QY values differ among the three sample sets: for YAG:Ce/SiO_2 the value is approximately 30%, for LuYAG:Ce/SiO_2 below 10%, and for LuAG:Ce/SiO_2 ≈15%. At the highest wt% contents, the QY values for all samples vary only slightly, remaining in the closest range of approximately 40–50%. These values remain below the QY of the bulk YAG:Ce crystal (QY ≈ 80%), which is indicated by the blue dashed line in Figure 47. As the garnet wt% increases, the total PL intensity rises because a larger number of grains contribute to the emission, while QY indicates that the emission efficiency of individual grains remains limited.

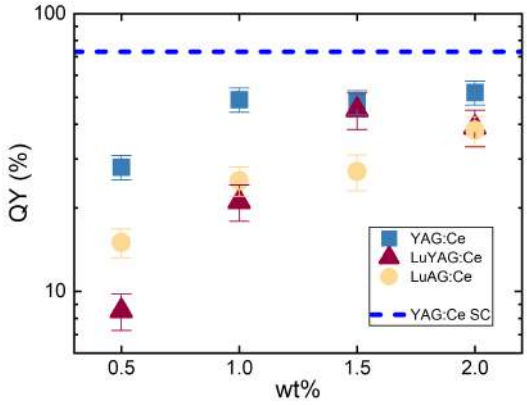

Figure 47. Comparison of QY of YAG:Ce/SiO_2, LuYAG:Ce/SiO_2 and LuAG:Ce/SiO_2 composites as a function of garnet content wt% under excitation to the Ce^{3+} $5d_1$ state. The dashed line indicates the QY value of the YAG:Ce SC.

In composite samples from all three sets, the PL decay occurs at approximately the same rate as in bulk crystals, i.e., around 60 ns. In Figure 48, normalised PL decay curves are presented for the LuYAG:Ce/SiO_2 sample with different wt% contents. The initial part of the decay in LuYAG:Ce/SiO_2 and LuAG:Ce/SiO_2 exhibits a fast component. As shown in the inset of Figure 48, this fast component is more pronounced in samples with lower garnet content, which can be attributed to enhanced nonradiative recombination. This observation correlates with the reduced internal quantum efficiency observed in these samples.

The decay kinetics were fitted using a biexponential function, with the slow component fixed at 60 ns for all samples. Table 7 presents the decay times of the fast components together with the corresponding weight coefficients for all components. A similar faster decay process was also observed in the previously described chapter on LuGAGG:Ce, Mg samples. In that case, the results were interpreted as the modification and formation of new Ce^{3+} emission centres associated with magnesium ions in close proximity. Likewise, the introduction of lutetium may initiate the formation of modified Ce^{3+} emission centres with enhanced nonradiative recombination. This process decreases the population of the emitting $5d_1$ level in Ce^{3+} and increases the decay rate.

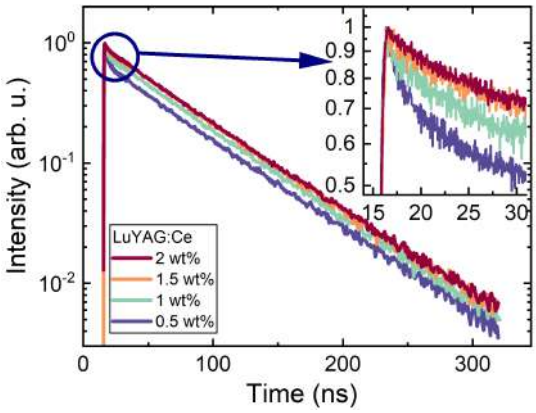

Figure 48. PL decay kinetics of LuYAG:Ce/SiO_2 samples with different garnet content wt% measured under excitation to the Ce^{3+} $5d_1$ state. The inset presents an enlarged view of the initial decay region.

Table 7. Decay times obtained from biexponential fits of PL and CL kinetics of YAG:Ce/SiO_2, LuYAG:Ce/SiO_2 and LuAG:Ce/SiO_2 composites containing 2 wt% garnet content.

	Decay time (ns)			
	PL		**CL**	
	Fast	**Slow**	**Fast**	**Slow**
YAG:Ce	–	60 (100%)	–	85 (100%)
LuYAG:Ce	37 (12%)	60 (88%)	25 (55%)	85 (45%)
LuAG:Ce	37 (32%)	60 (68%)	25 (58%)	85 (42%)

In Figure 49, CL spectra collected in a broad 1.5–4 eV spectral range from several microcrystals are presented. The spectra do not show any significant differences, indicating that neither the shape nor the size of the microcrystals has a noticeable impact on the emission spectra. When comparing the main Ce^{3+} emission band observed in CL and PL measurements, the band peaks remain at the same spectral position and exhibit similar shapes. The spectral positions of SiO_2-related bands correspond to those previously reported for CL spectra of SiO_2 layers of varying thickness deposited on silicon [189].

In PL measurements, one additional band associated with defect-related radiative centres in SiO_2 was observed. In contrast, the CL measurements

reveal two additional well-separated bands. These bands originate from SiO_2 emission (similar to the PL measurements shown in Figure 45) and are also detected in CL spectra collected from regions that do not contain garnet microcrystals.

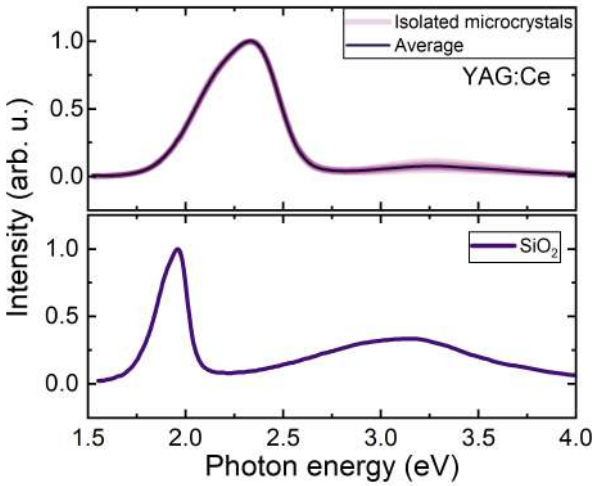

Figure 49. CL spectra collected from nine selected microcrystals in the YAG:Ce/SiO_2 composite (top panel). The bottom panel shows CL spectra recorded from composite regions that do not contain garnet microcrystals.

In YAG:Ce/SiO_2 samples, the Ce^{3+} decay time reaches approximately 85 ns in CL measurements in Figure 50. For the other two sample sets, LuYAG:Ce/SiO_2 and LuAG:Ce/SiO_2, a similar decay rate is observed for the longer decay component. However, these two samples also exhibit an additional faster decay component. A similar behaviour has been reported in the previously studied LuGAGG:Ce,Mg samples, where the fast decay component was attributed to the formation of modified emission centres Ce^{3+}+Mg^{2+}. Analogously, in the present case, the introduction of lutetium is likely to promote the formation of modified Ce^{3+} emission centres with an enhanced rate of nonradiative recombination. This process reduces the population of the emitting $5d_1$ level in Ce^{3+} and increases the luminescence decay rate. The decay kinetics for these two samples were fitted using a biexponential function, with the slower component fixed at 85 ns. The fast component for both samples was estimated to be approximately 25 ns, as presented in Table 7.

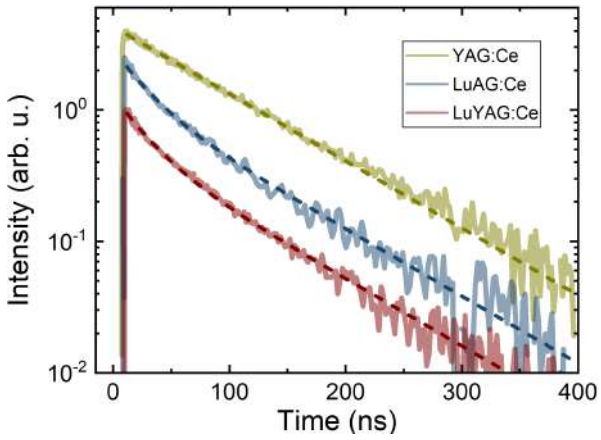

Figure 50. CL decays in YAG:Ce/SiO_2, LuAG:Ce/SiO_2, LuYAG:Ce/SiO_2 composites. Solid lines represent the measured decay kinetics, while dashed lines show the corresponding best-fit curves.

In Figure 51, the CL and PL decay kinetics for all three sample sets: YAG:Ce/SiO_2, LuYAG:Ce/SiO_2, and LuAG:Ce/SiO_2, are compared. For YAG:Ce/SiO_2, the emission intensity decays almost exponentially, although with different decay times: approximately 85 ns for CL and 60 ns for PL measurements. The longer decay observed under CL excitation is most probably associated with carrier trapping, which delays the excitation of the Ce^{3+} emission centres. A similar difference between PL and CL decay kinetics has been observed in GAGG:Ce, where it was attributed to delayed excitation transfer through the Gd ion subsystem [190]. In YAG:Ce, differences between the luminescence decays under optical and high-energy excitation have also been attributed to the trapping of migrating electrons before they recombine at the Ce^{3+} emission centres [191]. Therefore, carrier trapping during excitation transfer provides a possible explanation for the longer CL decay observed in the investigated YAG:Ce/SiO_2 composites. The faster decay components observed in the Lu-containing composites, as discussed above, are attributed to the formation of modified Ce^{3+} emission centres with an enhanced nonradiative recombination rate.

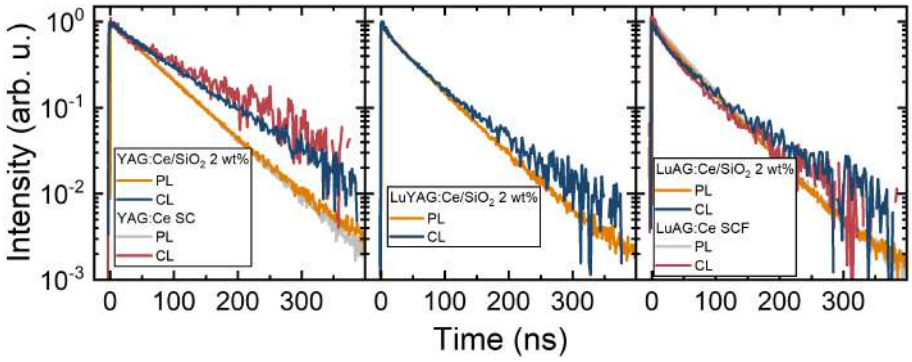

Figure 51. CL and PL kinetics of YAG:Ce/SiO_2, LuAG:Ce/SiO_2, LuYAG:Ce/SiO_2 composites with a 2 wt% of garnet content. The corresponding decay kinetics of the SCs and SCFs are included for comparison.

In Figure 52, the dependence of CL intensity on the individual grain size is presented for all three sample sets: YAG/SiO_2, LuAG/SiO_2, and LuYAG/SiO_2, each containing 2 wt% of garnet. A calculation method was implemented to evaluate the irregular grain sizes. The grain size was estimated by counting the number of pixels in the CL scan that emit with an intensity above a fixed threshold. For each grain, the luminescence intensities of all emitting pixels were summed and then normalised by the grain size. If the emission intensity were proportional only to the grain area, all data points in Figure 52 would yield the same value along the Y-axis. However, a clear increase in the surface-area-normalised intensity with increasing grain size is observed for all samples. This behaviour may be associated with the increase in the volume-to-surface ratio as the grain size becomes larger. Since grain surfaces typically contain non-radiative recombination centres, their relative influence decreases as the grain size increases, resulting in more efficient luminescence from larger grains.

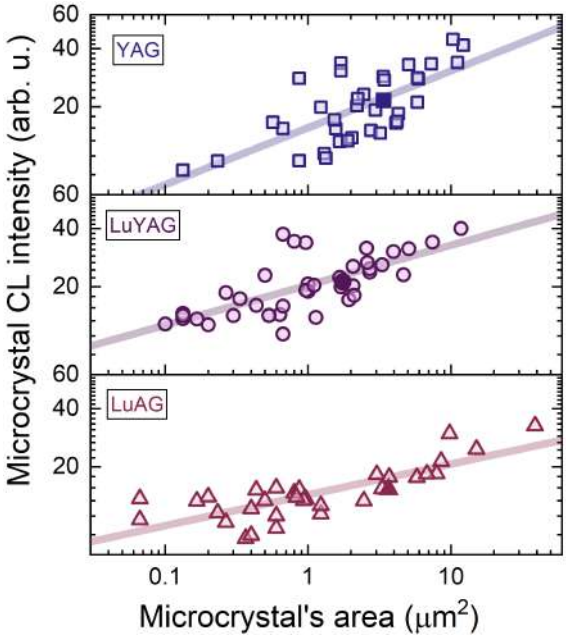

Figure 52. CL intensity of individual microcrystals as a function of their area in YAG:Ce/SiO_2, LuAG:Ce/SiO_2, LuYAG:Ce/SiO_2 composites containing 2 wt% garnet content. The intensity values are normalised to the microcrystal area. Solid points represent the mean values for microcrystals of similar size.

Various intrinsic and impurity-related defects are theoretically predicted to occur in YAG, some of which possess low activation energies and may act as trapping centres [186]. Thermoluminescence glow-curve analysis of YAG:Ce indicates that up to eleven shallow traps can be active in this material [191]. Therefore, the trapping centres in YAG:Ce are likely to have a complex origin. Theoretical calculations identify antisite defects Y_{Al} in YAG as the lowest-energy intrinsic defects [186]. A high concentration of such defects has been experimentally observed in YAG SCs grown at elevated temperatures (1800–1900 °C) [192]. In contrast, their density is significantly reduced in thin layers fabricated by the LPE at lower temperatures (850–1040 °C) [193], as well as in ceramics sintered at temperatures far below the melting point of YAG [194]. In the present samples, which were fabricated at moderate temperatures using the sol–gel method, the contribution of antisite defects as electron traps is therefore expected to be minimal.

7.3. Summary and highlights

Highlights:

- Structural analysis confirms that garnet microcrystals embedded in silica retain a single-crystal-like structure, while light emission spectral analysis reveals an additional defect-related emission originating from the silica matrix.
- Increasing garnet microcrystal content enhances the total PL intensity, whereas the QY rises initially and saturates at 1.5 wt%.
- Larger garnet grains exhibit enhanced surface-area-normalised luminescence intensity, attributed to the increased volume-to-surface ratio with increasing grain size.

Key findings:

- Low-cost composites consisting of YAG:Ce, LuYAG:Ce, or LuAG:Ce grains in silica matrix have potential for scalable production as scintillators exhibiting bulk-like Ce^{3+} emission spectra, luminescence decay, and quantum efficiency.

REFERENCES

[1] D. R. Schaart, "Physics and technology of time-of-flight pet detectors", *Physics in Medicine and Biology*, vol. 66, no. 9, 09TR01, Apr. 2021. doi: 10.1088/1361-6560/abee56

[2] R. Pelberg, "Basic principles in computed tomography (ct)", in *Cardiac CT Angiography Manual*. London: Springer London, 2015, pp. 19–58, isbn: 978-1-4471-6690-0. doi: 10.1007/978-1-4471-6690-0_2

[3] W. A. Kalender, "X-ray computed tomography", *Physics in Medicine & Biology*, vol. 51, no. 13, R29, Jun. 2006. doi: 10.1088/0031-9155/51/13/R03

[4] I. Béjar Alonso et al., Eds., *High-Luminosity Large Hadron Collider (HL-LHC): Technical Design Report* (CERN Yellow Reports: Monographs CERN-2020-010). Geneva: CERN, 2020, isbn: 978-92-9083-587-5. doi: 10.23731/CYRM-2020-0010

[5] A. Jana et al., "Perovskite scintillators, direct detectors, and x-ray imagers", *Materials Today*, vol. 55, pp. 110–136, 2022. doi: 10.1016/j.mattod.2022.04.009

[6] G. Blasse, "Scintillator materials", *Chemistry of Materials*, vol. 6, no. 9, pp. 1465–1475, 1994. doi: 10.1021/cm00045a002

[7] A. Markovskyi et al., "Structural, luminescence and photoconversion properties of lu3al5o12:ce single crystalline film phosphors for wled application", *Journal of Alloys and Compounds*, vol. 929, p. 167 159, 2022, issn: 0925-8388. doi: 10.1016/j.jallcom.2022.167159

[8] T. Yanagida et al., "Development of pr:luag scintillator array and assembly for positron emission mammography", *IEEE Transactions on Nuclear Science*, vol. 57, no. 3, pp. 1492–1495, 2010. doi: 10.1109/TNS.2009.2032265

[9] C. Michail et al., "Evaluation of the imaging performance of lso powder scintillator for use in x-ray mammography", *Nuclear Instruments and Methods in Physics Research Section A: Accelerators, Spectrometers, Detectors and Associated Equipment*, vol. 580, no. 1, pp. 558–561, 2007, Proceedings of the 10th International Symposium on Radiation Physics, issn: 0168-9002. doi: 10.1016/j.nima.2007.05.234

[10] T. Yanagida, T. Kato, D. Nakauchi, and N. Kawaguchi, “Fundamental aspects, recent progress and future prospects of inorganic scintillators”, *Japanese Journal of Applied Physics*, vol. 62, no. 1, p. 010 508, 2023. doi: 10.35848/1347-4065/ac9026

[11] C. Dujardin et al., “Needs, trends, and advances in inorganic scintillators”, *IEEE Transactions on Nuclear Science*, vol. 65, no. 8, pp. 1977–1997, 2018. doi: 10.1109/TNS.2018.2840160

[12] D. Zhu, M. Nikl, W. Chewpraditkul, and J. Li, “Development and prospects of garnet ceramic scintillators: A review”, *Journal of Advanced Ceramics*, vol. 11, no. 12, pp. 1825–1848, 2022. doi: 10.1007/s40145-022-0660-9

[13] M. Nikl, “Scintillation detectors for x-rays”, *Measurement Science and Technology*, vol. 17, no. 4, R37, Feb. 2006. doi: 10.1088/0957-0233/17/4/R01

[14] G. Singh, V. Thomas, V. Tiwari, and A. Karnal, “Effect of cerium doping on optical and scintillation properties of transparent yag ceramic”, *Ceramics International*, vol. 43, no. 12, pp. 9032–9040, 2017, issn: 0272-8842. doi: 10.1016/j.ceramint.2017.04.047

[15] M. Fasoli et al., “Band-gap engineering for removing shallow traps in rare-earth $lu_3al_5o_{12}$ garnet scintillators using ga^{3+} doping”, *Phys. Rev. B*, vol. 84, p. 081 102, 8 Aug. 2011. doi: 10.1103/PhysRevB.84.081102

[16] O. Sidletskiy et al., “Structure and scintillation yield of ce–doped al–ga substituted yttrium garnet”, *Materials Research Bulletin*, vol. 47, no. 11, pp. 3249–3252, 2012, issn: 0025-5408. doi: 10.1016/j.materresbull.2012.08.004

[17] M. Nikl and A. Yoshikawa, “Recent r&d trends in inorganic single-crystal scintillator materials for radiation detection”, *Advanced Optical Materials*, vol. 3, no. 4, pp. 463–481, 2015. doi: 10.1002/adom.201400571

[18] S. Blahuta, A. Bessiere, B. Viana, P. Dorenbos, and V. Ouspenski, “Evidence and consequences of ce^{4+} in lyso:ce,ca and lyso:ce,mg single crystals for medical imaging applications”, *IEEE Transactions on Nuclear Science*, vol. 60, no. 4, pp. 3134–3141, 2013. doi: 10.1109/TNS.2013.2269700

[19] R.-Y. Zhu, "Progress on inorganic scintillators for future HEP experiments", in *Hard X-Ray, Gamma-Ray, and Neutron Detector Physics XXIII*, N. J. Cherepy, M. Fiederle, and R. B. James, Eds., International Society for Optics and Photonics, vol. 11838, SPIE, 2021, p. 118380I. doi: 10.1117/12.2596459

[20] R. Hodák, *A basic introduction to scintillating detectors*, Lecture slides, IEEE NPSS Prague EduCom International Summer School (PEISS), June 30 – July 11, 2025, Prague, Czech Republic, 2025.

[21] Analytical Components, *The history of scintillation*, https://analyticalcomponents.uk/the-history-of-scintillation/, Accessed: 2026-01-04.

[22] M. Koshimizu, "Recent progress of organic scintillators", *Japanese Journal of Applied Physics*, vol. 62, no. 1, p. 010 503, 2023. doi: 10.35848/1347-4065/ac94fe

[23] D. L. Horrocks, "The mechanisms of the liquid scintillation process", in *Liquid Scintillation*, A. Noujaim, C. Ediss, and L. Weibe, Eds., Academic Press, 1976, pp. 1–16, isbn: 978-0-12-522350-8. doi: 10.1016/B978-0-12-522350-8.50006-4

[24] M. Hamel, B. Sabot, C. Dutsov, G. H. Bertrand, and K. Mitev, "Tuning the decay time of liquid scintillators", *Journal of Luminescence*, vol. 235, p. 118 021, 2021, issn: 0022-2313. doi: 10.1016/j.jlumin.2021.118021

[25] M. Lerch, *Scintillation detectors*, Lecture slides, 4th ARDENT Workshop, Prague, Czech Republic, 2015.

[26] P. Schotanus, "Recent developments in the use of organic and inorganic scintillation materials in industrial applications", *Radiation Measurements*, vol. 194, p. 107 677, 2026, issn: 1350-4487. doi: 10.1016/j.radmeas.2026.107677

[27] T. YANAGIDA, "Inorganic scintillating materials and scintillation detectors", *Proceedings of the Japan Academy, Series B*, vol. 94, no. 2, pp. 75–97, 2018. doi: 10.2183/pjab.94.007

[28] R. C. Lanza, W. Rideout, F. Fahey, and R. E. Zimmerman, "Gas scintillators for imaging of low energy isotopes", *IEEE Transactions on Nuclear Science*, vol. 34, no. 1, pp. 406–409, Feb. 1987. doi: 10.1109/TNS.1987.4337372

[29] M. Mutterer, “Gas scintillation nuclear particle detectors”, *Nuclear Instruments and Methods in Physics Research*, vol. 196, no. 1, pp. 73–81, 1982, issn: 0167-5087. doi: 10.1016/0029-554X(82)90619-X

[30] P. Lecoq, “Scintillation detectors for charged particles and photons”, in *Particle Physics Reference Library: Volume 2: Detectors for Particles and Radiation*, C. W. Fabjan and H. Schopper, Eds. Cham: Springer International Publishing, 2020, pp. 45–89, isbn: 978-3-030-35318-6. doi: 10.1007/978-3-030-35318-6_3

[31] S. Min, H. Kang, B. Seo, J. Cheong, C. Roh, and S. Hong, “A review of nanomaterial based scintillators”, *Energies*, vol. 14, no. 22, 2021, issn: 1996-1073. doi: 10.3390/en14227701

[32] F. Maddalena et al., “Inorganic, organic, and perovskite halides with nanotechnology for high–light yield x- and γ-ray scintillators”, *Crystals*, vol. 9, no. 2, 2019, issn: 2073-4352. doi: 10.3390/cryst9020088

[33] J. Hubbell, “Electron–positron pair production by photons: A historical overview”, *Radiation Physics and Chemistry*, vol. 75, no. 6, pp. 614–623, 2006, Pair Production, issn: 0969-806X. doi: 10.1016/j.radphyschem.2005.10.008

[34] H. Cui et al., “Lead-free organic–inorganic hybrid scintillators for x-ray detection”, *Aggregate*, vol. 5, no. 2, e454, 2024. doi: 10.1002/agt2.454

[35] Stanford University, *What are scintillator materials?*, https://web.stanford.edu/group/scintillators/scintillators.html, Accessed: 2026-05-17.

[36] M. Nikl et al., “Defect engineering in ce-doped aluminum garnet single crystal scintillators”, *Crystal Growth & Design*, vol. 14, no. 9, pp. 4827–4833, 2014. doi: 10.1021/cg501005s

[37] M. Weber, S. Derenzo, and W. Moses, “Measurements of ultrafast scintillation rise times: Evidence of energy transfer mechanisms”, *Journal of Luminescence*, vol. 87–89, pp. 830–832, 2000, issn: 0022-2313. doi: 10.1016/S0022-2313(99)00430-5

[38] S. E. Derenzo, W.-S. Choong, and W. W. Moses, "Fundamental limits of scintillation detector timing precision", *Physics in Medicine & Biology*, vol. 59, no. 13, pp. 3261–3286, 2014. doi: 10.1088/0031-9155/59/13/3261

[39] Y.-C. Lin, M. Bettinelli, and M. Karlsson, "Unraveling the mechanisms of thermal quenching of luminescence in ce3+-doped garnet phosphors", *Chemistry of Materials*, vol. 31, no. 11, pp. 3851–3862, 2019. doi: 10.1021/acs.chemmater.8b05300

[40] M. R. Ashraf et al., "Dosimetry for flash radiotherapy: A review of tools and the role of radioluminescence and cherenkov emission", *Frontiers in Physics*, vol. 8, p. 328, 2020. doi: 10.3389/fphy.2020.00328

[41] A. N. Vasil'ev, "Microtheory of scintillation in crystalline materials", in *Engineering of Scintillation Materials and Radiation Technologies*, ser. Springer Proceedings in Physics, M. Korzhik and A. Gektin, Eds., vol. 200, Springer International Publishing, 2017. doi: 10.1007/978-3-319-68465-9_1

[42] A. Vasil'ev, "Relaxation of hot electronic excitations in scintillators: Account for scattering, track effects, complicated electronic structure", in *Proceedings of the Fifth International Conference on Inorganic Scintillators and their applications*, 2000, pp. 43–52.

[43] V. Shevelev, A. Ishchenko, A. Vanetsev, V. Nagirnyi, and S. Omelkov, "Ultrafast hybrid nanocomposite scintillators: A review", *Journal of Luminescence*, vol. 242, p. 118 534, 2022, issn: 0022-2313. doi: 10.1016/j.jlumin.2021.118534

[44] F. Gao, Y. Xie, S. Kerisit, L. Campbell, and W. Weber, "Yield, variance and spatial distribution of electron–hole pairs in csi", *Nuclear Instruments and Methods in Physics Research Section A: Accelerators, Spectrometers, Detectors and Associated Equipment*, vol. 652, no. 1, pp. 564–567, 2011, Symposium on Radiation Measurements and Applications (SORMA) XII 2010, issn: 0168-9002. doi: 10.1016/j.nima.2010.08.063

[45] R. Narayan, R. Miranda, and P. Rez, "Simulating gamma-ray energy resolution in scintillators due to electron–hole pair statistics", *Nuclear Instruments and Methods in Physics Research Section B: Beam Inter-*

actions with Materials and Atoms, vol. 269, no. 22, pp. 2667–2675, 2011, issn: 0168-583X. doi: 10.1016/j.nimb.2011.08.008

[46] P. Lecoq, A. Annenkov, A. Gektin, M. Korzhik, and C. Pedrini, *Inorganic Scintillators for Detector Systems: Physical Principles and Crystal Engineering* (Particle Acceleration and Detection). Berlin, Heidelberg: Springer, 2006, isbn: 978-3-540-27766-8.

[47] J. Ueda and S. Tanabe, "(invited) review of luminescent properties of ce3+-doped garnet phosphors: New insight into the effect of crystal and electronic structure", *Optical Materials: X*, vol. 1, p. 100 018, 2019, issn: 2590-1478. doi: 10.1016/j.omx.2019.100018

[48] J. Qiao, J. Zhao, Q. Liu, and Z. Xia, "Recent advances in solid-state led phosphors with thermally stable luminescence", *Journal of Rare Earths*, vol. 37, no. 6, pp. 565–572, 2019, issn: 1002-0721. doi: 10.1016/j.jre.2018.11.001

[49] Y. Du and H. Zaidi, "Single-photon emission computed tomography: Principles and applications", in *Encyclopedia of Biomedical Engineering*, vol. 3, Elsevier, 2019, pp. 493–506. doi: 10.1016/B978-0-12-801238-3.10891-8

[50] C. L. Melcher, "Scintillation crystals for pet", *The Journal of Nuclear Medicine*, vol. 41, no. 6, pp. 1051–1055, 2000.

[51] M. Conti, "State of the art and challenges of time-of-flight pet", *Physica Medica*, vol. 25, no. 1, pp. 1–11, 2009, issn: 1120-1797. doi: 10.1016/j.ejmp.2008.10.001

[52] E. Enlow and S. Abbaszadeh, "State-of-the-art challenges and emerging technologies in radiation detection for nuclear medicine imaging: A review", *Frontiers in Physics*, vol. 11, p. 1 106 546, 2023. doi: 10.3389/fphy.2023.1106546

[53] A. Nassalski et al., "Comparative study of scintillators for pet/ct detectors", in *IEEE Nuclear Science Symposium Conference Record, 2005*, vol. 5, 2005, pp. 2823–2829. doi: 10.1109/NSSMIC.2005.1596921

[54] X. Yu et al., "Requirements of scintillation crystals with the development of pet scanners", *Crystals*, vol. 12, no. 9, 2022, issn: 2073-4352. doi: 10.3390/cryst12091302

[55] C. Michail, P. Liaparinos, N. Kalyvas, I. Kandarakis, G. Fountos, and I. Valais, "Radiation detectors and sensors in medical imaging", *Sensors*, vol. 24, no. 19, p. 6251, 2024. doi: 10.3390/s24196251

[56] E. Berg and S. R. Cherry, "Innovations in instrumentation for positron emission tomography", *Seminars in Nuclear Medicine*, vol. 48, no. 4, pp. 311–331, 2018, Instrumentation, issn: 0001-2998. doi: 10.1053/j.semnuclmed.2018.02.006

[57] R. Vinke et al., "Optimizing the timing resolution of sipm sensors for use in tof-pet detectors", *Nuclear Instruments and Methods in Physics Research Section A: Accelerators, Spectrometers, Detectors and Associated Equipment*, vol. 610, no. 1, pp. 188–191, 2009, New Developments In Photodetection NDIP08, issn: 0168-9002. doi: 10.1016/j.nima.2009.05.068

[58] S. J. Duclos et al., "Development of the hilighttm scintillator for computed tomography medical imaging", *Nuclear Instruments and Methods in Physics Research Section A: Accelerators, Spectrometers, Detectors and Associated Equipment*, vol. 505, no. 1, pp. 68–71, 2003, Proceedings of the tenth Symposium on Radiation Measurements and Applications, issn: 0168-9002. doi: 10.1016/S0168-9002(03)01022-2

[59] B. C. Grabmaier and W. Rossner, "New scintillators for x-ray computed tomography", *Nuclear Tracks and Radiation Measurements*, vol. 21, no. 1, pp. 43–45, 1993, issn: 0735-245X.

[60] Z. Wang et al., "Needs, trends, and advances in scintillators for radiographic imaging and tomography", *IEEE Transactions on Nuclear Science*, vol. 70, no. 7, pp. 1244–1280, 2023. doi: 10.1109/TNS.2023.3290826

[61] O. D. I. Moseley, T. A. S. Doherty, R. Parmee, M. Anaya, and S. D. Stranks, "Halide perovskites scintillators: Unique promise and current limitations", *J. Mater. Chem. C*, vol. 9, no. 35, pp. 11 588–11 604, 2021. doi: 10.1039/D1TC01595H

[62] C. Ronda, "Scintillators for medical imaging", *Optical Materials: X*, vol. 22, p. 100 293, 2024, issn: 2590-1478. doi: 10.1016/j.omx.2024.100293

[63] L. Lu, M. Sun, T. Wu, Q. Lu, B. Chen, and B. Huang, "All-inorganic perovskite nanocrystals: Next-generation scintillation materials for high-resolution x-ray imaging", *Nanoscale Advances*, vol. 4, no. 3, pp. 680–696, Feb. 2022, issn: 2516-0230. doi: 10.1039/d1na00815c

[64] S. Gianfaldoni, R. Gianfaldoni, U. Wollina, J. Lotti, G. Tchernev, and T. Lotti, "An overview on radiotherapy: From its history to its current applications in dermatology", *Open Access Macedonian Journal of Medical Sciences*, vol. 5, no. 4, pp. 521–525, 2017. doi: 10.3889/oamjms.2017.122

[65] W. D. Newhauser and R. Zhang, "The physics of proton therapy", *Physics in Medicine & Biology*, vol. 60, no. 8, R155, Mar. 2015. doi: 10.1088/0031-9155/60/8/R155

[66] L. Archambault, J. C. Polf, L. Beaulieu, and S. Beddar, "Characterizing the response of miniature scintillation detectors when irradiated with proton beams", *Physics in Medicine & Biology*, vol. 53, no. 7, p. 1865, Mar. 2008. doi: 10.1088/0031-9155/53/7/004

[67] M. Reimold et al., "Time-of-flight spectroscopy for laser-driven proton beam monitoring", *Scientific Reports*, vol. 12, p. 21 488, 2022. doi: 10.1038/s41598-022-25120-6

[68] L. Kelleter et al., "A scintillator-based range telescope for particle therapy", *Physics in Medicine & Biology*, vol. 65, no. 16, p. 165 001, 2020. doi: 10.1088/1361-6560/ab9415

[69] D. H. Perkins, *Introduction to High Energy Physics*, 4th ed. Cambridge, UK: Cambridge University Press, 2000, isbn: 0-521-62196-8.

[70] CERN, *Our mission*, https://home.cern/about/who-we-are/our-mission, Accessed: 2026-01-12, 2025.

[71] L. Martinazzoli, N. Kratochwil, S. Gundacker, and E. Auffray, "Scintillation properties and timing performance of state-of-the-art gd3al2ga3o12 single crystals", *Nuclear Instruments and Methods in Physics Research Section A: Accelerators, Spectrometers, Detectors and Associated Equipment*, vol. 1000, p. 165 231, 2021, issn: 0168-9002. doi: 10.1016/j.nima.2021.165231

[72] F. Addesa et al., “Comparative characterization study of lyso:ce crystals for timing applications”, *Journal of Instrumentation*, vol. 17, no. 08, P08028, Aug. 2022. doi: 10.1088/1748-0221/17/08/P08028

[73] R. Gargiulo, “Quality control of lyso:ce crystals for the cms barrel mip timing detector”, *Nuclear Instruments and Methods in Physics Research Section A: Accelerators, Spectrometers, Detectors and Associated Equipment*, vol. 1066, p. 169 624, 2024, issn: 0168-9002. doi: 10.1016/j.nima.2024.169624

[74] CERN Experimental Physics Department, “Strategic r&d programme on technologies for future experiments: Annual report 2021”, CERN, Geneva, Switzerland, Tech. Rep. CERN-EP-RDET-2022-006, Apr. 2022.

[75] J. Glodo et al., “New developments in scintillators for security applications”, *Physics Procedia*, vol. 90, pp. 285–290, 2017, Conference on the Application of Accelerators in Research and Industry, CAARI 2016, 30 October – 4 November 2016, Ft. Worth, TX, USA, issn: 1875-3892. doi: 10.1016/j.phpro.2017.09.012

[76] T. J. Hajagos, C. Liu, N. J. Cherepy, and Q. Pei, “High-z sensitized plastic scintillators: A review”, *Advanced Materials*, vol. 30, no. 27, p. 1 706 956, 2018. doi: 10.1002/adma.201706956

[77] U. Shirwadkar et al., “Progress on metal-loaded plastic scintillators for nuclear security applications”, in *2017 IEEE Nuclear Science Symposium and Medical Imaging Conference (NSS/MIC)*, 2017, pp. 1–3. doi: 10.1109/NSSMIC.2017.8532604

[78] K. E. Nelson, T. B. Gosnell, and D. A. Knapp, “The effect of energy resolution on the extraction of information content from gamma-ray spectra”, *Nuclear Instruments and Methods in Physics Research Section A: Accelerators, Spectrometers, Detectors and Associated Equipment*, vol. 659, no. 1, pp. 207–214, 2011, issn: 0168-9002. doi: 10.1016/j.nima.2011.06.057

[79] S. Robinson, R. Runkle, and R. Newby, “A comparison of performance between organic scintillation crystals and moderated 3he-based detectors for fission neutron detection”, *Nuclear Instruments and Methods in Physics Research Section A: Accelerators, Spectrometers, Detectors*

and Associated Equipment, vol. 652, no. 1, pp. 404–407, 2011, Symposium on Radiation Measurements and Applications (SORMA) XII 2010, issn: 0168-9002. doi: 10.1016/j.nima.2010.08.008

[80] H. Al Hamrashdi, S. D. Monk, and D. Cheneler, "Passive gamma-ray and neutron imaging systems for national security and nuclear non-proliferation in controlled and uncontrolled detection areas: Review of past and current status", *Sensors*, vol. 19, no. 11, 2019, issn: 1424-8220. doi: 10.3390/s19112638

[81] B. An, Y. Deng, Z. Jin, and S. Sun, "Scintillators for neutron detection and imaging: Advances and prospects", *Advanced Functional Materials*, p. 2 422 522, 2024. doi: 10.1002/adfm.202422522

[82] K. Asghar, M. F. Ngulimi, S. Kim, B. K. Seo, G. H. Bertrand, and C. Roh, "State of the art challenges and prospects of advanced materials in radiation detection for nuclear energy: A review", *Progress in Materials Science*, vol. 158, p. 101 616, 2026, issn: 0079-6425. doi: 10.1016/j.pmatsci.2025.101616

[83] V. Ryzhikov et al., "Instruments and detectors on the base of scintillator crystals znse(te), cwo, csi(tl) for systems of security and customs inspection systems", *Nuclear Instruments and Methods in Physics Research Section A: Accelerators, Spectrometers, Detectors and Associated Equipment*, vol. 537, no. 1, pp. 424–430, 2005, Proceedings of the 7th International Conference on Inorganic Scintillators and their Use in Scientific and Industrial Applications, issn: 0168-9002. doi: 10.1016/j.nima.2004.08.056

[84] G. Tessitore, G. A. Mandl, S. L. Maurizio, M. Kaur, and J. A. Capobianco, "The role of lanthanide luminescence in advancing technology", *RSC Advances*, vol. 13, no. 26, pp. 17 787–17 811, Jun. 2023, issn: 2046-2069. doi: 10.1039/d3ra00991b

[85] S. Sinha, J. Kwong, W. G. J. Langeveld, and P. Ryge, "Characterization of zno, BaF_2 and $PbWO_4$ scintillator detectors for cargo inspection using transmitted x-ray spectroscopy", *IEEE Transactions on Nuclear Science*, vol. 60, no. 2, pp. 1016–1023, 2013. doi: 10.1109/TNS.2013.2241451

[86] Y. Tian, "Development of phosphors with high thermal stability and efficiency for phosphor-converted leds", *Journal of Solid State Lighting*, vol. 1, no. 1, p. 11, 2014. doi: 10.1186/s40539-014-0011-8

[87] P. C. Ricci, "Assessment of crystalline materials for solid state lighting applications: Beyond the rare earth elements", *Crystals*, vol. 10, no. 7, 2020, issn: 2073-4352. doi: 10.3390/cryst10070559

[88] R. Génois, S. Jobic, G. Ouvrard, F. Massuyeau, and R. Gautier, "The crucial impact of cerium reduction on photoluminescence", *Applied Materials Today*, vol. 20, p. 100 643, 2020, issn: 2352-9407. doi: 10.1016/j.apmt.2020.100643

[89] P. Gorrotxategi, M. Consonni, and A. Gasse, "Optical efficiency characterization of led phosphors using a double integrating sphere system", *Journal of Solid State Lighting*, vol. 2, no. 1, p. 1, 2015. doi: 10.1186/s40539-014-0020-7

[90] A. Nikitin, A. Fedorov, and M. Korjik, "Novel glass ceramic scintillator for detection of slow neutrons in well logging applications", *IEEE Transactions on Nuclear Science*, vol. 60, no. 2, pp. 1044–1048, 2013. doi: 10.1109/TNS.2013.2251748

[91] A. Bala, J. Brown, D. Jenkins, and P. Joshi, "Operation of scintillators and sipms at high temperatures and their application for borehole logging", *Nuclear Instruments and Methods in Physics Research Section A: Accelerators, Spectrometers, Detectors and Associated Equipment*, vol. 997, p. 165 161, 2021, issn: 0168-9002. doi: 10.1016/j.nima.2021.165161

[92] J. Ampe et al., "The calibration and environmental testing of the engineering module of glast csi calorimeter", *IEEE Transactions on Nuclear Science*, vol. 51, no. 5, pp. 2008–2011, 2004. doi: 10.1109/TNS.2004.835704

[93] Y. Eisen, L. Evans, R. Starr, and J. Trombka, "Cdwo4 scintillator as a compact gamma ray spectrometer for planetary lander missions", *Nuclear Instruments and Methods in Physics Research Section A: Accelerators, Spectrometers, Detectors and Associated Equipment*, vol. 490, no. 3, pp. 505–517, 2002, issn: 0168-9002. doi: 10.1016/S0168-9002(02)01089-6

[94] C. Kim et al., "A review of inorganic scintillation crystals for extreme environments", *Crystals*, vol. 11, no. 6, p. 669, 2021. doi: 10.3390/cryst11060669

[95] D. de Faoite et al., "Development of glass-ceramic scintillators for gamma-ray astronomy", *Journal of Physics: Conference Series*, vol. 620, p. 012 002, 2015. doi: 10.1088/1742-6596/620/1/012002

[96] P. F. Bloser et al., "A fast scintillator Compton telescope for medium-energy gamma-ray astronomy", in *Space Telescopes and Instrumentation 2010: Ultraviolet to Gamma Ray*, M. Arnaud, S. S. Murray, and T. Takahashi, Eds., International Society for Optics and Photonics, vol. 7732, SPIE, 2010, p. 773 222. doi: 10.1117/12.857545

[97] G. Müller and J. Friedrich, "Crystal growth, bulk: Methods", in *Encyclopedia of Condensed Matter Physics*, F. Bassani, G. L. Liedl, and P. Wyder, Eds., Oxford: Elsevier, 2005, pp. 262–274, isbn: 978-0-12-369401-0. doi: 10.1016/B0-12-369401-9/00416-2

[98] Y. Yokota, M. Yoshino, and T. Horiai, *Inorganic Scintillator and Crystal Growth Methods*. Weinheim, Germany: Wiley-VCH, 2025, isbn: 978-3-527-35208-1. doi: 10.1002/9783527842025

[99] J. J. Derby and F. M. Shuaeib, "Crystal growth, bulk: Theory and models", in *Reference Module in Materials Science and Materials Engineering*, Elsevier, 2016. doi: 10.1016/B978-0-12-803581-8.01011-0

[100] N. Ye, J.-Y. Wang, R. Boughton, and M.-C. Hong, "Chapter 20 - functional crystals", in *Modern Inorganic Synthetic Chemistry (Second Edition)*, R. Xu and Y. Xu, Eds., Second Edition, Amsterdam: Elsevier, 2017, pp. 575–611, isbn: 978-0-444-63591-4. doi: 10.1016/B978-0-444-63591-4.00020-3

[101] V. Shlegel et al., "Recent progress in oxide scintillation crystals development by low-thermal gradient czochralski technique for particle physics experiments", *Journal of Instrumentation*, vol. 12, no. 08, p. C08011, Aug. 2017. doi: 10.1088/1748-0221/12/08/C08011

[102] Z. Frukacz and D. Pawlak, "Garnets, growth of", in *Encyclopedia of Materials: Science and Technology*, K. J. Buschow et al., Eds., Oxford: Elsevier, 2001, pp. 3455–3463, isbn: 978-0-08-043152-9. doi: 10.1016/B0-08-043152-6/00616-1

[103] R. Hendawi and M. Di Sabatino, "Analyzing structure loss in czochralski silicon growth: Root causes investigation through surface exami-

nation", *Journal of Crystal Growth*, vol. 629, p. 127 564, 2024, issn: 0022-0248. doi: 10.1016/j.jcrysgro.2023.127564

[104] A. Yoshikawa, V. Chani, and M. Nikl, "Czochralski growth and properties of scintillating crystals", *Acta Physica Polonica A*, vol. 124, no. 2, pp. 250–264, 2013. doi: 10.12693/APhysPolA.124.250

[105] Y. Shoji et al., "Growth of (la,gd)2si2o7 crystals by the czochralski method and crucible-free pulling from cold container techniques for scintillator applications", *Journal of Crystal Growth*, vol. 649, p. 127 950, 2025, issn: 0022-0248. doi: 10.1016/j.jcrysgro.2024.127950

[106] H. Zhu et al., "Bridgman method for growing metal halide single crystals: A review", *Inorganics*, vol. 13, no. 2, 2025, issn: 2304-6740. doi: 10.3390/inorganics13020053

[107] J. Lund, F. Olschner, and A. Burger, "Chapter 11 - lead iodide crystals and detectors", in *Semiconductors and Semimetals*, ser. Semiconductors and Semimetals, T. Schlesinger and R. B. James, Eds., vol. 43, Elsevier, 1995, pp. 443–464. doi: 10.1016/S0080-8784(08)62750-7

[108] EdTech Books, *Single crystal growth technique*, https://edtechbooks.org/semiconductor_physics/single_crystal_growth_technique, Accessed: 2026-01-15, 2025.

[109] V. Kozlov et al., "Improvements and problems of bridgman–stockbarger method for fabrication of tlbr single crystal detectors", *Nuclear Instruments and Methods in Physics Research Section A: Accelerators, Spectrometers, Detectors and Associated Equipment*, vol. 607, no. 1, pp. 126–128, 2009, Radiation Imaging Detectors 2008, issn: 0168-9002. doi: 10.1016/j.nima.2009.03.126

[110] L. F. Schneemeyer, "Crystal growth", in *Encyclopedia of Physical Science and Technology (Third Edition)*, R. A. Meyers, Ed., Third Edition, New York: Academic Press, 2003, pp. 79–89, isbn: 978-0-12-227410-7. doi: 10.1016/B0-12-227410-5/00158-7

[111] R. Fornari, "3.01 - bulk crystal growth of semiconductors: An overview", in *Comprehensive Semiconductor Science and Technology*, P. Bhattacharya, R. Fornari, and H. Kamimura, Eds., Amsterdam: Elsevier, 2011, pp. 1–35, isbn: 978-0-444-53153-7. doi: 10.1016/B978-0-44-453153-7.00088-2

[112] C. Heyn, "Epitaxy (classical mbe)", in *Encyclopedia of Condensed Matter Physics (Second Edition)*, T. Chakraborty, Ed., Second Edition, Oxford: Academic Press, 2024, pp. 544–553, isbn: 978-0-323-91408-6. doi: 10.1016/B978-0-323-90800-9.00205-5

[113] M. Ohring, "Chapter 8 - epitaxy", in *Materials Science of Thin Films (Second Edition)*, M. Ohring, Ed., Second Edition, San Diego: Academic Press, 2002, pp. 417–494, isbn: 978-0-12-524975-1. doi: 10.1016/B978-012524975-1/50011-2

[114] D. Maryenko, "Epitaxy", in *Encyclopedia of Condensed Matter Physics (Second Edition)*, T. Chakraborty, Ed., Second Edition, Oxford: Academic Press, 2024, pp. 528–543, isbn: 978-0-323-91408-6. doi: 10.1016/B978-0-323-90800-9.00208-0

[115] Z. Li et al., "Review of thin-film resistor sensors: Exploring materials, classification, and preparation techniques", *Chemical Engineering Journal*, vol. 477, p. 147 029, 2023, issn: 1385-8947. doi: 10.1016/j.cej.2023.147029

[116] MIT News, *Explained: Chemical vapor deposition*, https://news.mit.edu/2015/explained-chemical-vapor-deposition-0619, Accessed: 2026-01-22, 2015.

[117] M. M. Alam, M. Imran, A. Abutaleb, M. E. Khan, and W. Ali, "4 - fabrication approaches of nanocomposites", in *Nanocomposites-Advanced Materials for Energy and Environmental Aspects*, ser. Woodhead Publishing Series in Composites Science and Engineering, M. E. Khan, J. Aslam, and C. Verma, Eds., Woodhead Publishing, 2023, pp. 67–85, isbn: 978-0-323-99704-1. doi: 10.1016/B978-0-323-99704-1.00020-5

[118] Kintek Furnace, *What are the main disadvantages of chemical vapor deposition (cvd)?*, https://kintekfurnace.com/faqs/what-are-the-main-disadvantages-of-chemical-vapor-deposition-cvd, Accessed: 2025-01-22, 2025.

[119] E. Kuphal, "Liquid phase epitaxy", *Applied Physics A*, vol. 52, pp. 380–409, 1991. doi: 10.1007/BF00323650

[120] F. Lévy, "Film growth and epitaxy: Methods", in *Encyclopedia of Condensed Matter Physics*, F. Bassani, G. L. Liedl, and P. Wyder, Eds.,

Oxford: Elsevier, 2005, pp. 210–222, isbn: 978-0-12-369401-0. doi: 10.1016/B0-12-369401-9/00418-6

[121] M. G. Mauk, "6 - liquid-phase epitaxy", in *Handbook of Crystal Growth (Second Edition)*, ser. Handbook of Crystal Growth, T. F. Kuech, Ed., Second Edition, Boston: North-Holland, 2015, pp. 225–316, isbn: 978-0-444-63304-0. doi: 10.1016/B978-0-444-63304-0.00006-8

[122] E. Bauser, L. Schmidt, K. S. Loechner, and E. Raabe, "Liquid phase epitaxy apparatus for multiple layers utilizing centrifugal forces", *Japanese Journal of Applied Physics*, vol. 16, no. S1, p. 457, Jan. 1977. doi: 10.7567/JJAPS.16S1.457

[123] M. Kučera and P. Průša, "Lpe-grown thin-film scintillators", in *Nanocomposite, Ceramic, and Thin Film Scintillators*, M. Nikl, Ed., Pan Stanford Publishing, 2017, isbn: 978-981-4745-22-2.

[124] R. Priya, R. Mariappan, A. Karthikeyan, E. Palani, E. Krishnamoorthy, and G. Gowrisankar, "Review on rare earth metals doped lapo4 for optoelectronic applications", *Solid State Communications*, vol. 339, p. 114 457, 2021, issn: 0038-1098. doi: 10.1016/j.ssc.2021.114457

[125] V. Shah, J. Bhaliya, G. M. Patel, M. Popaliya, A. Mishra, and P. R. Patel, "Chapter 10 - biodegradable polymer nanocomposites as electrode materials for electrochemical double-layer capacitors and hybrid supercapacitor applications", in *Biodegradable and Biocompatible Polymer Nanocomposites*, K. Deshmukh and M. Pandey, Eds., Elsevier, 2023, pp. 311–352, isbn: 978-0-323-91696-7. doi: 10.1016/B978-0-323-91696-7.00019-2

[126] J. M. Nedelec, "Sol-gel processing of nanostructured inorganic scintillating materials", *Journal of Nanomaterials*, vol. 2007, no. 1, p. 036 392, 2007. doi: 10.1155/2007/36392

[127] A. Garcia-Murillo, C. Le Luyer-Urlacher, C. Dujardin, C. Pedrini, and J. Mugnier, "Rare-earth actived sol-gel films for scintillator applications", *Journal of Sol-Gel Science and Technology*, vol. 26, pp. 957–960, 2003. doi: 10.1023/A:1020701111361

[128] Y. Sun, M. Koshimizu, S. Kishimoto, and K. Asai, "Synthesis and characterization of pr^{3+}-doped glass scintillators prepared by the sol–gel method", *Journal of Sol-Gel Science and Technology*, vol. 62, no. 3, pp. 313–318, 2012. doi: 10.1007/s10971-012-2726-6

[129] H.-J. Im, C. Willis, S. Saengkerdsub, R. Makote, M. D. Pawel, and S. Dai, "Scintillators for alpha and neutron radiations synthesized by room temperature sol–gel processing", *Journal of Sol-Gel Science and Technology*, vol. 32, pp. 117–123, 2004. doi: 10.1007/s10971-004-5775-7

[130] M. Koshimizu, "Sol–gel-doped glasses for scintillators", in *Handbook of Sol-Gel Science and Technology*, L. Klein, M. Aparicio, and A. Jitianu, Eds. Cham: Springer International Publishing, 2016, pp. 1–29, isbn: 978-3-319-19454-7. doi: 10.1007/978-3-319-19454-7_103-1

[131] G. J. Owens et al., "Sol–gel based materials for biomedical applications", *Progress in Materials Science*, vol. 77, pp. 1–79, 2016, issn: 0079-6425. doi: 10.1016/j.pmatsci.2015.12.001

[132] S. Taylor, "Coatings for corrosion protection: Inorganic", in *Encyclopedia of Materials: Science and Technology*, K. J. Buschow et al., Eds., Oxford: Elsevier, 2001, pp. 1263–1269, isbn: 978-0-08-043152-9. doi: 10.1016/B0-08-043152-6/00238-2

[133] D. Navas, S. Fuentes, A. Castro-Alvarez, and E. Chavez-Angel, "Review on sol-gel synthesis of perovskite and oxide nanomaterials", *Gels*, vol. 7, no. 4, 2021, issn: 2310-2861. doi: 10.3390/gels7040275

[134] D. B. Emrie, "Sol–gel synthesis of nanostructured mesoporous silica powder and thin films", *Journal of Nanomaterials*, vol. 2024, no. 1, p. 6 109 770, 2024. doi: 10.1155/2024/6109770

[135] M. J. Mosquera, D. M. de los Santos, L. Valdez-Castro, and L. Esquivias, "New route for producing crack-free xerogels: Obtaining uniform pore size", *Journal of Non-Crystalline Solids*, vol. 354, no. 2, pp. 645–650, 2008, Physics of Non-Crystalline Solids 11, issn: 0022-3093. doi: 10.1016/j.jnoncrysol.2007.07.095

[136] T. J. Garino, "The cracking of sol–gel films during drying", in *MRS Online Proceedings Library*, vol. 180, Materials Research Society, 1990, p. 497. doi: 10.1557/PROC-180-497

[137] A. Fatima et al., “Comparative study of sol-gel and co-precipitation techniques for synthesizing calotropis procera-mediated bismuth ferrite for biomedical and environmental applications”, *Results in Chemistry*, vol. 15, p. 102 149, 2025, issn: 2211-7156. doi: 10.1016/j.rechem.2025.102149

[138] J. Cai et al., “Characterization of ce,ca:luag ceramic scintillators fabricated from co-precipitated powders”, *Optical Materials*, vol. 133, p. 113 051, 2022, issn: 0925-3467. doi: 10.1016/j.optmat.2022.113051

[139] Hamamatsu. “Operating principle streak camera”, Accessed: Oct. 13, 2025. [Online]. Available: https://www.hamamatsu.com/jp/en/product/photometry-systems/streak-camera/operating-principle.html

[140] J. C. de Mello, H. F. Wittmann, and R. H. Friend, “An improved experimental determination of external photoluminescence quantum efficiency”, *Advanced Materials*, vol. 9, no. 3, pp. 230–232, 1997. doi: 10.1002/adma.19970090308

[141] S. Leyre et al., “Absolute determination of photoluminescence quantum efficiency using an integrating sphere setup”, *Review of Scientific Instruments*, vol. 85, no. 12, p. 123 115, Dec. 2014, issn: 0034-6748. doi: 10.1063/1.4903852

[142] B. Dierre, X. Yuan, and T. Sekiguchi, “Low-energy cathodoluminescence microscopy for the characterization of nanostructures”, *Science and Technology of Advanced Materials*, vol. 11, no. 4, p. 043 001, 2010, PMID: 27877341. doi: 10.1088/1468-6996/11/4/043001

[143] N. Varkentina et al., “Cathodoluminescence excitation spectroscopy: Nanoscale imaging of excitation pathways”, *Science Advances*, vol. 8, no. 40, eabq4947, 2022. doi: 10.1126/sciadv.abq4947

[144] Z. Xia and A. Meijerink, “Ce3+-doped garnet phosphors: Composition modification, luminescence properties and applications”, *Chemical Society Reviews*, vol. 46, no. 1, pp. 275–299, Jan. 2017, issn: 0306-0012. doi: 10.1039/c6cs00551a

[145] Attolight, *Cathodoluminescene – what it is and how it works*, Accessed: 2026-03-12, 2018. [Online]. Available: https://www.azonano.com/article.aspx?ArticleID=4735

[146] G. Blasse and A. Bril, "A new phosphor for flying spot cathode ray tubes for color television: Yellow emitting y3al5o12–ce3+", *Applied Physics Letters*, vol. 11, no. 2, pp. 53–55, Jul. 1967, issn: 0003-6951. doi: 10.1063/1.1755025

[147] L. Chen et al., "Charge deformation and orbital hybridization: Intrinsic mechanisms on tunable chromaticity of $Y_3Al_5O_{12} : Ce^{3+}$ luminescence by doping Gd^{3+} for warm white leds", *Scientific Reports*, vol. 5, p. 11 514, 2015. doi: 10.1038/srep11514

[148] S. Fu, J. Tan, X. Bai, S. Yang, L. You, and Z. Du, "Effect of al/ga substitution on the structural and luminescence properties of y3(al1-xgax)5o12: Ce3+ phosphors", *Optical Materials*, vol. 75, pp. 619–625, 2018, issn: 0925-3467. doi: 10.1016/j.optmat.2017.11.021

[149] O. Sidletskiy et al., "Engineering of bulk and fiber-shaped yagg:ce scintillator crystals", *CrystEngComm*, vol. 19, no. 6, pp. 1001–1007, 2017. doi: 10.1039/C6CE02330D

[150] Advatech UK, *Yag:ce scintillation crystal*, https://www.advatech-uk.co.uk/yag_ce.html, Accessed: 2025-10-18, 2025.

[151] Crytur, *Yag:ce scintillation crystal*, https://www.crytur.com/materials/yag-ce/, Accessed: 2025-11-26, 2025.

[152] S. Akiyama et al., "Fabrication of high-efficiency yag:ce3+ phosphors via concurrent optimization of firing atmosphere and fluxing agent", *Optical Materials*, vol. 128, p. 112 386, 2022, issn: 0925-3467. doi: 10.1016/j.optmat.2022.112386

[153] S. R. Rotman, H. L. Tuller, and C. Warde, "Defect-property correlations in garnet crystals. vi. the electrical conductivity, defect structure, and optical properties of luminescent calcium and cerium-doped yttrium aluminum garnet", *Journal of Applied Physics*, vol. 71, no. 3, pp. 1209–1214, 1992. doi: 10.1063/1.351289

[154] M. Nikl, E. Mihokova, J. Pejchal, A. Vedda, Y. Zorenko, and K. Nejezchleb, "The antisite Lu~~-~~Al defect–related trap in $Lu_3Al_5O_{12}$:Ce single crystal", *physica status solidi (b)*, vol. 242, no. 14, R119–R121, 2005. doi: 10.1002/pssb.200541225

[155] O. Zapadlík, M. Nikl, J. Polák, P. Průša, and V. Linhart, "Engineering of yag:ce to improve its scintillation properties", *Optical Materials: X*, vol. 15, p. 100 165, 2022, issn: 2590-1478. doi: 10.1016/j.omx.2022.100165

[156] M. A. Spurrier, P. Szupryczynski, K. Yang, A. A. Carey, and C. L. Melcher, "Effects of Ca^{2+} co-doping on the scintillation properties of lso:ce", *IEEE Transactions on Nuclear Science*, vol. 55, no. 3, pp. 1178–1182, 2008. doi: 10.1109/TNS.2007.913486

[157] J. M. Ogiegło, A. Katelnikovas, A. Zych, T. Jüstel, A. Meijerink, and C. R. Ronda, "Luminescence and luminescence quenching in gd3(ga,al)5o12 scintillators doped with ce3+", *The Journal of Physical Chemistry A*, vol. 117, no. 12, pp. 2479–2484, Mar. 2013, issn: 1089-5639. doi: 10.1021/jp309572p

[158] Z. Song et al., "After-glow, luminescent thermal quenching, and energy band structure of ce-doped yttrium aluminum-gallium garnets", *Journal of Luminescence*, vol. 192, pp. 1278–1287, 2017, issn: 0022-2313. doi: 10.1016/j.jlumin.2017.09.008

[159] A. M. Stoneham, *Theory of Defects in Solids: Electronic Structure of Defects in Insulators and Semiconductors*. Oxford University Press, Feb. 2001, isbn: 9780198507802. doi: 10.1093/acprof:oso/9780198507802.001.0001

[160] S. Nargelas et al., "Influence of matrix composition and its fluctuations on excitation relaxation and emission spectrum of ce ions in (gdx y1-x)3al2ga3o12:ce scintillators", *Journal of Luminescence*, vol. 242, p. 118 590, 2022, issn: 0022-2313. doi: 10.1016/j.jlumin.2021.118590

[161] Y. Zorenko, T. Zorenko, P. Malinowski, O. Sidletskiy, and S. Neicheva, "Luminescent properties of y3al5−xgaxo12:ce crystals", *Journal of Luminescence*, vol. 156, pp. 102–107, 2014, issn: 0022-2313. doi: 10.1016/j.jlumin.2014.07.011

[162] Y. Zorenko et al., "Time-resolved luminescent spectroscopy of yag:ce single crystal and single crystalline films", *Radiation Measurements*, vol. 45, no. 3, pp. 395–397, 2010, Proceedings of the 7th European Conference on Luminescent Detectors and Transformers of Ionizing Radiation (LUMDETR 2009), issn: 1350-4487. doi: 10.1016/j.radmeas.2009.10.106

[163] Y. Zorenko et al., “Single crystalline film scintillators based on ce- and pr-doped aluminium garnets”, *Radiation Measurements*, vol. 42, no. 4, pp. 521–527, 2007, Proceedings of the 6th European Conference on Luminescent Detectors and Transformers of Ionizing Radiation (LUMDETR 2006), issn: 1350-4487. doi: 10.1016/j.radmeas.2007.01.045

[164] B. Sabot et al., “A compact detector system for simultaneous measurements of the light yield non-linearity and timing properties of scintillators”, *Scientific Reports*, vol. 14, p. 6960, 2024. doi: 10.1038/s41598-024-57186-9

[165] G. Tamulaitis et al., “Improvement of the time resolution of radiation detectors based on gd3al2ga3o12 scintillators with sipm readout”, *IEEE Transactions on Nuclear Science*, vol. 66, no. 7, pp. 1879–1888, 2019. doi: 10.1109/TNS.2019.2919898

[166] J. Bok and P. Schauer, “Performance of sem scintillation detector evaluated by modulation transfer function and detective quantum efficiency function”, *Scanning*, vol. 36, no. 4, pp. 384–393, 2014. doi: 10.1002/sca.21130

[167] T. Hirano et al., “Development of EB inspection system EBeyeM for EUV mask”, in *Photomask Technology 2010*, M. W. Montgomery and W. Maurer, Eds., International Society for Optics and Photonics, vol. 7823, SPIE, 2010, p. 78232C. doi: 10.1117/12.864208

[168] P. Schauer, O. Lalinský, M. Kučera, Z. Lučeničová, and M. Hanuš, “Effect of mg co-doping on cathodoluminescence properties of lugagg:ce single crystalline garnet films”, *Optical Materials*, vol. 72, pp. 359–366, 2017, issn: 0925-3467. doi: 10.1016/j.optmat.2017.06.028

[169] R. Autrata, P. Schauer, J. Kvapil, and J. Kvapil, “Single-crystal aluminates – a new generation of scintillators for scanning electron microscopes and transparent screens in electron optical devices”, *Scanning Electron Microscopy*, vol. II, pp. 489–500, 1983.

[170] Luxium Solutions, *Lyso scintillation crystals*, https://luxiumsolutions.com/radiation-detection-scintillators/crystal-scintillators/lyso-scintillation-crystals, Accessed: 2025-10-10, 2025.

[171] Advatech UK, *Luag:ce scintillation crystal*, https://www.advatech-uk.co.uk/luag_ce.html, Accessed: 2025-12-15, 2025.

[172] K. Kamada et al., "Composition engineering in cerium-doped (lu,gd)3(ga,al)5o12 single-crystal scintillators", *Crystal Growth & Design*, vol. 11, no. 10, pp. 4484–4490, 2011. doi: 10.1021/cg200694a

[173] K. Bartosiewicz et al., "A study of mg2+ ions effect on atoms segregation, defects formation, luminescence and scintillation properties in ce3+ doped gd3al2ga3o12 single crystals", *Journal of Alloys and Compounds*, vol. 905, p. 164 154, 2022, issn: 0925-8388. doi: 10.1016/j.jallcom.2022.164154

[174] M. Lucchini et al., "Effect of mg2+ ions co-doping on timing performance and radiation tolerance of cerium doped gd3al2ga3o12 crystals", *Nuclear Instruments and Methods in Physics Research Section A: Accelerators, Spectrometers, Detectors and Associated Equipment*, vol. 816, pp. 176–183, 2016, issn: 0168-9002. doi: 10.1016/j.nima.2016.02.004

[175] G. Dantelle et al., "Research on efficient fast scintillators: Evidence and x-ray absorption near edge spectroscopy characterization of ce4+ in ce3+, mg2+-co-doped gd3al2ga3o12 garnet crystal", *physica status solidi (b)*, vol. 257, no. 8, p. 1 900 510, 2020. doi: 10.1002/pssb.201900510

[176] M. Kučera, K. Nitsch, M. Nikl, M. Hanuš, and S. Daniš, "Growth and characterization of yag and luag epitaxial films for scintillation applications", *Journal of Crystal Growth*, vol. 312, no. 9, pp. 1538–1545, 2010, issn: 0022-0248. doi: 10.1016/j.jcrysgro.2010.01.023

[177] L. Martinazzoli et al., "Compositional engineering of multicomponent garnet scintillators: Towards an ultra-accelerated scintillation response", *Materials Advances*, vol. 3, no. 17, pp. 6842–6852, Sep. 2022, issn: 2633-5409. doi: 10.1039/d2ma00626j

[178] M. Kučera, K. Nitsch, M. Nikl, and M. Hanuš, "Defects in ce-doped luag and yag scintillation layers grown by liquid phase epitaxy", *Radiation Measurements*, vol. 45, no. 3, pp. 449–452, 2010, Proceedings of the 7th European Conference on Luminescent Detectors and Transformers of Ionizing Radiation (LUMDETR 2009), issn: 1350-4487. doi: 10.1016/j.radmeas.2009.12.031

[179] P. Průša et al., "Garnet scintillators of superior timing characteristics: Material, engineering by liquid phase epitaxy", *Advanced Optical Materials*, vol. 5, no. 6, p. 1 600 875, 2017. doi: 10.1002/adom.201600875

[180] P. Prusa et al., "Tailoring and optimization of luag:ce epitaxial film scintillation properties by mg co-doping", *Crystal Growth & Design*, vol. 18, no. 9, pp. 4998–5007, 2018. doi: 10.1021/acs.cgd.8b00411

[181] D. Mateika, E. Völkel, and J. Haisma, "Lattice-constant-adaptable crystallographics: Ii. czochralski growth from multicomponent melts of homogeneous mixed-garnet crystals", *Journal of Crystal Growth*, vol. 102, no. 4, pp. 994–1013, 1990, issn: 0022-0248. doi: 10.1016/0022-0248(90)90870-Q

[182] V. Dormenev et al., "Multipurpose ce-doped ba-gd silica glass scintillator for radiation measurements", *Nuclear Instruments and Methods in Physics Research Section A: Accelerators, Spectrometers, Detectors and Associated Equipment*, vol. 1015, p. 165 762, 2021, issn: 0168-9002. doi: 10.1016/j.nima.2021.165762

[183] N. Chiodini et al., "High-efficiency sio_2:ce^{3+} glass scintillators", *Applied Physics Letters*, vol. 81, no. 23, pp. 4374–4376, 2002. doi: 10.1063/1.1524294

[184] M. Skruodiene et al., "Synthesis and investigation of novel optical active sio2 glasses with entrapped yag:ce synthesized via sol–gel method", *Gels*, vol. 9, no. 6, 2023, issn: 2310-2861. doi: 10.3390/gels9060488

[185] K. Kajihara, "Recent advances in sol–gel synthesis of monolithic silica and silica-based glasses", *Journal of Asian Ceramic Societies*, vol. 1, no. 2, pp. 121–133, 2013. doi: 10.1016/j.jascer.2013.04.002

[186] M. M. Kuklja, "Defects in yttrium aluminium perovskite and garnet crystals: Atomistic study", *Journal of Physics: Condensed Matter*, vol. 12, no. 13, pp. 2953–2967, 2000. doi: 10.1088/0953-8984/12/13/307

[187] A. Lenef, J. F. Kelso, and A. Piquette, "Light extraction from luminescent light sources and application to monolithic ceramic phosphors", *Opt. Lett.*, vol. 39, no. 10, pp. 3058–3061, May 2014. doi: 10.1364/OL.39.003058

[188] M. Oishi et al., “Enhanced quantum efficiency of a self-organized silica mixed red phosphor caalsin3:eu”, *Journal of Solid State Chemistry*, vol. 309, p. 122 968, 2022, issn: 0022-4596. doi: 10.1016/j.jssc.2022.122968

[189] A. Baraban, S. Samarin, V. Prokofiev, V. Dmitriev, A. Selivanov, and Y. Petrov, “Luminescence of sio2 layers on silicon at various types of excitation”, *Journal of Luminescence*, vol. 205, pp. 102–108, 2019, issn: 0022-2313. doi: 10.1016/j.jlumin.2018.09.009

[190] Y. Talochka, S. Nargelas, Ž. Podlipskas, M. Kucera, Z. Lucenicova, and G. Tamulaitis, “Acceleration of emission decay in ce-doped gd-containing garnets by aliovalent codoping due to blocking excitation transfer via gadolinium subsystem”, *Radiation Physics and Chemistry*, vol. 218, p. 111 589, 2024, issn: 0969-806X. doi: 10.1016/j.radphyschem.2024.111589

[191] E. Zych, C. Brecher, and J. Glodo, “Kinetics of cerium emission in a YAG:Ce single crystal: The role of traps”, *Journal of Physics: Condensed Matter*, vol. 12, no. 8, pp. 1947–1958, Feb. 2000. doi: 10.1088/0953-8984/12/8/336

[192] Y. Zorenko et al., “Exciton and antisite defect-related luminescence in lu3al5o12 and y3al5o12 garnets”, *physica status solidi (b)*, vol. 244, no. 6, pp. 2180–2189, 2007. doi: 10.1002/pssb.200642431

[193] Y. V. Zorenko, I. V. Konstankevych, V. V. Mikhailin, V. N. Kolobanov, and D. A. Spasskii, “Luminescence of excitons in single-crystal garnets”, *Optics and Spectroscopy*, vol. 96, no. 3, pp. 390–397, 2004. doi: 10.1134/1.1690031

[194] E. Mihóková et al., “Luminescence and scintillation properties of yag:ce single crystal and optical ceramics”, *Journal of Luminescence*, vol. 126, no. 1, pp. 77–80, 2007, issn: 0022-2313. doi: 10.1016/j.jlumin.2006.05.004

SANTRAUKA

Įvadas

Scintiliuojančios medžiagos yra neatsiejama daugelio šiuolaikinių technologijų dalis. Literatūros apžvalga atskleidžia plačias jų taikymo galimybes: nuo medicininio vaizdinimo iki didelės energijos fizikos (HEP) eksperimentų [1], [2], [3], [4]. Scintiliatorius yra medžiaga, gebanti sugerti didelės energijos spinduliuotę ir paverčianti ją šviesa, dažniausiai ultravioletinėje arba regimojoje spektro srityje [5], [6]. Toks energijos virsmas leidžia aptikti ir kiekybiškai įvertinti spinduliuotę, kurios kitu būdu tiesiogiai užregistruoti nebūtų galima. Dėl šios savybės scintiliatoriai plačiai taikomi įvairiose srityse: nuo buityje naudojamų baltų šviestukų (wLED) iki pažangių medicininio vaizdinimo sistemų ir CERN vykstančių dalelių fizikos eksperimentų [7], [8], [9].
Ankstyvuoju scintiliatorių vystymo laikotarpiu jiems buvo keliami gana fundamentalūs reikalavimai: gebėjimas aptikti didelės energijos spinduliuotę išspinduliuojant išmatuojamą regimosios šviesos signalą [10]. Ilgainiui pageidaujamų medžiagos savybių sąrašas gerokai išsiplėtė ir pradėjo priklausyti konkrečios taikymo srities reikalavimų. Didelė šviesos išeiga (LY), spartus scintiliacinis atsakas, t.y. trumpa signalo augimo ir gesimo trukmė, bei gera energinė skyra yra tik dalis savybių, kurių reikšmė priklauso nuo konkrečios scintiliatoriaus paskirties [11]. Pavyzdžiui, CERN vykdomuose eksperimentuose norima pasiekti maždaug 10 ps laikinę skyrą [4]. Be to, tokiomis sąlygomis detektorius veikia itin didelės spinduliuotės dozės ir intensyvūs dalelių srautai, todėl naudojamos scintiliacinės medžiagos turi išlaikyti stabilias liuminescencines charakteristikas net ir esant ekstremalioms veikimo sąlygoms.
Tarp įvairių medžiagų klasių pastaruoju metu itin perspektyviais yra laikomi granato struktūros scintiliatoriai. Didelis jų tankis yra svarbus registruojant didelės energijos daleles, o plačios cheminės sudėties keitimo galimybės ypač aktualios HEP taikymams [12]. Granato kristalinė gardelė leidžia dalį jonų pakeisti kitais neardant kristalinės struktūros. Toks struktūrinis lankstumas suteikia galimybę kryptingai keisti scintiliacines savybes legiruojant medžiagą arba keičiant jos cheminę sudėtį.
Cerio jonai laikomi itin efektyviais liuminescencijos aktyvatoriais dėl spartaus $5d \rightarrow 4f$ optinio šuolio [13]. Sugėrus didelės energijos spinduliuotę, medžiagoje susidarę krūvininkai perduoda energiją aktyvatoriaus jonams, o jų suža-

dintų būsenų relaksacija lemia scintiliacinės šviesos emisiją. Todėl sparti Ce^{3+} sužadintos būsenos relaksacija sudaro prielaidas trumpai scintiliacinio atsako trukmei. Tačiau realiose medžiagose šis procesas priklauso ne tik nuo pačių aktyvatoriaus jonų savybių, bet ir nuo kristalinės gardelės kokybės bei joje esančių defektų [14]. Krūvininkų gaudyklės gali laikinai sulaikyti sužadinimo metu susidariusius elektronus ar skyles ir taip sutrikdyti tiesioginį energijos perdavimą Ce^{3+} jonams. Dėl šios priežasties su gaudyklėmis susiję procesai yra vienas iš pagrindinių veiksnių, ribojančių platesnį Ce aktyvuotų granato struktūros scintiliatorių taikymą tokiose srityse kaip CERN eksperimentai [15]. Krūvininkų išlaisvinimas iš gaudyklių gali vykti gerokai lėčiau nei pirminis scintiliacijos procesas, todėl atsiranda uždelstosios emisijos komponentės ir pailgėja bendras scintiliacinis atsakas. Be to, dalis krūvininkų gali rekombinuoti nespinduliniu būdu, todėl mažėja ne tik atsako greitis, bet ir bendras liuminescencijos efektyvumas.

Kitas svarbus uždavinys yra suderinti didelę šviesos išeigą ir spartų scintiliacinį atsaką. Skirtingose taikymo srityse šių savybių svarba nevienoda, todėl vienai paskirčiai optimizuotos medžiagos nebūtinai yra tinkamos kitai. Pavyzdžiui, wLED gamyboje naudojamoms medžiagoms svarbus didelis fotoliuminescencijos intensyvumas ir emisijos stabilumas, o didelės energijos fizikos eksperimentuose, tokiuose kaip vykdomi CERN, itin svarbus ir trumpa scintiliacinio atsako trukmė. Todėl medžiagų, kuriose būtų optimaliai suderintos šios savybės, paieška tebėra sudėtingas uždavinys.

Vienas iš būdų kryptingai keisti scintiliacines charakteristikas yra kristalinės matricos legiravimas papildomais jonais. Tačiau legiranto poveikis neapsiriboja vien norimos optinės savybės pagerinimu. Papildomų jonų įterpimas gali pakeisti vietinę kristalinės gardelės aplinką, paskatinti struktūrinių defektų susidarymą ir paveikti krūvininkų pernašos bei rekombinacijos procesus [16]. Be to, galimų legirantų pasirinkimą riboja jų suderinamumas su konkrečia gardelės struktūra ir taikomomis sintezės ar kristalų auginimo sąlygomis. Dėl šios priežasties, siekiant pagerinti scintiliatoriaus savybes, svarbu vertinti ne tik paties legiranto poveikį liuminescencijos centrui, bet ir jo įtaką visai medžiagos elektroninei struktūrai. Viena iš tokių strategijų yra draustinio tarpo inžinerija. Keičiant laidumo juostos (CB) dugno padėtį galima keisti sekliųjų elektronų gaudyklių energetinį gylį ir taip sumažinti jų įtaką krūvininkų pernašai bei scintiliacijos kinetikai [15]. Tačiau toks elektroninės struktūros pakeitimas gali turėti ir nepageidaujamų pasekmių, pavyzdžiui, sumažinti medžiagos atsparumą terminei jonizacijai. Todėl aktualu rasti tokias pagrindines medžiagas ir jų

sudėtis, kuriose draustinio tarpo inžinerija leistų kryptingai reguliuoti scintiliacines charakteristikas, kartu išlaikant tinkamą šviesos išeigos, atsako greičio ir terminio stabilumo pusiausvyrą.

Vienas iš praktiškai taikomų būdų keisti Ce aktyvuotų granato struktūros scintiliatorių savybes yra jų kolegiravimas kitavalenčiais jonais. Tyrimai parodė, kad Ca^{2+} arba Mg^{2+} jonų įterpimas į tokių medžiagų kristalinę gardelę gali paspartinti scintiliacinį atsaką [17]. Vis dėlto toks kolegiravimas dažniausiai taikomas esant nedidelėms legirantų koncentracijoms, nes didesnis kitavalenčių jonų kiekis gali lemti PL intensyvumo sumažėjimą ir sustiprinti nespindulinės rekombinacijos procesus. Šie pokyčiai mokslinėje literatūroje dažnai siejami su Ce^{4+} jonų stabilizacija [18]. Tačiau vien šiuo modeliu ne visada galima nuosekliai paaiškinti visus eksperimentinius rezultatus. Tai ypač aktualu tais atvejais, kai tiek rezonansinis žadinimas, tiek žadinimas didelės energijos elektronų srautu lemia panašias PL gesimo charakteristikas. Tokie stebėjimai rodo, kad kitavalenčio kolegiravimo poveikį gali lemti ne tik cerio oksidacijos būsenos pokyčiai, bet ir kiti su kristalinės gardelės defektais bei krūvininkų rekombinacija susiję procesai.

Šių medžiagų savybių optimizavimas tampa ypač aktualus atsižvelgiant į CERN vykdomus technologinius atnaujinimus. Vienas svarbiausių šiuo metu įgyvendinamų projektų yra HL-LHC (angl. *High-Luminosity Large Hadron Collider*) greitintuvo atnaujinimas, kuriam reikalingos medžiagos, pasižyminčios dideliu šviesos našumu, sparčiu scintiliaciniu atsaku ir atsparumu intensyviai apšvitai [11], [19]. Tačiau praktiniam tokių medžiagų taikymui svarbios ne tik jų optinės ir scintiliacinės charakteristikos, bet ir gamybos sąnaudos. Dėl šios priežasties kartu ieškoma alternatyvių sintezės metodų, kurie ekonominiu ir laiko sąnaudų požiūriu galėtų būti pranašesni už įprastus monokristalų auginimo metodus. Viena iš galimų alternatyvų yra dviejų etapų zolio-gelio sintezės metodas. Šis metodas, palyginus su įprastais kristalų auginimo būdais, suteikia didelį lankstumą keičiant medžiagos cheminę sudėtį ir gali leisti sutrumpinti sintezės trukmę bei sumažinti gamybos sąnaudas. Vis dėlto, siekiant įvertinti šio metodo tinkamumą scintiliacinių medžiagų gamybai, būtinas išsamus taip susintetintų medžiagų struktūrinių, optinių ir scintiliacinių savybių charakterizavimas.

Tikslas, uždaviniai ir mokslinis naujumas

Šiame darbe tirta Ce aktyvuotų granato struktūros scintiliatorių serija. Nors visi tirti scintiliatoriai priklauso tai pačiai granatų šeimai, lyginant tarpusavyje jie reikšmingai skiriasi sudėtimi (pvz., YAG, LuAG), kuri daro stiprią įtaką jų liuminescencijos ir scintiliacinėms savybėms. Be to, tirtos medžiagos užaugintos skirtingais gamybos metodais ir taikytos skirtingos medžiagų inžinerijos strategijos, kuriomis siekiama pagerinti scintiliatorių charakteristikas arba sukurti ekonomiškesnius jų gamybos būdus. **Šio darbo tikslas** – nustatyti procesus, ribojančius Ce jonais aktyvuotų granato struktūros scintiliatorių emisijos efektyvumą ir scintiliacinio atsako spartą, tiriant skirtingomis strategijomis optimizuotas pagrindines medžiagas, įskaitant draustinės juostos inžineriją, didelės koncentracijos kitavalentį legiravimą ir kompozitų gamybą taikant dviejų etapų zolio-gelio metodą.

Šiam tikslui pasiekti buvo **iškeltas uždavinys**: charakterizuoti Ce jonais aktyvuotus granato struktūros scintiliatorius, taikant eksperimentinių metodų rinkinį, apimantį fotoliuminescencijos (PL), laikinės skyros fotoliuminescencijos (TRPL), kvantinio našumo (QY) ir katodoliuminescencijos (CL) matavimus įvairiomis eksperimentinėmis sąlygomis, kai naudojami skirtingi žadinimo režimai, žadinimo energijos tankis bei keičiama bandinio temperatūra.

Pirmajame skyriuje sistemiškai tiriama galio kiekio įtaka $Y_3(Al_{1-x}Ga_x)_5O_{12}$:Ce scintiliatorių savybėms plačiame sudėties intervale, nuo $x = 0$ iki $x = 1$. Šio skyriaus naujumas – nustatytas galio kiekio intervalas, kuriame galima optimizuoti kvantinį našumą ir scintiliacinio atsako spartą.

Antrajame skyriuje parodyta, kad Ce jonais aktyvuotus LuGAGG granatų scintiliatorius stipriai legiruojant kitavalenčiais Mg^{2+} jonais, reikšmingai sutrumpėja liuminescencijos gesimo trukmė, tačiau kartu sumažėja ir fotoliuminescencijos intensyvumas. Šio skyriaus naujumas – nustatytas alternatyvus šį reiškinį lemiantis mechanizmas, parodant, kad stebimus pokyčius lemia papildomo emisijos centro susidarymas.

Trečiajame skyriuje pristatomas Ce aktyvuotų granato tipo scintiliatorių, susintetintų taikant dviejų etapų zolio-gelio metodą, tyrimas. Šio skyriaus naujumas – parodyta, kad dviejų etapų zolio-gelio metodas gali būti ekonomiškai ir technologiškai efektyvi alternatyva įprastiems scintiliatorių gamybos metodams.

Ginamieji teiginiai

1 Teiginys Galio kiekio didinimas $Y_3(Al_{1-x}Ga_x)_5O_{12}$:Ce scintiliatoriuose iki $x \sim 0.7$ sumažina terminės jonizacijos barjerą ir santykį tarp liuminescencijos gesimo trukmės ir šviesos išeigos, taip pagerindamas scintiliatoriaus atsako spartą. Toliau didinant galio kiekį, scintiliatoriaus charakteristikos reikšmingai blogėja.

2 Teiginys Scintiliatoriaus LuGAGG:Ce papildomas legiravimas didele Mg^{2+} jonų koncentracija suformuoja pakitusių savybių emisijos centrus, kurie paspartina liuminescencijos gesimą dėl papildomo nuo temperatūros nepriklausančio nespindulinės rekombinacijos kanalo susidarymo ir sustiprėjusio terminio gesinimo, kuriam būdingas 0,2 eV barjeras, gerokai mažesnis nei įprastų Ce^{3+} centrų.

3 Teiginys Efektyvumo nuostolius Mg jonais papildomai legiruotuose LuGAGG:Ce daugiausia lemia nespindulinė rekombinacija Ce^{3+} emisijos centruose, o ne nuostoliai, atsirandantys sužadinimo energijos perdavimo metu.

4 Teiginys Kompozitiniai scintiliatoriai, sudaryti iš YAG:Ce, LuYAG:Ce ir LuAG:Ce mikrokristalitų silicio dioksido matricoje bei pagaminti taikant dviejų etapų zolio-gelio metodą, išlaiko pagrindines monokristalams būdingas fotoliuminescencines savybes: emisijos spektrų padėtį, fotoliuminescencijos gesimo spartą ir kvantinį našumą, kartu sudarydami galimybę sumažinti gamybos ir laiko sąnaudas.

Darbo struktūra

Disertacijos pradžioje pateikiama įvadinė dalis, kurioje pristatoma pagrindinė mokslinė problema, darbo naujumas ir pagrindiniai ginamieji teiginiai. Šioje dalyje taip pat pateikiama su disertacija susijusi informacija, įskaitant publikuotų mokslinių straipsnių ir konferencijose pristatytų pranešimų sąrašus. Toliau pateikiamą literatūros apžvalgą sudaro trys pagrindinės dalys: (1) fizikiniai procesai scintiliatoriuose, (2) scintiliatorių taikymo sritys ir (3) scintiliatorių gamyba. Eksperimentinių metodų skyriuje aprašomi šiame darbe taikyti fotoliuminescencijos, laikinės skyros liuminescencijos, kvantinio našumo ir katodoliuminescencijos matavimo metodai.

Eksperimentiniai rezultatai pateikiami trijuose skyriuose. Kiekvienas jų pradedamas trumpu įvadu, skirtu konkrečiam granato struktūros scintiliatoriui, po kurio pateikiami ir aptariami eksperimentiniai rezultatai. Kiekvieno skyriaus pabaigoje pateikiama rezultatų santrauka ir pagrindinės išvados. Pirmasis ginamasis teiginys pristatomas pirmajame skyriuje, antrasis ir trečiasis – antrajame, o ketvirtasis – trečiajame skyriuje.

Autoriaus indėlis

Eksperimentinius tyrimus ir jų duomenų analizę, susijusią su QY bei PL ir gesimo kinetikų temperatūrine priklausomybe, atliko šios disertacijos autorius. Eksperimentinius darbus ir duomenų analizę, susijusius su CL matavimais, atliko laboratorijos kolegos. Disertacijos autorius taip pat prisidėjo prie mokslinių publikacijų, parengtų remiantis šiame darbe pateikiamais rezultatais ir paskelbtų iki disertacijos pateikimo, rengimo.

Eksperimentiniai tyrimo metodai

Šiame darbe tiriamos scintiliatorių liuminescencinės charakteristikos, taikant fotoliuminescencijos ir katodoliuminescencijos metodus, taip pat nustatomos liuminescencijos gyvavimo trukmės ir kvantinės išeigos (QY) vertės. Principinė PL, TRPL ir QY matavimų schema pateikta Pav. 1. PL ir TRPL matavimai atliekami kambario temperatūroje arba naudojant kriogeninę sistemą, leidžiančią keisti bandinio temperatūrą nuo 78 iki 750 K. Optiniam Ce^{3+} centrų sužadinimui naudojama sistema, sudaryta iš Yb lazerio, generuojančio 170 fs trukmės impulsus ties 1030 nm bangos ilgiu, ir optinio parametrinio stiprintuvo (OPA). Keičiant OPA generuojamos spinduliuotės bangos ilgį, Ce^{3+} jonai gali būti rezonansiškai žadinami, vykstant $4f \rightarrow 5d$ elektroniniams šuoliams.

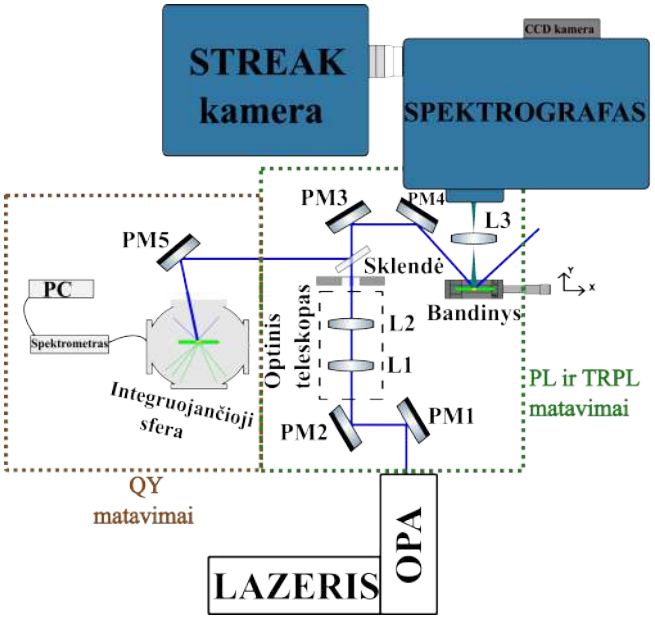

Pav. 1. PL, TRPL ir QY matavimams naudotos eksperimentinės įrangos principinė schema.

PL matavimo sistemą sudarė Kymera 328i spektrografas ir Hamamatsu UV-VIS CCD kamera. TRPL matavimai atlikti naudojant Hamamatsu UV-VIS juostinę (streak) kamerą, kurios laikinė skyra siekia 30 ps. QY matavimams naudota 6 colių integruojanti sfera. QY vertės nustatytos taikant trijų etapų

metodą: „Tuščia sfera“, „Netiesioginis žadinimas“ ir „Tiesioginis žadinimas“ (Pav. 2) [141]. Pirmuoju atveju („Tuščia sfera“) registruojama tik krintančioji spinduliuotė be bandinio. Antruoju („Netiesioginis žadinimas“) bandinys sužadinamas netiesiogiai, nuo integruojančios sferos paviršiaus atspindėta šviesa. Trečiuoju („Tiesioginis žadinimas“) bandinys sužadinamas tiesiogiai į jį krintančia spinduliuote. QY vertė apskaičiuojama integruojant lazerio liniją ir scintiliatoriaus emisiją atitinkančias spektro sritis.

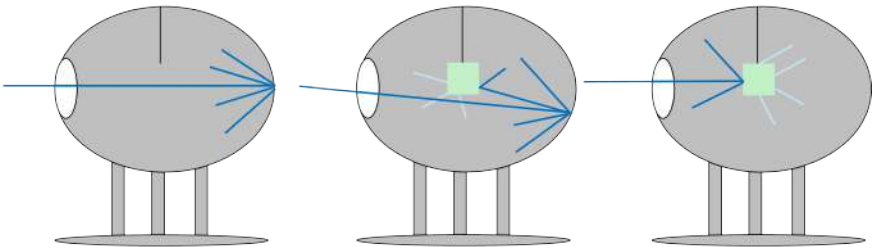

Pav. 2. Trijų etapų metodo, skirto QY matavimams naudojant integruojančią sferą, schema: (a) „Tuščia sfera“, (b) „Netiesioginis žadinimas“ ir (c) „Tiesioginis žadinimas“. Adaptuota pagal [141].

CL matavimų sistemos principinė veikimo schema pateikta Pav. 3. Ji apjungia skenuojantį elektroninį mikroskopą (SEM) ir CL detekcijos sistemą, leidžiančią analizuoti elektronų pluoštu sužadintų scintiliatorių spektrus. Sistemą sudaro aeroPULSE PL lazeriu valdoma elektronų patranka, Cassegrain tipo šviesos surinkimo objektyvas, Horiba iHR 320 spektrometras, Andor Newton 920 CCD kamera erdviniam vaizdui registruoti ir Hamamatsu C10910 juostinė kamera laikinei analizei. CL matavimai gali būti atliekami nuostoviu režimu, skirtu CL intensyvumo ir spektrinio pasiskirstymo analizei, arba impulsiniu režimu, leidžiančiu tirti emisijos kinetiką.

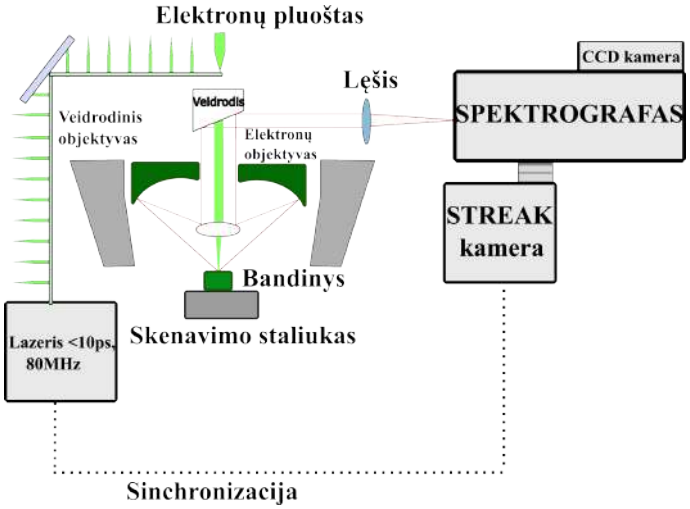

Pav. 3. CL matavimams naudotos eksperimentinės įrangos principinė schema. Adaptuota pagal [145].

Kadangi PL ir CL metodais inicijuojami skirtingi sužadinimo ir energijos perdavimo procesai, jų eksperimentiniai rezultatai šiame darbe lyginami tarpusavyje. Atliekant PL matavimus, Ce^{3+} centrai žadinami rezonansiškai, vykstant tiesioginiams $4f \rightarrow 5d$ elektroniniams šuoliams [144]. Tokiu atveju sužadinimas vyksta tiesiogiai Ce^{3+} centre, todėl išmatuotos liuminescencijos charakteristikos daugiausia atspindi pačių emisijos centrų relaksacijos procesus. CL atveju aukštos energijos elektronų pluoštas pirmiausia sužadina kristalinę matricą. Dėl nerezonansinio sužadinimo joje susidaro nepusiausvirieji elektronai ir skylės, kurie migruoja kristalinėje gardelėje, gali būti pagaunami defektuose arba perduoti sužadinimo energiją Ce^{3+} emisijos centrams. Todėl CL signalą lemia ne tik Ce^{3+} centrų relaksacija, bet ir prieš ją vykstantys krūvininkų generacijos, pernašos, pagavimo bei energijos perdavimo procesai. PL ir CL rezultatų palyginimas leidžia įvertinti krūvininkų pernašos ir jų pagavimo gaudyklėse įtaką liuminescencijos intensyvumui bei kinetikai ir atskirti šiuos procesus nuo spindulinės bei nespindulinės rekombinacijos, vykstančios pačiuose Ce^{3+} emisijos centruose.

Skyrius 1: $Y_3(Al_{1-x}Ga_x)_5O_{12}$:Ce

Itrio aliuminio granatas, aktyvuotas ceriu (YAG:Ce), yra vienas pirmųjų ceriu aktyvuotų granato struktūros scintiliatorių ir iki šiol plačiai tiriamas bei naudojamas pramonėje [146]. YAG kristalui būdinga kubinė gardelė, kurioje Y^{3+} jonai užima dodekaedrines pozicijas, o Al^{3+} jonai pasiskirsto tarp oktaedrinių ir tetraedrinių gardelės pozicijų. Į gardelę įterpti Ce^{3+} jonai pakeičia Y^{3+} jonus ir užima dodekaedrines gardelės pozicijas [147].

YAG:Ce medžiagos plačiai naudojamos dėl didelio QY bei gero cheminio ir mechaninio stabilumo. Jos taikomos wLED technologijoje [47], [148], jonizuojančiajai spinduliuotei registruoti medicinoje ir laikomos perspektyviomis būsimųjų HEP detektorių medžiagomis. Be to, palyginus su kai kuriais sunkesnių elementų turinčiais scintiliatoriais, YAG:Ce gali būti atsparesnis spinduliuotės sukeliamiems pažeidimams.

Visgi YAG:Ce vis dar turi reikšmingų trūkumų, ribojančių šios medžiagos taikymą HEP eksperimentuose. YAG:Ce liuminescencijos gesimo trukmė yra santykinai ilga [19], o spartų scintiliacinį atsaką papildomai riboja medžiagoje esančios elektronų gaudyklės (angl. *electron traps*). Jų kilmė dar nėra galutinai išaiškinta, tačiau elektronų gaudyklių susidarymas dažniausiai siejamas su deguonies vakansijomis ir kitais kristalinės gardelės defektais [153], [154], [155].

YAG:Ce scintiliaciniam atsakui gerinti taikomos dvi strategijos. Viena iš jų yra kolegiravimas dvivalenčiais jonais, tokiais kaip Mg^{2+} arba Ca^{2+}, kurie gali skatinti Ce^{4+} oksidacijos būsenos stabilizavimą ir sudaryti sąlygas spartesnei spindulinei rekombinacijai [18], [155], [156]. Antroji strategija yra draustinio tarpo inžinerija (angl. *band-gap engineering*), pavaizduota Pav. 4. Keičiant kristalo cheminę sudėtį modifikuojama jo juostinė struktūra ir mažinamas elektronų gaudyklių poveikis [15]. Vienas iš šios strategijos pavyzdžių yra dalinis Al^{3+} jonų pakeitimas Ga^{3+} jonais. Nedidelis galio kiekis gali paspartinti scintiliacinį atsaką ir padidinti LY [149]. Tačiau esant didesniam galio kiekiui gali sustiprėti liekamoji liuminescencija (angl. *persistent luminescence*). Galio įterpimas taip pat keičia emisijos spektrinę padėtį, o tai svarbu wLED taikymams [148], [149]. Šiame skyriuje tirtos ceriu aktyvuotų itrio aliuminio galio granatų optinės savybės, sistemingai keičiant galio dalį nuo 0 % iki 100 % (Lentelė 1). Bandiniai gauti iš Ukrainos tyrimų grupės, kurios vadovas – *Oleg Sidletskiy*.

Lentelė 1. Galio kiekis (x) $Y_3(Al_{1-x}Ga_x)_5O_{12}$:Ce bandiniuose.

$Y_3(Al_{1-x}Ga_x)_5O_{12}$:Ce
0,00
0,16
0,36
0,66
0,75
0,80
0,85
1,00

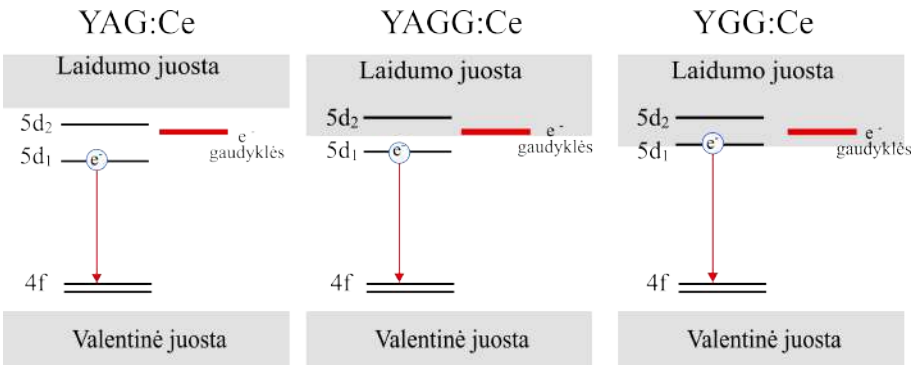

Pav. 4. Draustinio tarpo inžinerijos poveikio Ce^{3+} sužadintųjų $5d_1$ ir $5d_2$ energijos lygmenų padėtims $Y_3(Al_{1-x}Ga_x)_5O_{12}$:Ce bandiniuose, priklausomai nuo galio kiekio x, schema. Adaptuota pagal [149].

Pirmiausia išmatuoti visų aštuonių bandinių sugerties spektrai Pav. 5. Juose identifikuotos dvi pagrindinės sugerties juostos, atitinkančios optinius perėjimus iš pagrindinio Ce^{3+} jonų $4f$ energijos lygmens į sužadintuosius $5d_1$ ir $5d_2$ energijos lygmenis. Didinant Ga kiekį kristalinėje gardelėje, energijos skirtumas tarp $5d_1$ ir $5d_2$ lygmenų sumažėja nuo $\Delta E = 0{,}93$ eV iki $\Delta E = 0{,}54$ eV [47], [161]. Kaip nurodoma literatūroje, ΔE pokytis siejamas su kristalinio lauko stiprio kitimu Ce^{3+} jonų užimamose dodekaedrinėse gardelės pozicijose [47].

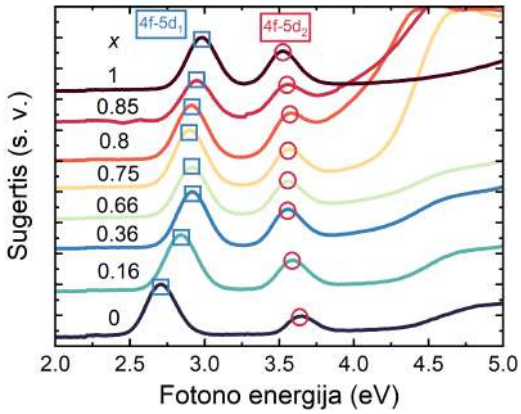

Pav. 5. $Y_3(Al_{1-x}Ga_x)_5O_{12}$:Ce bandinių su skirtingais galio kiekiais x sugerties spektrai.

PL spektrai matuoti 90–750 K temperatūros intervale. Bandiniai žadinti rezonansiškai, parenkant žadinimo energijas pagal sugerties spektruose nustatytas juostų, atitinkančių perėjimus į sužadintuosius $5d_1$ ir $5d_2$ energijos lygmenis, padėtis.

Visų tirtų bandinių emisijos spektrai, bandinio temperatūrą keičiant 100 K žingsniu, išmatuoti žadinant į $5d_1$ energijos lygmenį, pateikti Pav. 6. Bandiniuose, kuriuose galio kiekis yra x = 0,16–0,66, PL signalo intensyvumas išauga. Šis padidėjimas ryškiausiai matomas 90–500 K temperatūros intervale ir gali būti nulemtas mažesnių su defektais susijusių nespindulinių nuostolių Ce^{3+} centruose. Didinant temperatūrą iki 750 K, terminis gesinimas stiprėja, ypač bandiniuose su didesniu galio kiekiu, nes didėjant galio kiekiui mažėja terminės jonizacijos barjeras.

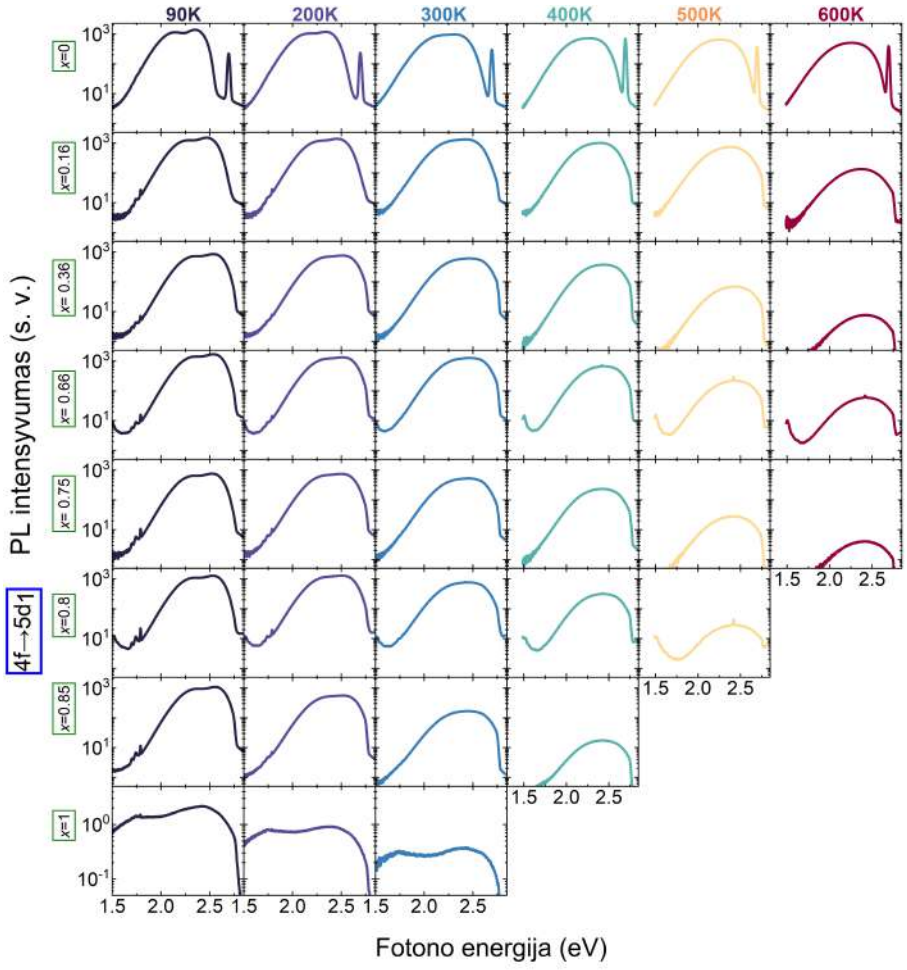

Pav. 6. $Y_3(Al_{1-x}Ga_x)_5O_{12}$:Ce bandinių PL spektrų temperatūrinės priklausomybės, žadinant į Ce^{3+} $5d_1$ lygmenį.

Pav. 7 pateiktos PL intensyvumo temperatūrinės priklausomybės analizuotos siekiant nustatyti aktyvacijos energiją, nusakančią terminės jonizacijos barjero aukštį. Tam taikyta Arrhenius lygtis (7.1), darant prielaidą, kad PL intensyvumo mažėjimą lemia vienas termiškai aktyvuotas nespindulinio gesimo kanalas. Analizuoti bandiniai, kuriuose galio kiekis neviršija $x = 0{,}66$, atskirai žadinant į Ce^{3+} jonų $5d_1$ ir $5d_2$ energijos lygmenis. Esant didesniam galio kiekiui, terminio gesinimo mechanizmas tampa sudėtingesnis ir negali būti tinkamai aprašytas modeliu įskaitančiu vieną energijos barjerą.

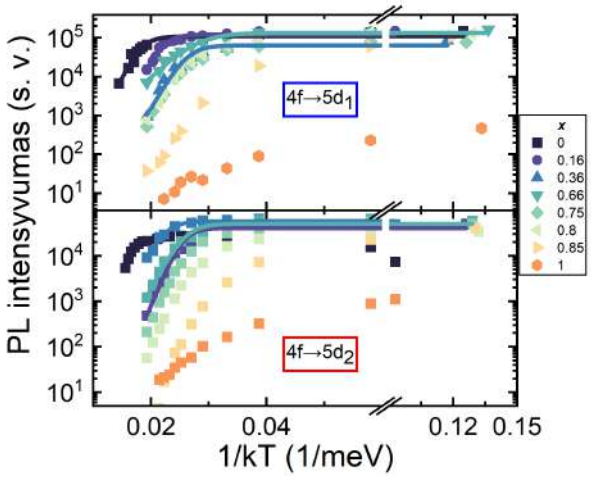

Pav. 7. $Y_3(Al_{1-x}Ga_x)_5O_{12}$:Ce bandinių PL intensyvumų temperatūrinės priklausomybės, žadinant į Ce^{3+} $5d_1$ ir $5d_2$ lygmenis.

$$V = \frac{V_0}{1 + A \cdot \exp\left(-\frac{E_a}{k_B T}\right)} \tag{7.1}$$

V_0 intensyvumas esant žemai temperatūrai ($k_b T \ll E_a$);
A tapatinimo konstanta;
k_B Boltzmanno konstanta.

Pav. 8 pateiktos PL gesimo kinetikos, registruotos emisijos maksimumo srityje 90–750 K temperatūros intervale, žadinant į Ce^{3+} jonų $5d_1$ ir $5d_2$ energijos lygmenis. YAG:Ce liuminescencijos gesimo trukmė kambario temperatūroje yra apie 55 ns ir dėl terminio gesinimo trumpėja augant temperatūrai, ir ties 745 K yra apie 18 ns. Bandinio, kuriame galio kiekis yra x = 0,85, liuminescencijos gesimo trukmė yra gerokai trumpesnė. Kambario temperatūroje ji siekia maždaug 10–13 ns, priklausomai nuo žadinimo energijos, o aukštesnėje temperatūroje tampa trumpesnė nei 1 ns.

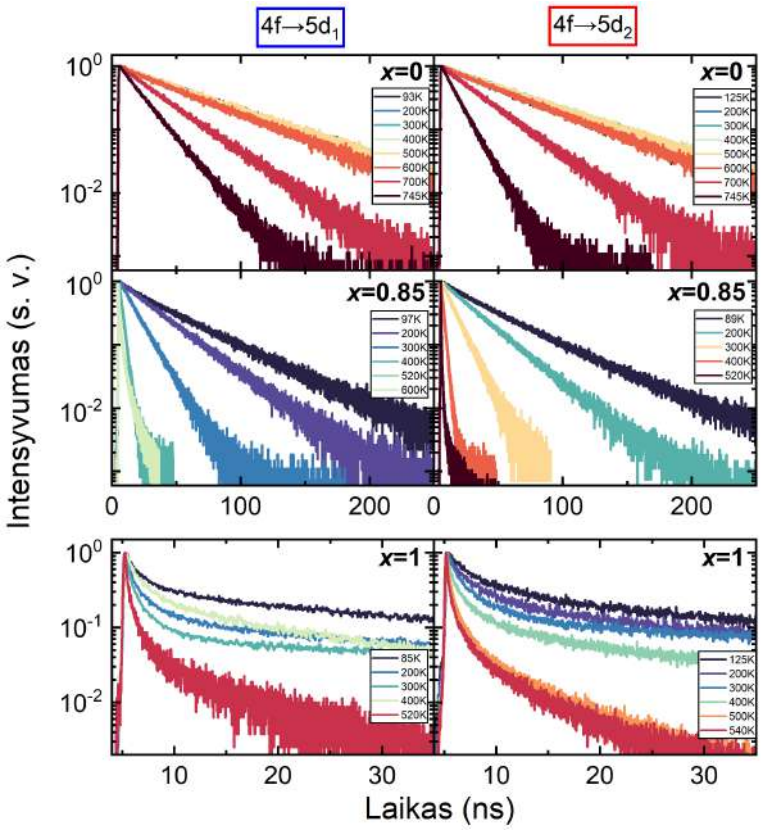

Pav. 8. Normuotos $Y_3(Al_{1-x}Ga_x)_5O_{12}$:Ce bandinių PL gesimo kinetikos temperatūrinės priklausomybės, žadinant į Ce^{3+} $5d_1$ ir $5d_2$ lygmenis.

Bandinių, kuriuose galio kiekis neviršija $x = 0{,}66$, liuminescencijos gesimo kinetikos visame tirtame temperatūros intervale gerai aprašomos vieneksponente funkcija, o esant didesniam galio kiekiui stebimi nukrypimai nuo vieneksponentės gesimo kinetikos (žr. Pav. 9).

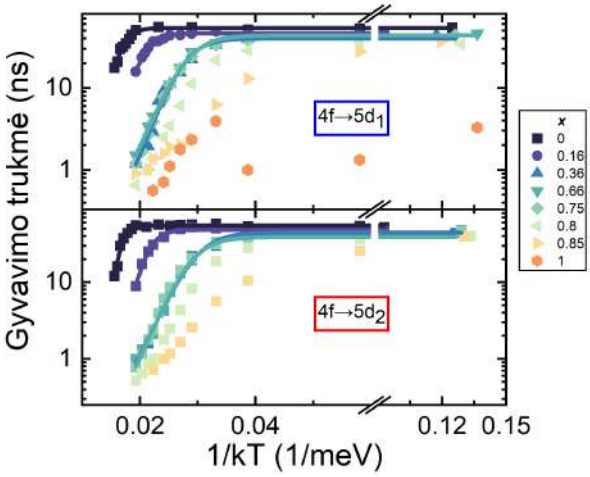

Pav. 9. $Y_3(Al_{1-x}Ga_x)_5O_{12}$:Ce bandinių PL gyvavimo trukmių temperatūrinės priklausomybės, žadinant į Ce^{3+} $5d_1$ ir $5d_2$ lygmenis.

Aktyvacijos energijos vertės, įvertintos iš PL intensyvumo ir gesimo trukmės temperatūrinių priklausomybių, pateiktos Lentelė 2. Galio įterpimas modifikuoja juostinę struktūrą, ir lemia Ce^{3+} sužadintųjų $5d_1$ ir $5d_2$ lygmenų priartėjimą prie CB dugno. Dėl to mažėja aktyvacijos energija ir stiprėja terminis gesinimas. PL intensyvumo ir gesimo trukmės temperatūrinės priklausomybės rodo, kad esant mažam galio kiekiui terminis gesinimas gali būti aprašytas vienu aktyvacijos barjeru. Kai galio kiekis viršija x=0,66, vieno barjero modelis nebetinka, nes prie terminio gesinimo prisideda alternatyvūs nespindulinės rekombinacijos kanalai.

Lentelė 2. $Y_3(Al_{1-x}Ga_x)_5O_{12}$:Ce bandinių su skirtingais galio kiekiais x aktyvacijos energijos E_a (meV), nustatytos iš PL intensyvumo ir gesimo trukmės temperatūrinių priklausomybių, žadinant į Ce^{3+} jonų $5d_1$ energijos lygmenį.

x	E_a (meV); PL intensyvumas	E_a (meV); Gyvavimo trukmė
0	684 ± 94	681 ± 63
0,16	628 ± 85	642 ± 60
0,36	534 ± 49	421 ± 29
0,66	333 ± 31	386 ± 14

QY matavimų rezultatai pateikti Pav. 10. Matavimai atlikti rezonansiškai ža-

dinant į Ce^{3+} jonų $5d_1$ ir $5d_2$ energijos lygmenis. Didėjant galio kiekiui iki x = 0,66, QY nežymiai didėja, tačiau esant didesniam Ga kiekiui QY vertės pradeda sparčiai mažėti. Toks QY kitimas siejamas su galio jonų pasiskirstymu tarp skirtingų kristalinės gardelės pozicijų. Esant mažam galio kiekiui, Ga^{3+} jonai pirmiausia pakeičia Al^{3+} jonus tetraedrinėse gardelės pozicijose. Didinant galio kiekį, vis didesnė Ga^{3+} jonų dalis pakeičia Al^{3+} jonus oktaedrinėse gardelės pozicijose [161].

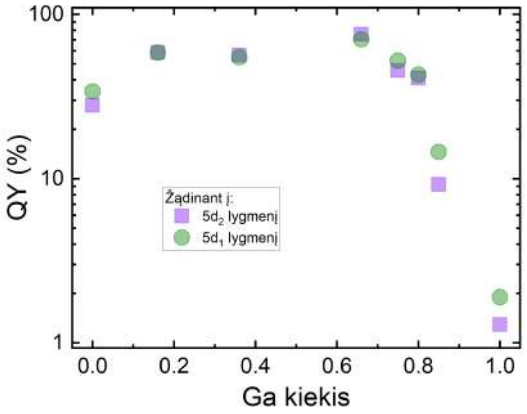

Pav. 10. $Y_3(Al_{1-x}Ga_x)_5O_{12}$:Ce bandinių QY priklausomybė nuo galio kiekio x, žadinant į Ce^{3+} $5d_1$ ir $5d_2$ lygmenis.

Pav. 11 pateiktuose CL spektruose stebima Ce^{3+} emisija 2,0–2,5 eV energijų intervale. Didėjant galio kiekiui, pagrindinė emisijos juosta pasislenka į didesnių energijų sritį. Daugumoje bandinių dominuoja Ce^{3+} emisija, tačiau YGG bandinyje (x = 1) ji yra stipriai nuslopinta ir atsiranda nauja emisijos juosta ties 2,0 eV. Taip pat stebima papildoma emisijos juosta ties 3,8 eV. Ji yra intensyviausia bandinyje be galio, silpnėja esant vidutiniam galio kiekiui ir vėl išryškėja YGG bandinyje. Ši juosta nėra susijusi su tipine Ce^{3+} emisija ir priskiriama su defektais susijusiai eksitonų rekombinacijai arba F^+ centrų liuminescencijai [162], [163]. Skirtingai nei ankstesniuose tyrimuose, kuriuose bandiniai žadinti rentgeno ir sinchrotronine spinduliuote, galio kiekiui esant intervale x=0,4–0,5 emisijos intensyvumo padidėjimas nebuvo stebėtas [16], [161]. Šis skirtumas siejamas su netiesiniu CL atsaku esant didesniam sužadinimo tankiui.

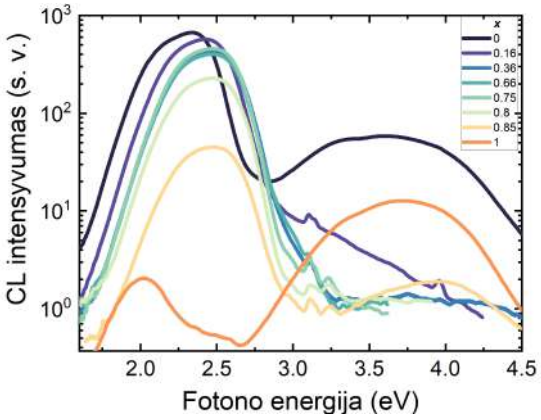

Pav. 11. $Y_3(Al_{1-x}Ga_x)_5O_{12}$:Ce bandinių su skirtingais galio kiekiais *x* CL spektrai.

Pav. 12 pateiktos CL gesimo kreivės rodo, kad gesimo trukmė, kuri įvertinta kaip laiko intervalas, per kurį emisijos intensyvumas nuo didžiausios vertės sumažėja iki 1/e jos dalies, didėjant galio kiekiui reikšmingai trumpėja. Bandiniuose be galio gesimo trukmė yra apie 92 ns, tuo tarpu bandiniuose su dideliu galio kiekiu ($x = 0.85$) ji sumažėja iki maždaug 2 ns.

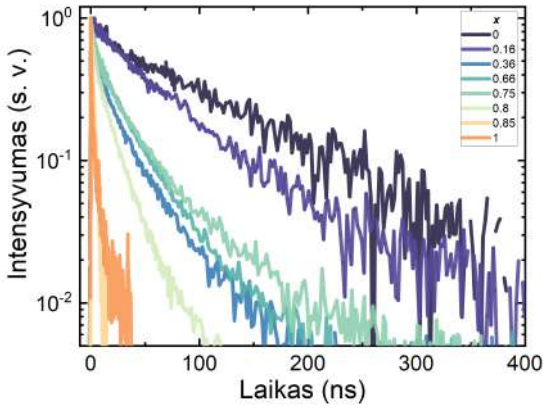

Pav. 12. Normuotos $Y_3(Al_{1-x}Ga_x)_5O_{12}$:Ce bandinių CL gesimo kinetikos esant skirtingam galio kiekiui *x*.

Siekiant įvertinti CL atsako tiesiškumą, ištirta CL intensyvumo priklausomybė nuo zondavimo srovės Pav. 13. Nustatyta netiesinė priklausomybė, kuri gali būti aprašyta laipsnine funkcija $I(j) \propto j^{\alpha}$. Didėjant galio kiekiui, α sumažėja nuo 0,84 iki 0,71. Tai rodo, kad bandiniuose su didesniu galio kiekiu stip-

rėja nukrypimas nuo tiesinės priklausomybės. Silpnas nuokrypis nuo tiesinės priklausyomybės nustatytas ir atliekant PL matavimus, tačiau tik tuomet, kai sužadinimo energijos tankis viršijo 10 mJ/cm^2. Nors netiesinis scintiliatorių atsakas dažnai siejamas su elektronų gaudyklių arba nespindulinės rekombinacijos centrų įsotinimu, šiuo atveju nustatyta netiesinė priklausomybė labiau atitinka Ce^{3+} emisijos centrų įsotinimą.

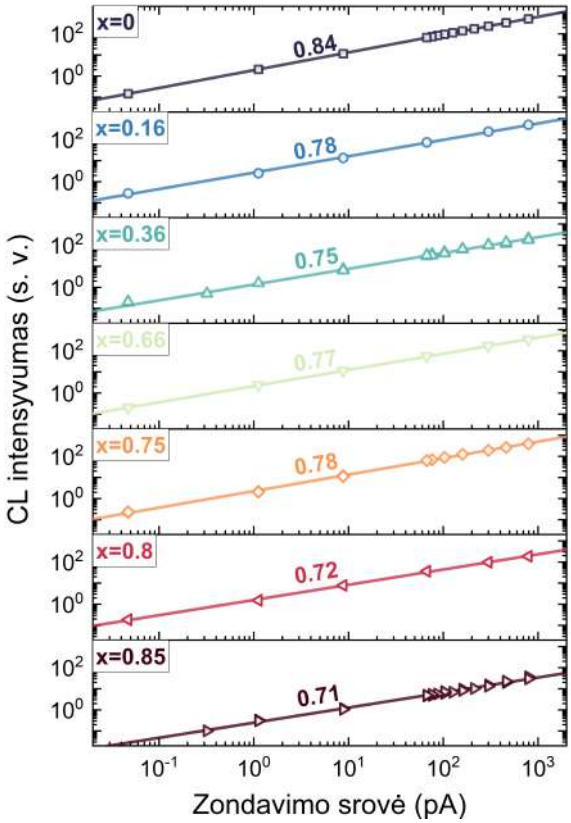

Pav. 13. $Y_3(Al_{1-x}Ga_x)_5O_{12}$:Ce bandinių CL intensyvumo priklausomybė nuo zondavimo srovės esant skirtingiems galio kiekiams x. Tiesės atitinka geriausius aproksimacijos rezultatus pagal galios dėsnį $I(j) \propto j^{\alpha}$.

Pav. 14 pateiktos kiekvieno tirto bandinio QY ir liuminescencijos gesimo trukmės vertės. Didžiausia QY nustatyta bandinyje, kuriame $x = 0{,}66$, o didėjant galio kiekiui liuminescencijos gesimo trukmė trumpėja. Vertinant scintiliacinių detektorių laikines charakteristikas, svarbūs ir užregistruotų fotonų skaičius, ir liuminescencijos gesimo trukmė. Sutapimų laikinė skyra (angl. coinciden-

ce timing resolution, CTR) apibūdina laiko skirtumo tarp dviejų sutampančių detekcijos įvykių nustatymo tikslumą. Supaprastintu atveju CTR yra proporcinga $\sqrt{\tau/N_{ph}}$, kur τ yra liuminescencijos gesimo trukmė, o N_{ph} – užregistruotų fotonų skaičius [1], [165]. Šiame darbe spektro ir laiko atžvilgiu integruotas CL intensyvumas naudotas kaip santykinis N_{ph} įvertis, todėl apskaičiuotas santykis $\sqrt{\tau/N_{ph}}$. Mažiausia šio santykio vertė nustatyta bandinyje, kuriame $x = 0{,}80$, o tai pagal taikytą santykinį įvertį rodo galimai geriausias laikines charakteristikas tirtoje bandinių serijoje. Tačiau šio bandinio QY yra gerokai mažesnė nei bandinio, kuriame $x = 0{,}66$, todėl būtent $x \sim 0.7$ gali būti laikoma palankiu kompromisu tarp liuminescencijos efektyvumo ir laikinių charakteristikų.

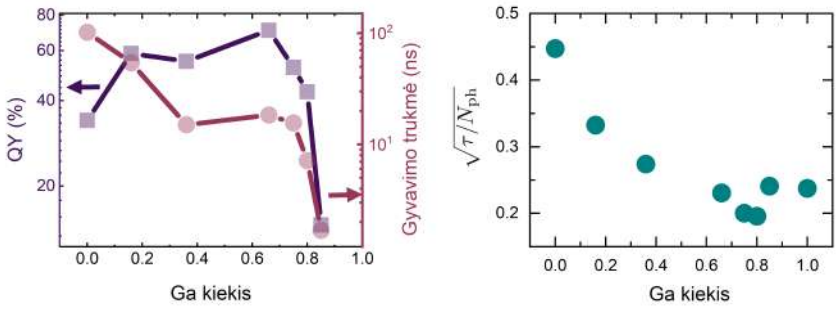

Pav. 14. $Y_3(Al_{1-x}Ga_x)_5O_{12}$:Ce bandinių QY (kvadratai, kairė ašis) ir gyvavimo trukmės (apskritimai, dešinė ašis) priklausomybė nuo galio kiekio x. Dešiniajame grafike pateiktos $\sqrt{\tau/N_{ph}}$ reikšmės priklausomai nuo galio kiekio x.

Spartus scintiliacinis atsakas yra itin svarbus scintiliatoriams, naudojamiems medicininio vaizdinimo sistemose, HEP eksperimentuose. Pavyzdžiui, SEM sistemose vieno pikselio skenavimo trukmė gali siekti vos 100 ns. Jei scintiliatoriaus gesimo trukmė yra panaši arba ilgesnė, dalis signalo persidengia su gretimų pikselių signalais, todėl mažėja vaizdo kontrastas [166]. Šiuo požiūriu svarbiausi parametrai yra gesimo trukmė ir liekamoji liuminescencija, nes uždelstas signalas mažina vaizdo kontrastą ir lemia jo išsiliejimą [168]. Plastikiniai scintiliatoriai šiose detekcijos sistemose plačiai naudojami dėl spartaus atsako ir mažų gamybos sąnaudų, tačiau jie turi reikšmingą trūkumą – veikiami elektronų pluošto greitai degraduoja [169].

Granato struktūros scintiliatoriai laikomi perspektyviomis medžiagomis CERN eksperimentams. Vienas gerai žinomų šios grupės scintiliatorių yra lutecio aliuminio granatas (LuAG:Ce), kurio liuminescencijos gesimo trukmė yra santykinai ilga ir siekia apie 70 ns [171]. Vis dėlto kolegiruojant šias medžiagas kitavalenčiais jonais, tokiais kaip Ca^{2+} arba Mg^{2+}, galima keisti krūvio kompensavimo ir su elektronų gaudyklėmis susijusius procesus, taip pagerinant scintiliacinį atsaką [13], [17]. LuAG:Ce laikinių charakteristikų pagerėjimas kolegiruojant siejamas tiek su elektronų gaudyklių poveikio sumažėjimu, tiek su Ce^{4+} jonų stabilizavimu [36]. Lygtyse (7.2) ir (7.3) pateikta reakcijų seka, rodanti stabilizuoto Ce^{4+} jono dalyvavimą spindulinės rekombinacijos procese. Pirmiausia Ce^{4+} jonas pagauna elektroną ir susidaro sužadintas Ce^{3+*} centras. Jam relaksuojant išspinduliuojamas fotonas, o Ce^{3+} jonas grįžta į pagrindinę būseną:

$$Ce^{4+} + e^- \rightarrow Ce^{3+*} \tag{7.2}$$

$$Ce^{3+*} \rightarrow Ce^{3+} + h\nu \tag{7.3}$$

Greta kolegiravimo, defektų kiekiui medžiagoje mažinti galima taikyti ir alternatyvius sintezės būdus, tokius kaip skystosios fazės epitaksija (angl. *liquid phase epitaxy* (LPE)). Taikant LPE metodą, granato struktūros sluoksniai formuojami gerokai žemesnėje temperatūroje, todėl sumažėja gardelės defektų ir įtrūkių susidarymo tikimybė [168]. Be to, po LPE proceso dažniausiai nereikia

papildomo mechaninio apdorojimo, todėl išvengiama su juo susijusių struktūrinių pažeidimų. Šiame darbe siekiama įvertinti didelių Mg^{2+} jonų koncentracijų įtaką optinėms savybėms ir nustatyti, ar Ce^{4+} jonų stabilizavimas lemia geresnes $Lu_{0.8}Gd_{2.2}Ga_{2.5}Al_{2.5}O_{12}$:Ce,Mg (LuGAGG) bandinių laikines charakteristikas. Ištirti šeši LuGAGG bandiniai su skirtingomis magnio koncentracijomis. Bandiniai gauti bendradarbiaujant su *Miroslav Kučera* vadovaujama tyrėjų grupe iš Čekijos. Informacija apie tirtų bandinių sudėtį pateikta Lentelė 3.

Lentelė 3. Magnio koncentracija (ppm) LuGAGG:Ce, Mg bandiniuose.

LuGAGG:Ce,Mg Mg kiekis (ppm)
0
35
300
700
2200
6000

LuGAGG bandinių sugerties spektrai pateikti Pav. 15. Nominali bendroji Ce koncentracija visuose bandiniuose yra vienoda, todėl stebimi skirtumai siejami su magnio koncentracijos kitimu. Pagrindiniai optinės sugerties maksimumai nustatyti ties 2,84 eV ir 3,65 eV. Jie atitinka Ce^{3+} jonų $4f \rightarrow 5d_1$ ir $4f \rightarrow 5d_2$ optinius šuolius. Didėjant magnio koncentracijai, abiejų sugerties juostų intensyvumas mažėja.

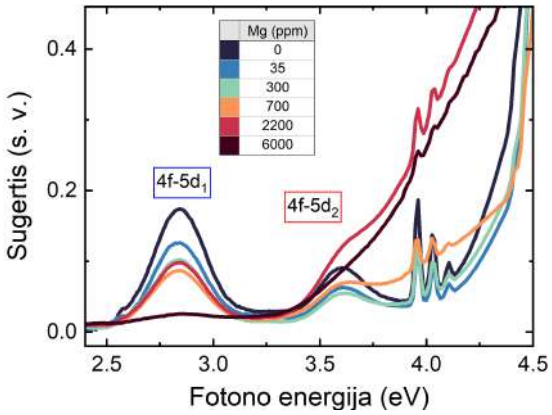

Pav. 15. LuGAGG:Ce,Mg bandinių su skirtingomis magnio koncentracijomis sugerties spektrai.

Tolesnė PL spektrų ir gesimo kinetikos analizė atlikta bandiniams, kuriuose Mg koncentracija yra 0, 300, 700 ir 2200 ppm, o bandinio su 6000 ppm Mg koncentracija PL signalas buvo per silpnas patikimiems matavimams atlikti. PL spektrų temperatūrinė priklausomybė tirta 80–600 K temperatūros intervale, atskirai žadinant į Ce^{3+} jonų $5d_1$ ir $5d_2$ energijos lygmenis (Pav. 16). Žadinant į $5d_1$ energijos lygmenį, didžiausias PL intensyvumas nustatytas esant apie 80 K temperatūrai, kai terminė jonizacija yra nuslopinta. Didėjant temperatūrai, terminė jonizacija stiprėja ir tampa vyraujančiu nespindulinio gesinimo procesu. Plačios ir asimetrinės emisijos juostos formą lemia du persidengiantys optiniai perėjimai iš sužadintojo $5d_1$ energijos lygmens į $4f$ konfigūracijos $^2F_{5/2}$ ir $^2F_{7/2}$ energijos lygmenis. Kolegiravimas net ir didelėmis magnio koncentracijomis reikšmingai nekeičia Ce^{3+} energijos lygmenų ar emisijos juostos spektrinės padėties.

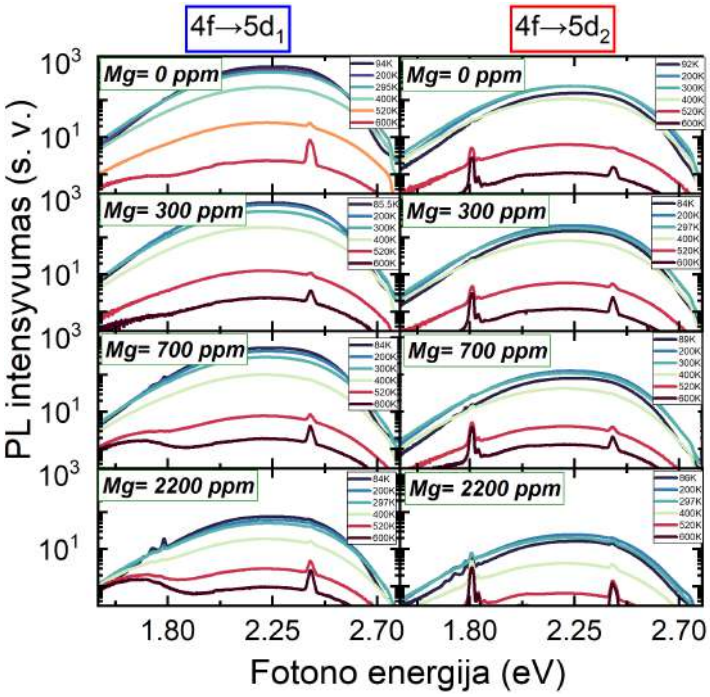

Pav. 16. LuGAGG:Ce,Mg bandinių temperatūriniai PL spektrai, žadinant į Ce^{3+} $5d_1$ ir $5d_2$ lygmenis.

Spektriškai integruoto PL intensyvumo temperatūrinės priklausomybės pateiktos Pav. 17. Jos analizuotos taikant Arrhenius modelį, o aktyvacijos energijos nustatytos atskirai žadinant į Ce^{3+} jonų $5d_1$ ir $5d_2$ energijos lygmenis. Aukštesnėje temperatūroje stebimas PL intensyvumo mažėjimas siejamas su termine jonizacija, kuri tampa vyraujančiu nespindulinio gesinimo procesu.

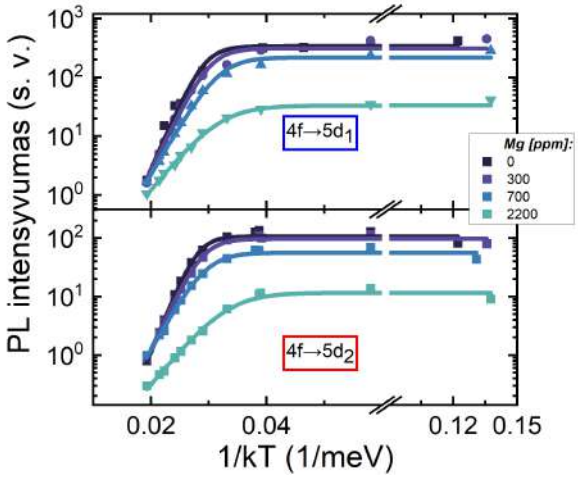

Pav. 17. LuGAGG:Ce,Mg bandinių PL intensyvumo temperatūrinės priklausomybės, žadinant į Ce^{3+} $5d_1$ ir $5d_2$ lygmenis.

Pav. 18 pateiktos LuGAGG bandinių PL gesimo kreivės rodo, kad magnio neturinčio bandinio PL gesimas plačiame temperatūros intervale gerai aprašomas vieneksponente funkcija. Didėjant magnio koncentracijai, PL gesimo kinetika vis labiau nukrypsta nuo vieneksponentės, o kreivėse išryškėja greitoji PL gesimo dedamoji. Didėjant temperatūrai, PL gesimo trukmė trumpėja dėl terminės jonizacijos. Magnio neturinčio bandinio PL gesimo trukmė kambario temperatūroje siekia apie 42 ns, o aukštesnėje temperatūroje tampa trumpesnė nei 1 ns. Esant didesnei magnio koncentracijai, PL gesimo trukmė jau kambario temperatūroje sutrumpėja iki maždaug 10 ns. Galima prisiminti, kad didėjant Mg koncentracijai Ce^{3+} emisijos juostos spektrinė padėtis beveik nekinta, bet emisijos gesimas reikšmingai spartėja.

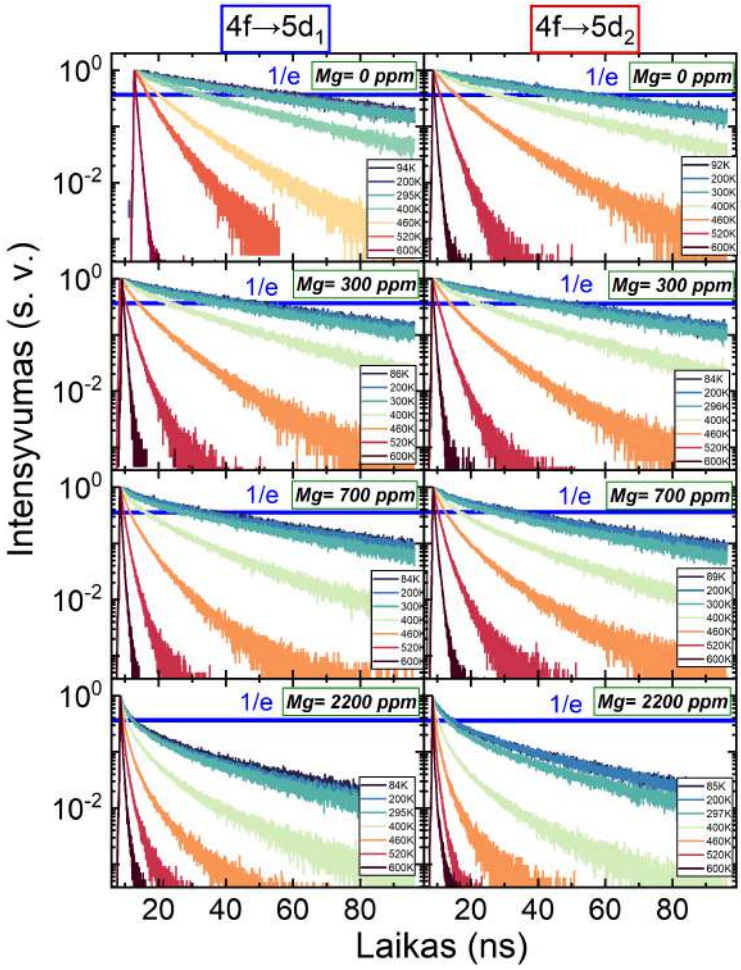

Pav. 18. Normuotos LuGAGG:Ce,Mg bandinių PL gesimo kinetikos temperatūrinės priklausomybės, žadinant į Ce^{3+} $5d_1$ ir $5d_2$ lygmenis.

PL gesimo trukmės temperatūrinės priklausomybės pateiktos Pav. 19, o jų analizei taip pat taikytas Arrhenius modelis. Aktyvacijos energijos, nustatytos iš PL intensyvumo ir gesimo trukmės temperatūrinių priklausomybių atskirai žadinant į Ce^{3+} jonų $5d_1$ ir $5d_2$ energijos lygmenis, palygintos Lentelė 4. Abiem metodais nustatyta tokia pati tendencija: didėjant Mg koncentracijai, aktyvacijos energija mažėja. Didinant Mg koncentraciją iki 300 ppm, aktyvacijos energija sumažėja nežymiai, tačiau toliau didinant Mg kiekį jos mažėjimas tampa gerokai ryškesnis.

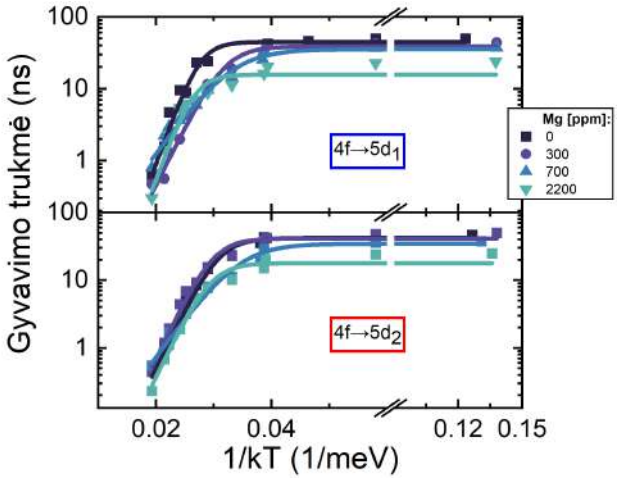

Pav. 19. LuGAGG:Ce,Mg bandinių PL gyvavimo trukmių temperatūrinės priklausomybės, žadinant į Ce^{3+} $5d_1$ ir $5d_2$ lygmenis.

Lentelė 4. Aktyvacijos energijos E_a (meV), nustatytos iš PL intensyvumo ir gyvavimo trukmių analizės, LuGAGG:Ce,Mg bandiniams su skirtinga magnio koncentracija, žadinant į Ce^{3+} $5d_1$ ir $5d_2$ lygmenis.

Bandinys (Mg kiekis), ppm	**Žadinant į $5d_1$ lygmenį**		**Žadinant į $5d_2$ lygmenį**	
	E_a *iš* **PL** (meV)	E_a *iš* $1/e$ (meV)	E_a *iš* **PL** (meV)	E_a *iš* $1/e$ (meV)
0	516 ± 41	486 ± 42	563 ± 27	462 ± 18
300	464 ± 37	423 ± 14	498 ± 17	407 ± 15
700	388 ± 21	348 ± 15	402 ± 22	316 ± 12
2200	278 ± 15	261 ± 5	273 ± 16	223 ± 8

Ankstesniuose tyrimuose laikinių charakteristikų pagerėjimas buvo siejamas su Ce^{4+} jonų stabilizavimu. Šiame darbe rezultatai aiškinami dviejų tipų emisijos centrų susidarymu: įprasto Ce^{3+} centro ir modifikuoto Ce^{3+}+Mg^{2+} centro, susidarančio Ce^{3+} ir Mg^{2+} jonams esant greta [181]. Magnio neturinčio LuGAGG bandinio PL gesimo kreivės, registruotos skirtingose temperatūrose žadinant į Ce^{3+} jonų $5d_1$ energijos lygmenį, ir gesimo trukmės temperatūrinė priklausomybė pateiktos Pav. 20. Visos gesimo kreivės gerai aprašomos vieneksponente funkcija, o tai rodo, kad liuminescencijoje vyrauja vieno tipo Ce^{3+}

emisijos centrai. Iš gesimo kreivių nustatyta gesimo trukmė τ_1, kurios temperatūrinė priklausomybė gerai aprašoma Arrhenius modeliu. Nustatyta 0,48 eV aktyvacijos energija, o spindulinė gesimo trukmė siekia apie 50 ns.

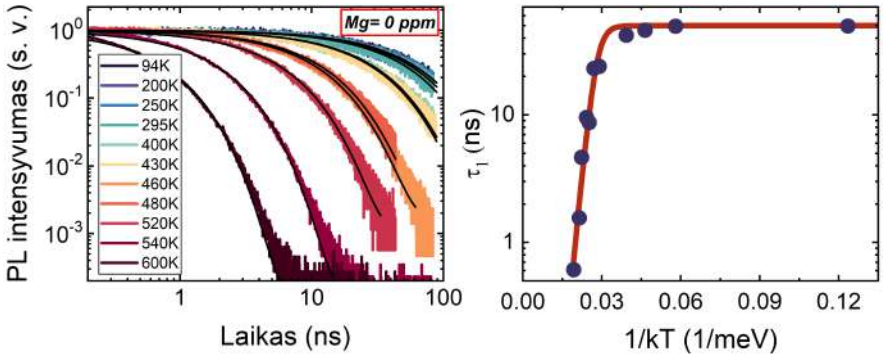

Pav. 20. Normuotos magnio neturinčio LuGAGG:Ce,Mg bandinio PL gesimo kinetikos temperatūrinės priklausomybės, žadinant į Ce^{3+} $5d_1$ lygmenį. Kinetikos aproksimuotos vieneksponentine funkcija. Dešinėje pusėje pateikta apskaičiuotos gyvavimo trukmės τ_1 temperatūrinė priklausomybė, aproksimuota Arrhenius išraiška (7.1).

Magniu legiruotų LuGAGG bandinių PL gesimo kinetika yra sudėtingesnė. Skirtingose temperatūrose išmatuotoms gesimo kreivėms aprašyti būtina atsižvelgti į antrojo tipo, modifikuotų Ce^{3+}+Mg^{2+} emisijos centrų, indėlį. PL intensyvumo $I(t)$ laikinė priklausomybė magniu kolegiruotuose bandiniuose aprašoma išraiška (7.4):

$$I(t) \propto w_1 \cdot \exp\left(-\frac{t}{\tau_1}\right) + (1 - w_1) \cdot \exp\left(-\frac{t}{\tau_2}\right) \tag{7.4}$$

čia w_1 yra svorio koeficientas, nusakantis Ce^{3+} centro indėlį;
τ_1 įprasto Ce^{3+} emisijos centro,
τ_2 modifikuoto Ce^{3+}+Mg^{2+} emisijos centro gesimo trukmė. Gesimo trukmės τ_1 ir τ_2 nustatytos aproksimuojant išmatuotas PL gesimo kreives (7.4) pateiktu dviejų eksponenčių modeliu. Jų temperatūrinės priklausomybės aprašytos Arrhenius lygtimi (7.1), kaip parodyta Pav. 21. Žemoje temperatūroje nustatyta τ_1 vertė, siekianti apie 50 ns, priskiriama Ce^{3+} centrų $5d_1 \rightarrow 4f$ spinduliniam gesimui. Modifikuotiems Ce^{3+}+Mg^{2+} emisijos centrams priskiriama greitoji

dedamoji τ_2, kurios trukmė net ir žemoje temperatūroje siekia apie 10.6 ns. Kadangi šiomis sąlygomis terminė jonizacija yra nereikšminga, rezultatai rodo, kad Ce^{3+}+Mg^{2+} centruose veikia papildomas, su termine jonizacija nesusijęs nespindulinės relaksacijos kanalas. Lentelė 4 pateiktų duomenų palyginimas rodo, kad didėjant magnio koncentracijai aktyvacijos energija mažėja. Ši tendencija gali būti siejama su didėjančia Ce^{3+}+Mg^{2+} centrų dalimi.

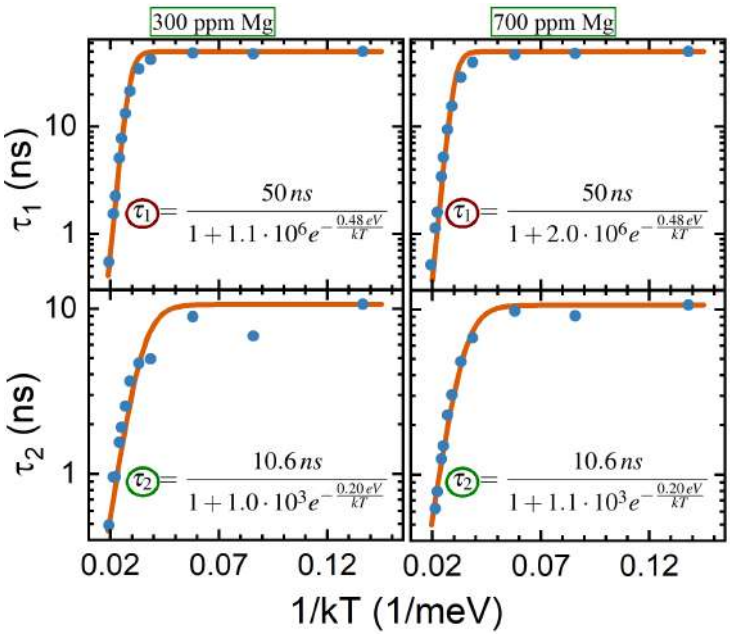

Pav. 21. LuGAGG:Ce,Mg bandinių su 300 ir 700 ppm magnio kiekiu PL gyvavimo trukmių τ_1 ir τ_2 temperatūrinės priklausomybės. Gyvavimo trukmės nustatytos iš išmatuotų temperatūrinių PL kinetikų, taikant (7.4) lygtį. Kreivės atitinka Arrhenius aproksimaciją, o aproksimacijos parametrai pateikti įterptuose grafikuose.

Pav. 22 pateikta LuGAGG bandinio energijos lygmenų schema, apimanti du pasiūlytus emisijos centrus ir jų spindulinės bei nespindulinės relaksacijos kanalus. Ce^{3+} centre elektronas gali būti sužadintas į $5d_1$ arba $5d_2$ energijos lygmenį. Į $5d_2$ lygmenį sužadintas elektronas pirmiausia nespinduliniu būdu relaksuoja į $5d_1$ lygmenį. Iš sužadinto energijos lygmens elektronas gali spinduliniu būdu grįžti į $4f$ energijos lygmenį arba, didėjant temperatūrai, būti termiškai jonizuotas į CB. Modifikuotame Ce^{3+}+Mg^{2+} emisijos centre papildomai vyksta nuo temperatūros nepriklausomas nespindulinės rekombinacijos (TINR) procesas, o terminės jonizacijos aktyvacijos energija sumažėja iki maždaug 200

meV. Dėl papildomo TINR kanalo ir mažesnės aktyvacijos energijos terminis gesinimas šiame centre yra stipresnis negu įprastame Ce^{3+} centre.

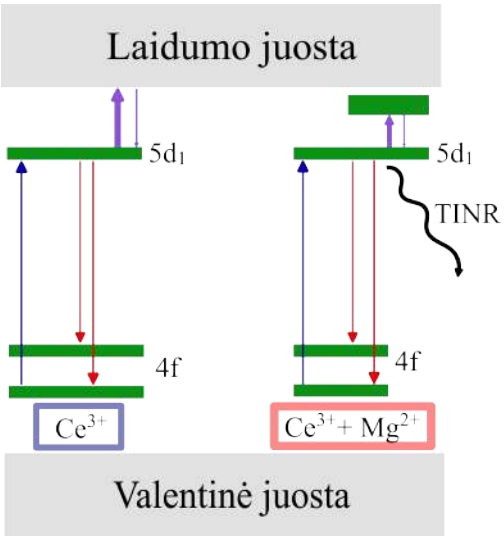

Pav. 22. LuGAGG:Ce,Mg bandinių Ce^{3+} ir Ce^{3+}+Mg^{2+} centrų energinių lygmenų diagrama. Mėlynos rodyklės nurodo optinį žadinimą, violetinės – terminę aktyvaciją, raudonos – spindulinę rekombinaciją į pagrindinius lygmenis, o juoda rodyklė žymi TINR.

Atliekant PL matavimus, Ce^{3+} centrai žadinami rezonansiškai, elektroną iš pagrindinio $4f$ energijos lygmens perkeliant į sužadintąjį $5d$ energijos lygmenį. Toks žadinimas galimas tik tada, kai cerio jonas yra Ce^{3+} oksidacijos būsenos ir turi $4f$ elektroną, todėl Ce^{4+} jonai šiuo būdu nežadinami. CL atveju bandinys žadinamas didelės energijos elektronais, todėl kristalinėje gardelėje susidaro nepusiausvirieji elektronai ir skylės. Šie krūvininkai migruoja gardelėje ir perduoda sužadinimo energiją Ce^{3+} emisijos centrams, o dalis jų gali rekombinuoti nespinduliniu būdu.

Pav. 23 pateiktas PL ir CL eksperimentuose išmatuotų emisijos intensyvumų palyginimas. Abiem sužadinimo metodais nustatyta panaši tendencija: kai magnio koncentracija viršija kelis šimtus ppm, emisijos intensyvumas reikšmingai sumažėja. Reikšmingų skirtumų tarp PL ir CL sužadinimo metodais gautų rezultatų nenustatyta.

Didele magnio koncentracija kolegiruotų LuGAGG bandinių laikinių charakteristikų pagerėjimas dažnai aiškinamas Ce^{4+} jonų stabilizavimu. Tačiau Ce^{4+} jonai neturi $4f$ elektrono, todėl negali būti tiesiogiai rezonansiškai sužadinti

vykstant $4f \rightarrow 5d$ optiniam perėjimui ir neprisideda prie šiuo būdu registruojamo PL signalo. CL sužadinimo metu gardelėje susidarę nepusiausvirieji krūvininkai gali būti pagaunami Ce^{4+} jonų, sudarydami sužadintus Ce^{3+*} centrus. Jei Ce^{4+} jonų stabilizavimo mechanizmas būtų vyraujantis, Pav. 23 pateiktos PL ir CL intensyvumo priklausomybės turėtų reikšmingai skirtis. Vis dėlto gauti rezultatai nepatvirtina, kad Ce^{4+} jonų stabilizavimas yra pagrindinė stebimo liuminescencijos gesimo spartėjimo priežastis. Abiem sužadinimo metodais nustatytas emisijos intensyvumo mažėjimas daugiausia siejamas su sustiprėjusia nespinduline rekombinacija emisijos centruose.

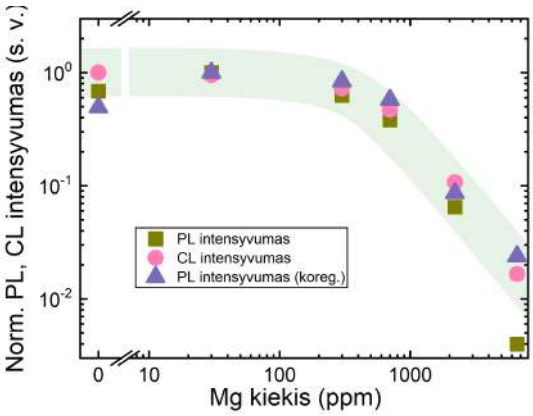

Pav. 23. Normuotų LuGAGG:Ce,Mg bandinių PL ir CL intensyvumų priklausomybė nuo magnio koncentracijos. CL intensyvumas pavaizduotas rožiniais taškais, o PL, žadinant į Ce^{3+} $5d_1$ lygmenį, pateiktas be korekcijos (žali kvadratai) ir su korekcija pagal sugertų fotonų skaičių (violetiniai trikampiai). Žaliai pažymėta sritis rodo bendrą stebimą tendenciją.

Skyrius 3: [x]Al_5O_{12}:Ce kompozitai, kur [x] = Lu_3, Y_3 ir $(Y, Lu)_3$

Czochralski (CZ) metodu scintiliatorių kristalai auginami aukštoje temperatūroje, o tai gali paskatinti kristalo gardelės defektų susidarymą. Be to, kristalams auginti dažnai reikalingi brangūs iridžio tigliai. Dėl šių priežasčių ieškoma alternatyvių sintezės ir kristalų auginimo technologijų, kurios leistų sumažinti tradiciniams metodams būdingus trūkumus ir gamybos sąnaudas. Ankstesniame skyriuje aprašyti LPE metodu užauginti bandiniai, o šis metodas gali būti laikomas viena iš CZ metodo alternatyvų. Kita galima strategija yra ceriu legiruotų granato struktūros mikrokristalų įterpimas į skaidrią matricą. Ankstesniuose tyrimuose nagrinėti ceriu legiruoti Ba–Gd silicio dioksido dariniai ir SiO_2:Ce^{3+} pasižymėjo perspektyviomis optinėmis savybėmis [182], [183].

Šiame skyriuje scintiliaciniams kompozitams sintetinti taikomas dviejų etapų zolio-gelio metodas. Gautus kompozitus sudaro granato struktūros mikrokristalai, įterpti į amorfinę silicio dioksido matricą. Šiuo metodu siekiama kelių pagrindinių tikslų: (1) pagerinti energijos perdavimą į Ce^{3+} emisijos centrus, (2) sumažinti paviršiaus defektų poveikį ir (3) sukurti lankstų bei ekonomišką zolio-gelio sintezės metodą. Bandinius susintetino ir pateikė *Aivaro Kareivos* vadovaujama mokslininkų grupė Vilniaus universitete.

Dviejų etapų zolio-gelio metodo eiga pateikta Pav. 24. Pirmajame etape metalų oksidų pirmtakai ištirpinti koncentruotoje azoto rūgštyje. Išgarinus tirpiklį, likęs gelis kelis kartus plautas distiliuotu vandeniu. Tuomet pridėta papildomų pirmtakų, kad būtų gauta nominali 0,5 % cerio koncentracija. Tirpalas 2 valandas maišytas 50 °C temperatūroje, tada pridėta citrinos rūgšties ir maišyta ilgiau nei 10 valandų. Toje pačioje temperatūroje išgarinus tirpiklį, susidaręs gelis 24 valandas džiovintas 140 °C temperatūroje. Gautas kserogelis termiškai apdorotas 600 °C temperatūroje, sutrintas, kalcinuotas 1000 °C temperatūroje, dar kartą sumaltas ir galiausiai atkaitintas 1200 °C temperatūroje, siekiant gauti medžiagą be įtrūkių. Antrajame etape atlikta tetraetoksisilano (TEOS) hidrolizė dejonizuotame vandenyje, pridėjus nedidelį kiekį azoto rūgšties ir pirmajame etape susintetintų miltelių. Kad mišinys taptų vienalytis, jis 1 valandą maišytas kambario temperatūroje. Vėliau mišinys apdorotas ultragarsinėje vonelėje, kad būtų pašalinti oro burbuliukai, ir 168 valandas džiovintas 70 °C temperatūroje. Gauti kserogeliai 2 valandas atkaitinti helio atmosferoje 1000 °C temperatūroje. Taip gautos skaidrios arba pusiau skaidrios kompozitinės medžiagos.

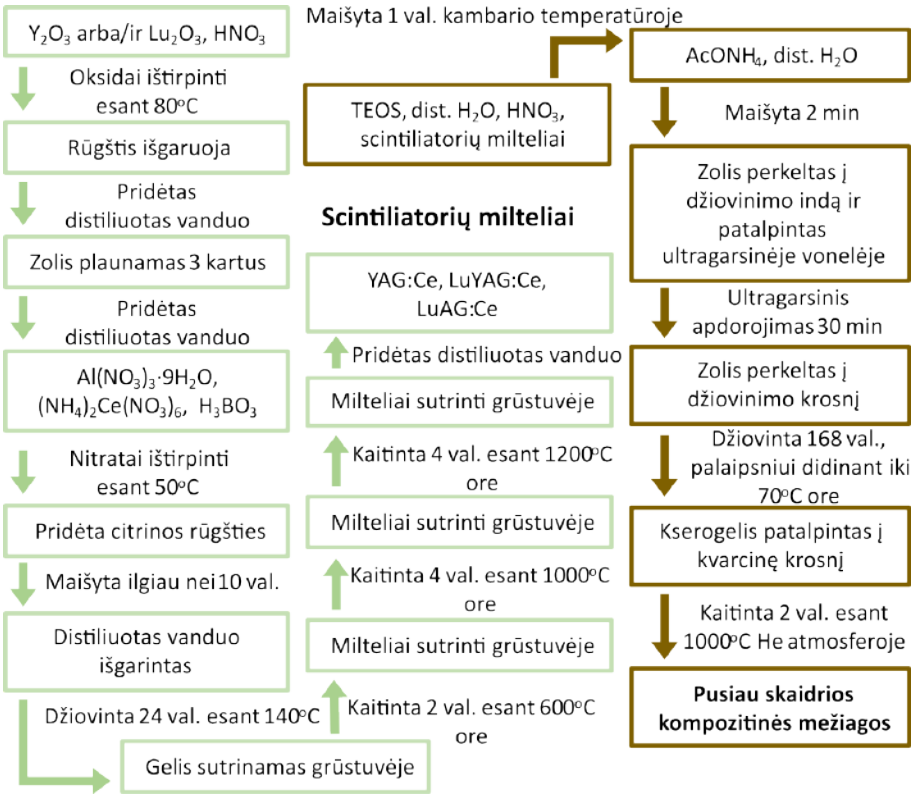

Pav. 24. Dviejų etapų zolio-gelio sintezės schema, skirta ceriu legiruotiems granato struktūros mikrokristalams įterpti į silicio dioksido matricą.

Šiame darbe tirtos trys tarpusavyje susijusios scintiliacinių kompozitų bandinių serijos. Pirmąją seriją sudarė YAG:Ce kompozitai, naudoti kaip etaloniniai bandiniai. Antrojoje serijoje dalis itrio buvo pakeista luteciu ir gautas LuYAG, o trečiojoje serijoje itris visiškai pakeistas luteciu ir gautas LuAG. Kiekvieną seriją sudarė keturi bandiniai, kuriuose įterpto granato kiekis buvo 0,5 wt%, 1 wt%, 1,5 wt% ir 2 wt%.

Pirmiausia susintetintų kompozitų fazinė sudėtis įvertinta rentgeno spindulių difrakcijos (XRD) metodu. Visų bandinių, kuriuose granato kiekis buvo 0,5 wt%, difraktogramos pateiktos Pav. 25. 20–30° kampų intervale stebimas platus difrakcinis maksimumas, būdingas amorfiniam SiO_2. Bandinių difraktogramos taip pat palygintos su etaloninėmis YAG ir LuAG difraktogramomis iš ICDD Powder Diffraction File (PDF) duomenų bazės. Palyginimas patvirtino, kad granato mikrokristalai yra vienfaziai, o kompozituose, be amorfinio silicio

dioksido, papildomų kristalinių fazių nenustatyta.

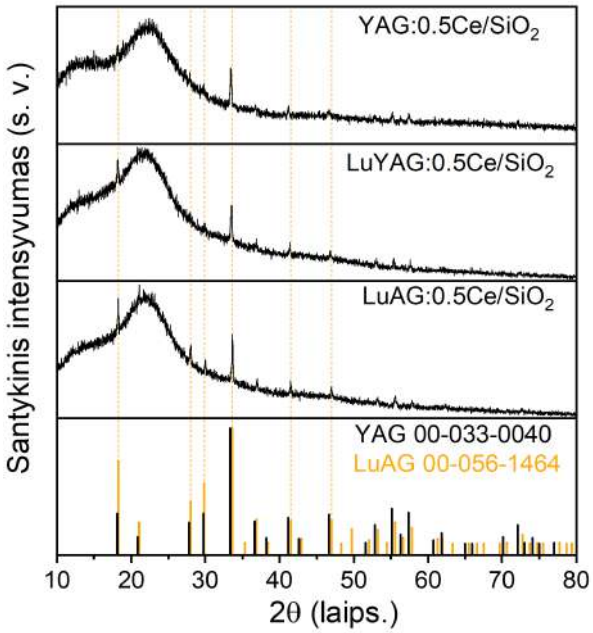

Pav. 25. 0.5 wt% YAG:Ce, LuYAG:Ce ir LuAG:Ce mikrokristalų turinčių kompozitų XRD difraktogramų palyginimas su atitinkamų kristalinių fazių etaloniniais PDF duomenimis.

Pav. 26 pateikti 2 wt% granato turinčio YAG:Ce/SiO_2 kompozito kelių sričių SEM vaizdai ir atitinkami CL intensyvumo žemėlapiai. Juose matyti, kad kompozitą sudaro submikrometriniai ceriu legiruoto granato grūdeliai įterpti į silicio dioksido matricą. Dalis šių grūdelių yra linkę aglomeruotis ir sudaryti didesnius darinius. Aglomeratų srityse registruojamas stipresnis CL signalas, nes jose sutelkta daugiau liuminescencinės medžiagos. Panašus grūdelių pasiskirstymas stebimas ir kitose kompozitų serijose. SEM vaizdų ir CL intensyvumo žemėlapių palyginimas padeda paaiškinti PL intensyvumo bei QY kitimą didėjant į silicio dioksido matricą įterpto granato kiekiui.

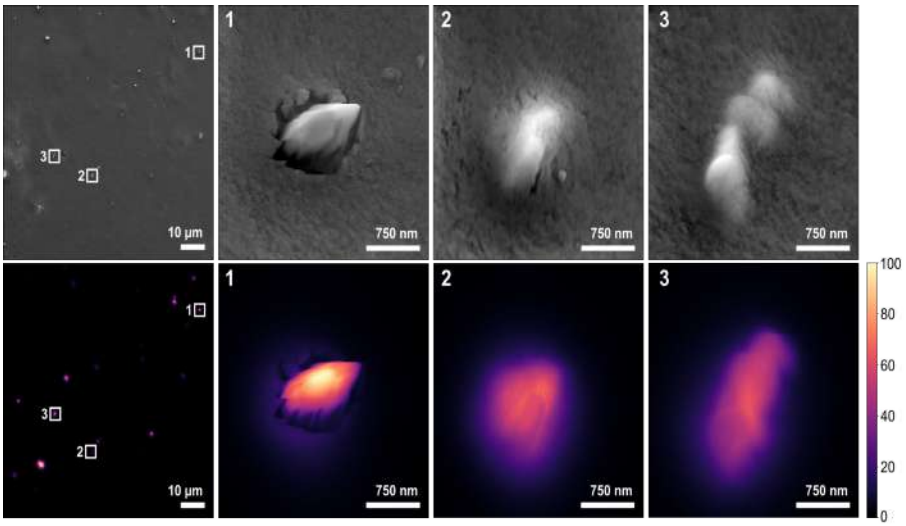

Pav. 26. YAG:Ce/SiO_2 kompozito, turinčio 2 wt% granato, SEM vaizdai (viršutinė eilė) ir atitinkami CL intensyvumo žemėlapiai (apatinė eilė). Numeriais pažymėtos bendro vaizdo sritys 1–3 fragmentuose parodytos didesniu padidinimu.

Dviejų 2 wt% granato turinčių kompozitų, YAG:Ce/SiO_2 ir LuAG:Ce/SiO_2, normuoti emisijos spektrai pateikti Pav. 27. Spektrai gauti rezonansiškai žadinant 2,75 eV fotonais į Ce^{3+} jonų $5d_1$ energijos lygmenį. Palyginimui taip pat pateikti YAG:Ce monokristalo (SC) ir LuAG:Ce monokristalinio sluoksnio (SCF) spektrai. Kompozitų emisijos spektrai nuo atitinkamų SC ir SCF bandinių spektrų reikšmingai nesiskiria.

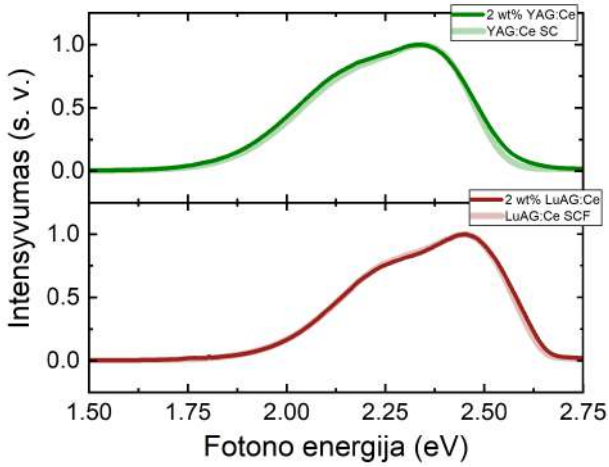

Pav. 27. Normuoti 2 wt% granato turinčių YAG:Ce/SiO_2 ir LuAG:Ce/SiO_2 bandinių PL spektrai. Spektrai palyginti su YAG:Ce SC ir LuAG:Ce SCF spektrais, žadinant į Ce^{3+} $5d_1$ lygmenį.

Lyginant kompozitų ir atitinkamų SC bei SCF bandinių Ce^{3+} emisijos spektrus, reikšmingų skirtumų nenustatyta nei žadinant į $5d_1$, nei į $5d_2$ energijos lygmenį. Tačiau žadinant į Ce^{3+} jonų $5d_2$ energijos lygmenį aptikta papildoma emisijos juosta ties maždaug 2,99 eV, rodanti emisiją iš SiO_2 matricos (Pav. 28). SiO_2 draustinio tarpo plotis siekia apie 9 eV, o naudota sužadinimo energija yra tik 3,58 eV. Todėl ši emisijos juosta siejama su SiO_2 matricoje esančių defektų liuminescencija. Pav. 28 dešinėje pateiktos gesimo kreivės rodo, kad SiO_2 emisija gęsta gerokai greičiau negu Ce^{3+} emisija. Vieneksponente funkcija aproksimavus gesimo kreives nustatyta, kad su Ce^{3+} centrais susijusios emisijos gesimo trukmė siekia apie 60 ns, o SiO_2 emisijos – apie 14 ns.

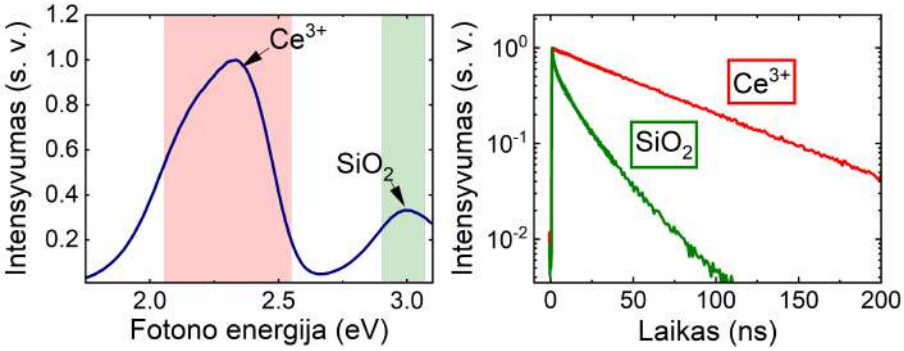

Pav. 28. YAG:Ce/SiO_2 PL spektrai, išmatuoti žadinant į Ce^{3+} $5d_2$ lygmenį. Dešiniajame grafike palygintos Ce^{3+} centrams ir SiO_2 matricos defektams priskiriamų emisijos juostų PL gesimo kreivės.

Trijų kompozitinių bandinių serijų PL intensyvumo priklausomybė nuo įterpto granato kiekio wt% pateikta Pav. 29. Esant mažam granato kiekiui, PL intensyvumas didėja beveik tiesiškai, tačiau toliau didinant granato kiekį pradeda augti sparčiau nei tiesiškai. Ši tendencija ypač ryški LuYAG:Ce/SiO_2 kompozituose. Viena iš galimų priežasčių yra efektyvesnis liuminescencijos išvedimas iš kompozito dėl sustiprėjusios sklaidos. Be to, didėjant granato kiekiui, mikrokristalai dažniau aglomeruojasi į didesnius darinius. Juose gali sumažėti santykinė paviršiuje esančių nespindulinės rekombinacijos centrų įtaka ir padidėti liuminescencijos efektyvumas. Abu šie veiksniai gali lemti spartesnį nei tiesinį PL intensyvumo augimą.

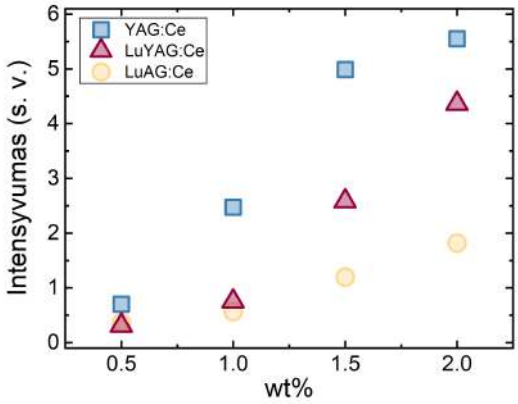

Pav. 29. YAG:Ce/SiO_2, LuYAG:Ce/SiO_2 ir LuAG:Ce/SiO_2 kompozitų PL intensyvumo palyginimas priklausomai nuo granato kiekio wt%, žadinant į Ce^{3+} $5d_1$ lygmenį.

Nors didėjant įterpto granato kiekiui bendras PL intensyvumas sistemingai auga, QY priklausomybė nėra tokia ryški. Trijų kompozitinių bandinių serijų QY priklausomybė nuo granato kiekio wt% pateikta Pav. 30. Matavimai atlikti žadinant į Ce^{3+} jonų $5d_1$ energijos lygmenį. Esant mažam granato kiekiui, QY didėja, o tai gali būti siejama su stiprėjančia mikrokristalų aglomeracija ir mažėjančia paviršinių nespindulinės rekombinacijos centrų įtaka. Esant didžiausiam granato kiekiui, visų trijų serijų QY vertės skiriasi nedaug ir patenka į 40–50 % intervalą. Jos išlieka mažesnės už YAG:Ce kristalo QY, siekiantį apie 80 % ir Pav. 30 pažymėtą mėlyna punktyrine linija. Didėjant granato kiekiui, bendras PL intensyvumas auga, nes emisijoje dalyvauja daugiau liuminescencinės medžiagos. Tačiau QY, apskaičiuotas atsižvelgiant į sugertų fotonų skaičių, rodo, kad bendras kompozito liuminescencijos efektyvumas palaipsniui įsisotina.

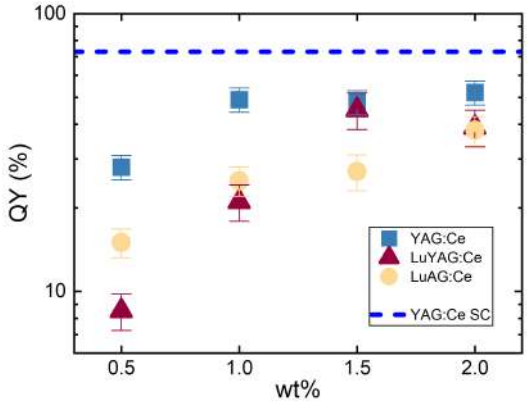

Pav. 30. YAG:Ce/SiO_2, LuYAG:Ce/SiO_2 ir LuAG:Ce/SiO_2 kompozitų QY priklausomybės nuo granato kiekio wt%, žadinant į Ce^{3+} jonų $5d_1$ energijos lygmenį. Punktyrinė linija žymi YAG:Ce SC bandinio QY vertę.

Visų kompozitinių bandinių PL gesimo trukmė yra panaši į SC bandinių ir siekia apie 60 ns. Normuotos LuYAG:Ce/SiO_2 kompozitų su skirtingais granato kiekiais wt% PL gesimo kreivės pateiktos Pav. 31. LuYAG:Ce/SiO_2 ir LuAG:Ce/SiO_2 bandinių gesimo kreivių pradžioje stebima greitoji dedamoji. Kaip matyti Pav. 31 intarpe, ji yra ryškesnė bandiniuose su mažesniu granato kiekiu. Tai gali būti siejama su stipriau išreikšta neradiacine rekombinacija.

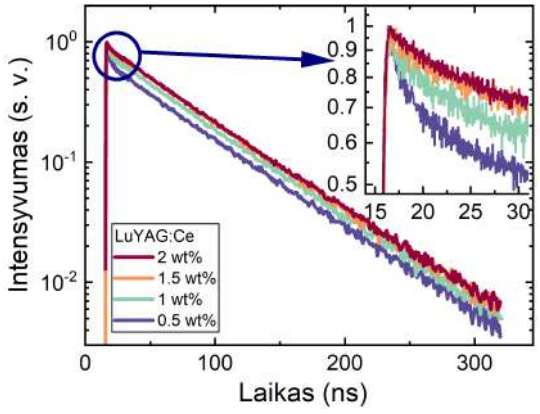

Pav. 31. LuYAG:Ce/SiO_2 bandinių, turinčių skirtingą granato kiekį wt%, PL gesimo kinetikos, žadinant į Ce^{3+} $5d_1$ lygmenį. Intarpe padidinta pradinė gesimo kreivių sritis.

Kelių skirtingų mikrokristalų CL spektrai, registruoti plačiame 1,5–4 eV ener-

gijų intervale, pateikti Pav. 32. Atskirų mikrokristalų spektrai reikšmingai nesiskiria. Tai rodo, kad tirtame dydžių ir formų intervale šie parametrai neturi pastebimos įtakos emisijos spektrui. Palyginus CL ir PL matavimais užregistruotą pagrindinę Ce^{3+} emisijos juostą nustatyta, kad jos maksimumo spektrinė padėtis nekinta, o forma abiem atvejais išlieka panaši.

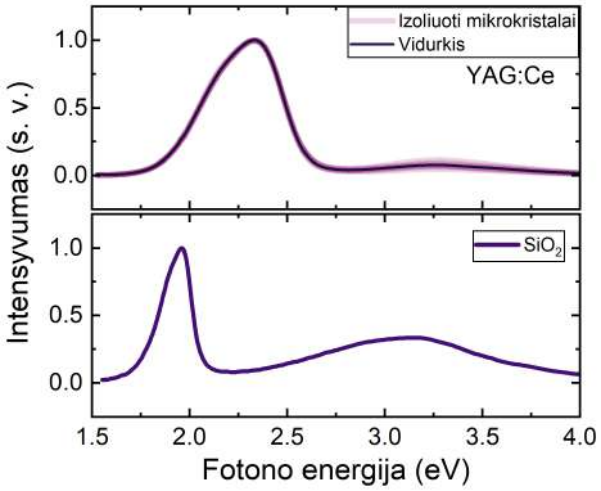

Pav. 32. Devyniuose pasirinktuose YAG:Ce/SiO_2 kompozito mikrokristaluose užregistruoti CL spektrai (viršutinis grafikas). Apatiniame grafike pateikti CL spektrai, išmatuoti kompozito srityse, kuriose nėra granato mikrokristalų.

Pav. 33 pateiktos kompozitinių bandinių CL gesimo kreivės. YAG:Ce/SiO_2 bandinio Ce^{3+} emisijos gesimo trukmė siekia apie 85 ns. LuYAG:Ce/SiO_2 ir LuAG:Ce/SiO_2 bandiniuose pagrindinio gesimo trukmė yra panaši, tačiau pradinėje kreivių dalyje papildomai stebimas spartesnis procesas. Panaši dviejų eksponenčių gesimo kinetika nustatyta ir anksčiau tirtuose LuGAGG:Ce,Mg bandiniuose, kuriuose greitoji komponentė buvo siejama su modifikuotų Ce^{3+}+Mg^{2+} emisijos centrų susidarymu. Lu turinčiuose kompozituose šis spartesnis gesimas gali būti siejamas su papildomu nespindulinės relaksacijos kanalu, veikiančiu dalyje Ce^{3+} emisijos centrų.

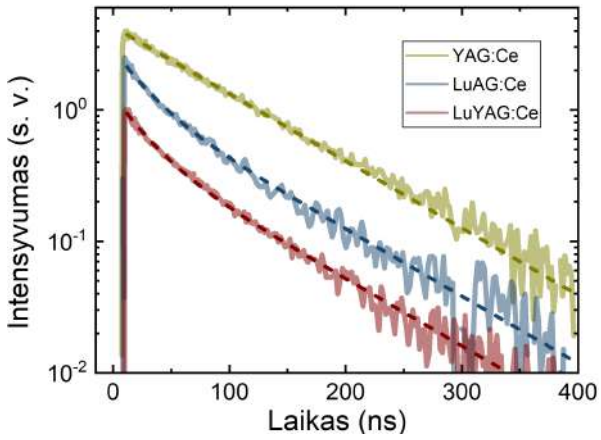

Pav. 33. YAG:Ce/SiO_2, LuAG:Ce/SiO_2, LuYAG:Ce/SiO_2 kompozitų CL gesimo kreivės. Ištisinės linijos žymi išmatuotus duomenis, o punktyrinės linijos – jų aproksimacijas.

Atskirų grūdelių CL intensyvumo priklausomybė nuo jų projekcinio ploto pateikta Pav. 34. Tirti trijų serijų kompozitai – YAG:Ce/SiO_2, LuAG:Ce/SiO_2 ir LuYAG:Ce/SiO_2, kuriuose granato kiekis buvo 2 wt%. Grūdelio projekcinis plotas nustatytas pagal CL intensyvumo žemėlapio pikselių, kurių intensyvumas viršijo pasirinktą slenkstinę vertę, skaičių. Kiekvienam grūdeliui šių pikselių CL intensyvumai buvo susumuoti, o gauta vertė normuota pagal projekcinį plotą. Jei bendras emisijos intensyvumas būtų proporcingas tik grūdelio projekciniam plotui, normuotas intensyvumas nepriklausytų nuo grūdelio dydžio ir visi duomenų taškai Y ašyje turėtų panašias vertes. Tačiau visose trijose kompozitų serijose pagal projekcinį plotą normuotas intensyvumas didėja kartu su grūdelio dydžiu. Ši tendencija gali būti siejama su didėjančiu grūdelio tūrio ir paviršiaus ploto santykiu. Kadangi grūdelių paviršiuje gali būti nespindulinės rekombinacijos centrų, didėjant grūdeliui santykinė jų įtaka mažėja, todėl didesni grūdeliai gali pasižymėti efektyvesne liuminescencija.

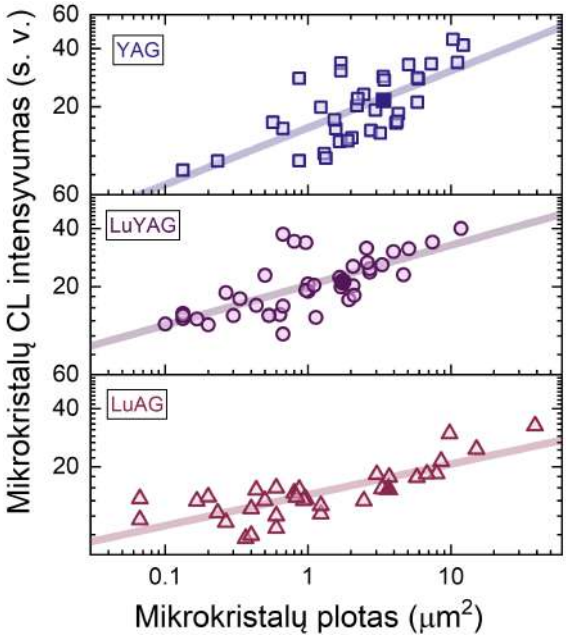

Pav. 34. Atskirų mikrokristalų CL intensyvumo priklausomybė nuo jų projekcinio ploto YAG:Ce/SiO_2, LuAG:Ce/SiO_2 ir LuYAG:Ce/SiO_2 kompozituose, turinčiuose 2 wt% granato. Intensyvumo vertės normuotos pagal mikrokristalo projekcinį plotą. Užpildyti simboliai žymi panašaus dydžio mikrokristalų vidutines vertes.

CURRICULUM VITAE

Arnoldas Solovjovas

WORK EXPERIENCE

Junior Research Fellow 2024 – Present
Vilnius University Institute of Photonics and Nanotechnology

Laboratory Technician 2022 – 2024
Vilnius University Institute of Photonics and Nanotechnology

EDUCATION

PhD Studies in Physics 2022 – 2026
Vilnius University Faculty of Physics

Master of Business Administration (MBA) 2020 – 2021
Vilnius University Business School

Master of Electronics and Telecommunication Technologies 2019 – 2021
Vilnius University Faculty of Physics

Bachelor of Telecommunication Physics and Electronics 2015 – 2019
Vilnius University Faculty of Physics

RESEARCH PROJECTS

LMT, S-CERN-24-7 2024 – Present
Daugiakomponenčio granato sudėties įtaka scintiliacijos spartai

LMT, S-A-UEI-23-6/6 2023 – Present
Tobulinti sparčius scintiliatorius jonizuojančiosios spinduliuotės detektoriams, skirtiems didelio šviesingumo aukštų energijų fizikos eksperimentams ir didelės erdvinės skyros medicininiam vaizdinimui

LIST OF PUBLICATIONS

PAPER 1 **Arnoldas Solovjovas**, Oleg Sidletskiy, Iaroslav Gerasymov, Saulius Nargelas, Gabija Soltanaitė, Žydrūnas Podlipskas, Etiennette Auffray and Gintautas Tamulaitis. Influence of gallium content on luminescence properties of Ce-doped yttrium aluminum gallium garnet scintillator. Optical Materials, vol. 168 (2025), article 117480. DOI: 10.1016/j.optmat.2025.117480.

PAPER 2 Saulius Nargelas, **Arnoldas Solovjovas**, Yauheni Talochka, Žydrūnas Podlipskas, Miroslav Kucera, Zuzana Lucenicova and Gintautas Tamulaitis. Influence of heavy magnesium co-doping on emission decay in Ce-doped multicomponent garnet scintillators. Journal of Materials Chemistry C, vol. 11, no. 35 (2023), pp. 12007–12015. DOI: 10.1039/D3TC02247A.

PAPER 3 Saulius Nargelas, Monika Skruodienė, **Arnoldas Solovjovas**, Šarūnas Ščefanavičius, Gabija Soltanaitė, Mantas Migauskas, Žydrūnas Podlipskas, Aivaras Kareiva and Gintautas Tamulaitis. Novel scintillators based on cerium-doped garnets in amorphous silica: crystal quality at the cost of glass. Journal of Materials Chemistry C, vol. 13, no. 25 (2025), pp. 12745–12753. DOI: 10.1039/D5TC00985E.

LIST OF OTHER PUBLICATIONS

- **Arnoldas Solovjovas**, Saulius Nargelas, Gabija Soltanaitė, Žydrūnas Podlipskas, Yuriy Zorenko, Vitaliy Gorbenko, Etiennette Auffray and Gintautas Tamulaitis. Luminescence kinetics in Ce-doped $\mathrm{Tb}_x\mathrm{Gd}_{3-x}\mathrm{Al}_5\mathrm{O}_{12}$ garnet with various terbium content. Journal of Luminescence, vol. 288 (2025), article 121555. DOI: 10.1016/j.jlumin.2025.121555.

- Mattia Cipriani, Fabrizio Consoli, Massimiliano Scisció, **Arnoldas Solovjovas**, Ioanna Angeliki Petsi, Mangirdas Malinauskas, Pierluigi Andreoli, Giuseppe Cristofari, E. Di Ferdinando and Giorgio Di Giorgio. Experimental and simulation study on high-power laser irradiation of 3D-printed microstructures. Matter and Radiation at Extremes, vol. 11, no. 2 (2026), article 027401. DOI: 10.1063/5.0283201.

- Saulius Nargelas, Oleg Sidletskiy, Iaroslav Gerasymov, **Arnoldas Solovjovas**, Gabija Soltanaitė, Žydrūnas Podlipskas, Loris Martinazzoli, Louis Roux, Etiennette Auffray and Gintautas Tamulaitis. Engineering the luminescence properties of YAG:Ce scintillators by double aliovalent codoping. Journal of Luminescence, vol. 299 (2026), article 122109. DOI: 10.1016/j.jlumin.2026.122109.

LIST OF CONFERENCES

- **A.Solovjovas**, S.Nargelas, Y.Talochka, M.Kucera, G.Tamulaitis. Influence of Mg^{2+} codoping on excitation relaxation and emission properties of $(Lu, Gd)_3(Ga, Al)_5O_{12}$:Ce,Mg scintillators. 51st International School and Conference on the Physics of Semiconductors "Jaszowiec 2023". June 17–23, 2023, Jaszowiec, Poland.

- **A.Solovjovas**, S.Nargelas, M.Kucera, Y.Talochka, Ž.Podlipskas, Z. Lucenicova. G.Tamulaitis. Stipraus kolegiravimo Mg^{2+} jonais poveikis šviesos emisijai ceriu legiruotuose daugiakomponenčiuose granatiniuose scintiliatoriuose. 45th Lithuanian National Physics Conference. October 25–27, 2023, Vilnius, Lithuania.

- M.Iršėnas, A.Vaitkevičius, S.Nargelas, A.Solovjovas, V.Gorbenko, Y. Zorenko, G. Tamulaitis. Optical properties of cerium doped multicomponent garnet type scintillators grown by liquid phase epitaxy. The 67th International Open readings conference. April 23–26, 2024, Vilnius, Lithuania.

- **A.Solovjovas**, S.Nargelas, Y.Talochka, Ž.Podlipskas, M.Kucera, Z. Lucenicova. G.Tamulaitis. Study of the emission properties of $(Lu, Gd)_3(Ga, Al)_5O_{12}$:Ce scintillators. European Workshop on Innovative and Advanced Epitaxy. June 11–14, 2024, Vilnius, Lithuania.

- **A.Solovjovas**, S.Nargelas, O.Sidletskiy, G.Tamulaitis. Investigation of emission properties in $Y_3(Al_{1-x}Ga_x)_5O_{12}$:Ce scintillators with different gallium content. 12th International Conference on Luminescent Detectors and Transformers of Ionizing Radiation. June 16–21, 2024, Riga, Latvia.

- S.Nargelas, Y.Talochka, Ž.Podlipskas, A.Solovjovas, G.Tamulaitis, Z.Lucenicova, M.Kucera. Mechanisms of aliovalent codoping on the timing properties of the multicomponent garnet scintillators. 12th International Conference on Luminescent Detectors and Transformers of Ionizing Radiation. June 16–21, 2024, Riga, Latvia.

- S.Nargelas, A.Solovjovas, Y.Talochka, Ž.Podlipskas, G.Tamulaitis, M.Kucera, Z.Lucenicova. Acceleration of emission decay in Ce-doped

multicomponent garnet scintillators by heavy magnesium codoping. 17th International Conference on scintillating materials and their application. July 8–12, 2024, Milan, Italy.

- **A.Solovjovas**, S.Nargelas, Y.Talochka, Ž.Podlipskas, M.Kucera, Z. Lucenicova. G.Tamulaitis. Investigation of the influence of heavy Mg^{2+}-codoping on emission properties of $(Lu, Gd)_3(Ga, Al)_5O_{12}$:Ce scintillators. Advanced Materials and Technologies. August 26–30, 2024, Palanga, Lithuania.

- **A.Solovjovas**, S.Nargelas, O.Sidletskiy, G.Tamulaitis. Investigation of emission properties in $Y_3(Al_{1-x}Ga_x)_5O_{12}$:Ce scintillators with different gallium content. AIDAinnova training course on quantum applications. January 23–24, 2025, Geneva, Switzerland, CERN.

- G.Tamulaitis. S.Nargelas, A.Solovjovas, Š.Ščefanavičius, G.Soltanaitė, Ž.Podlipskas, M.Skruodienė, A.Kareiva. Novel cost-efficient scintillators for fast radiation detection. 13th international conference on radiation, natural sciences, medicine, engineering, technology and ecology. June 16–20, 2025, Herceg Novi, Montenegro.

- **A. Solovjovas**, S. Nargelas, G. Soltanaitė, Ž. Podlipskas, Y. Zorenko, E. Auffray, G. Tamulaitis. Photoluminescence properties of Ce-doped $Tb_xGd_{3-x}Al_5O_{12}$ with different terbium content. Advanced Materials and Technologies. August 25–29, 2025, Palanga, Lithuania.

- **A.Solovjovas**. S. Nargelas, M. Skruodienė, Š.Ščefanavičius, G. Soltanaitė, Ž. Podlipskas, A. Kareiva, G. Tamulaitis. Cost-effective composite scintillators based on Ce-doped garnets in amorphous silica. 46th Lithuanian National Physics Conference. October 8–10, 2025, Kaunas, Lithuania.

- **A.Solovjovas**, S. Nargelas, M. Skruodienė, Š.Ščefanavičius, G. Soltanaitė, M. Migauskas, Ž. Podlipskas, A. Kareiva, G. Tamulaitis. Cost-effective composite scintillators of Ce-doped garnets embedded in amorphous silica. 5th CERN Baltic conference, October 14–16, 2025, Kaunas, Lithuania.

- M. Iršėnas, A. Vaitkevičius, A. Solovjovas, S. Nargelas. Investigation of the dependence of photoluminescence properties on magnesium con-

centration in LuAG:Ce scintillators. The 69th International Open readings conference, April 27–30, 2026, Vilnius, Lithuania.

- **A.Solovjovas**, S.Nargelas, G.Soltanaitė, Ž.Podlipskas, Y.Zorenko, V.Gorbenko, E.Auffray, G.Tamulaitis. Influence of terbium content on the photoluminescence properties of Ce-doped $Tb_xGd_{3-x}Al_5O_{12}$. SCINT 2026, May 25–29, 2026, Gyeongju, South Korea.
- **A.Solovjovas**, O.Sidletskiy, I.Gerasymov, S.Nargelas, G.Soltanaitė, Ž.Podlipskas, E.Auffray, G.Tamulaitis. Influence of gallium content on emission properties of $Y_3(Al_{1-x}Ga_x)_5O_{12}$:Ce scintillators. EuroDIM 15, July 5–10, 2026, Timisoara, Romania.

NOTES

NOTES

Vilniaus universiteto leidykla
Saulėtekio al. 9, III rūmai, LT-10222 Vilnius
El. p. info@leidykla.vu.lt, www.leidykla.vu.lt
bookshop.vu.lt, journals.vu.lt
Tiražas 25 egz.